Synthesis and Characterization of Metallic Nanostructures via Pulsed Laser Induced Dewetting and Electron Beam Lithography

A Dissertation Presented for the
Doctor of Philosophy
Degree
The University of Tennessee, Knoxville

David A. Garfinkel
December 2021

ACKNOWLEDGMENTS

I would like to thank my graduate advisor Philip Rack for providing me with the opportunity to grow as a person and researcher at the University of Tennessee. He has always provided me with guidance and assistance when I have needed it. I would also like to thank my committee members: Jason Fowlkes, Dustin Gilbert, and Andre Zeumault. Jason Fowlkes specifically has assisted me countless times whenever I have asked. A special thank you is also needed for all the cleanroom staff at the Center for Nanophase Material Science at Oak Ridge National Lab, you have all been incredibly helpful and a joy to be around. Finally, I would like to thank all my friends and family for supporting me throughout this process, I really appreciate everyone's help.

ABSTRACT

Metallic nanostructures have a wide range of applications from high resolution sensing to cancer treatment. Here, these structures are synthesized via a combination of single metal and bi-metal sputtering, in parallel with pulsed laser induced dewetting (PLiD) and electron beam lithography. PLiD is used to generated arrays of spherical caps that can be controlled by initial thin film geometry, namely the thickness. Electron beam lithography is used to produce higher complexity structures such as coupled meta-atoms. By using metallic elements that possess plasmonic (Au and Ag) and magnetic (Ni and Co) properties, tunability that is a function of size, composition, and chemical morphology can be achieved. In this work we first investigate the PLiD dewetting of a two-component system, Ag-Ni, to observe how the thermodynamic un-mixing behavior interplays with dewetting dynamics. This is done through a combination of fluid dynamic computational modeling (collaboration with NJIT), thermal finite element modeling, and experimental results. In the next chapter, the properties of this material system are studied. Both as deposited thin films, and PLiD particles of varying sizes are fabricated and measured to determine the magneto-plasmonic bi-functionality and tunability of the material system. In the third chapter, the magnetic and plasmonic properties of a second material system, Au-Co, are investigated. In this chapter chemical composition and chemical morphology are added to the tunability parameters. Finally, the fourth chapter investigates the use of electron beam lithography to synthesize ring nanostructures with plasmonic modes that can be excited through both the electric and magnetic components of an incident light source. Imaging of this behavior will be done via excited state electron energy gain and loss spectroscopy.

TABLE OF CONTENTS

LIST OF FIGURES

INTRODUCTION

Motivation

There are three primary motivations for this research: 1) enhancing the fundamental understanding of the dynamics involved in liquid dewetting, by competing/simultaneous phase separation behavior and kinetics for alloy systems, 2) creating functional materials with tunable combined magnetic and plasmonic properties, and 3) demonstrating the unique capabilities of the in situ Waviks optical delivery system via excited state electron energy spectroscopy.

From a theoretical modeling point of view, nanoscale dewetting of liquid metal films is exceptionally complex. Molecular dynamics simulations that incorporate real time and length scales of experiments are extremely computationally expensive. On the other hand, when using a continuum approach, the process is complicated by, amongst other things, the use of the Navier-Stokes equations to model nonlinear dynamics. This has made developing accurate computational models difficult in the past; however, significant progress has taken place, and good agreement has been observed in collaborative experimental and computational work in single component systems[1–3]. Focus has thus shifted to multicomponent systems. Through a collaborative effort combining continuum and molecular dynamics simulations with experimental work (the focus of this dissertation), the immiscible Ag-Ni material system will be studied to build upon the existing knowledge in single component metallic dewetting. The experimental portion of this collaboration is essential for providing input parameters as well as validating the developed theory.

The second aspect of this work is in the development of unique nanostructures, generated through the process of dewetting, that offer potential for use as functional materials. Metallic nanoparticles can be leveraged in a plethora of applications, including nanoelectronics, energy harvesting, biomedical engineering, and data storage[4–6]. Pulsed laser induced dewetting (PLID) provides a

highly robust technique for generating functional nanoparticles from a simple thin film geometry. The expansion of PLiD to multicomponent systems offers the ability to provide additional functionality and enhanced control over the material properties. Specifically, a plasmonic material can be combined with a magnetic material in individual nanoparticles to generate optimized magneto-plasmonic bi-functionality that is not possible with a single component. Further, introducing a second component reveals chemical composition and morphology as additional sources of tunability beyond nanoparticle size.

Finally, this work demonstrates the capabilities of a new *in situ* laser delivery system that has recently been installed on the Libra 200 (S)TEM at the Joint Institute for Advanced Materials (JIAM). In addition to the ability to photothermally heat a sample, this laser system has been combined with scanning transmission electron microscopy ((S)TEM) electron energy loss spectroscopy (EELS) to obtain an additional, otherwise unavailable, functionality: stimulated electron energy gain/loss spectroscopy (sEEGS/sEELS). In the place of PLiD, the added resolution and control of electron beam lithography is used to synthesize complex nanostructures specifically designed to couple to the energy of the laser system (1.58 eV). Optical excitation of simple rod[7] and dimer[8] structures has already been demonstrated with this system. In these previous studies, optical coupling is driven by the electric component of the laser. Here, coupling via the magnetic component of the optical field will be demonstrated by strategic design of metaatoms possessing a ring geometry, and thus a plasmonic mode with a magnetic dipole.

Background

Thin Films

A thin film is a geometric configuration of a material in which one dimension, the thickness, is significantly reduced, typically on the nanometer scale. The thickness is defined as the dimension

normal to the supporting substrate, as can be seen in Figure 1. There are various experimental techniques that can be used to generate thin films; these techniques are typically subdivided into two categories: physical and chemical. The predominant chemical techniques include chemical vapor deposition, plasma enhanced chemical vapor deposition, sol-gel, spray pyrolysis, and spin coating. Physical techniques are comprised of sputtering (direct current, radio frequency, magnetron, ion beam) and evaporation (thermal, laser, electron beam).

Sputtering

The general concept of sputtering is using physical collisions to eject atoms from a desired material to deposit on a substrate. The starting point for any sputtering process is a high vacuum, where unwanted collisions with molecules in the sputtering chamber are minimized. As can be seen in Figure 1, the necessary components inside this chamber are a "target", the material that will be used for sputtering, and a substrate, which will be used to support the generated thin film. Once a high vacuum is reached, the sputtering process is achieved by inserting a gas into the chamber near the target and applying a strong bias to that target to generate a plasma. This can be done as a direct current or alternating current depending on the sputtering technique. The ionization of Ar atoms by the plasma leads to an attraction to the target, and ultimately collisions that results in the ejection of target atoms in all directions. During the sputtering process some of these ejected atoms will be directed at the substrate material, and ultimately lead to the generation of a thin film. Complexity can be added by introducing a second target and voltage source to create multicomponent films. Further, the targets orientation to the substrate can introduce nonuniform deposition across the substrate, where one part of the substrate experiences a greater deposition rate that another. This can be leveraged to generate a single thin film with a wide chemical gradient for rapid

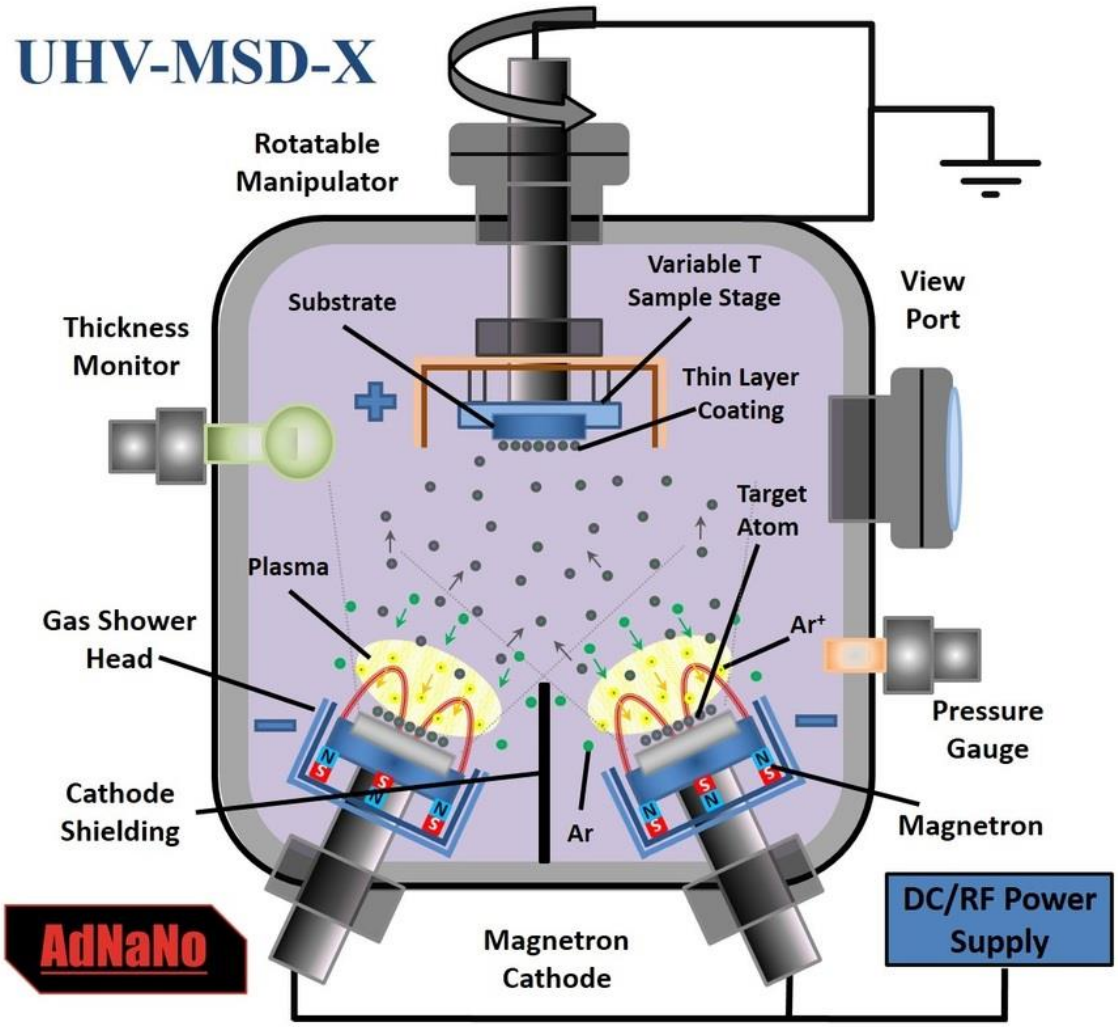

Figure 1: Representation of sputtering in a radio frequency magnetron spurting system[9]

characterization of large portions of the phase diagram, or the gradient can be eliminated by rotating the sample during depositions.

Dewetting

Wetting and Partial Wetting

Metal deposited on a substrate via physical vapor deposition, e.g., sputtering, will form a metastable solid thin film that entirely covers, or wets, the substrate. This, however, is not the equilibrium configuration due to the large surface to volume ratio. The equilibrium wetting behavior is determined by an energy balance between the covered substrate (wet), and the dry substrate (dewet). This relationship is represented in the spreading parameter, shown in equation 1 and 2. Here, S is the spreading parameter, γ_{SG} is the substrate-air/vacuum surface energy, γ_{SL} is the substrate-liquid surface energy, and γ_{LG} is the liquid-air/vacuum surface energy. A positive spreading parameter indicates complete wetting, while a negative spreading parameter indicates partial wetting. If a material is in the partial wetting regime, it is energetically favorable for the film to dewet to reduce contact between the substrate and film. In this case, the spreading parameter can be used to determine the contact angle, θ, between the film and substrate (equation 2).

$$S = E_{substrate,dry} - E_{substrate,wet} \qquad (1)$$

$$S = \gamma_{SG} - (\gamma_{SL} + \gamma_{LG}) \quad OR \quad S = \gamma_{LG}(cos(\theta) - 1) \qquad (2)$$

Figure 2 shows the force balance that is used to determine the wetting angle. Here, γ_{SG} acts as a force stabilizing the film; conversely, γ (γ_{LO}) and γ_{SL} drive the retraction, and eventual breakup of the film. The vertical component of the γ term is balanced by the substrate and can result in deformation. Figure 2 also shows examples of droplets with different ranges of spreading parameters and wetting angles.

Laplace Pressure

As was mentioned earlier, a film can be deposited onto a substrate and exhibit complete coverage of the substrate despite a strongly negative value of S, i.e., an energetic preference to dewet. A metal film with a melting temperature well above room temperature will not spontaneously achieve this lower energy state; it requires an energy input. Dewetting in the solid state is initiated by natural variations in thickness from grain boundaries, voids, or other defects, which create a pressure imbalance. In liquid films, breakup can occur through defects as well, or due to natural thickness fluctuations from thermocapillary effects.

The pressure imbalance created by thickness modulations, can be understood through the Laplace pressure: equation 3. Here, γ is the surface tension of the material and R_1 and R_2 are the radii of curvature, as seen in Figure 3.

$$\Delta p = \gamma C = \gamma \left(\frac{1}{R_1} + \frac{1}{R_2}\right) \quad (3)$$

The radii of curvature of a jet are shown in Figure 3 as an example. R_2 represents the distance from a point on the surface to the center of mass orthogonal to the surface. R_1 represents the curvature of the point by way of an orthogonal distance to the center of an imaginary circle created by continuing the tangent at the point of interest. In Figure 3, R_1 and R_2 are shown as AM and AN, respectively, for point A, and A′M′ and A′N′, respectively, for point A′. R_2, by definition, is always positive, while R_1 is positive when the radius goes towards the bulk (AM), and negative when it faces away from the bulk (A′M′). The directionality of R_1 drives the breakup of a film. The relative magnitude of R_1 and R_2 will determine if the film will breakup. If R_2 dominates (thick film or small perturbation) the film will be stable. Conversely, if R_1 dominates, the film will be unstable, and break up.

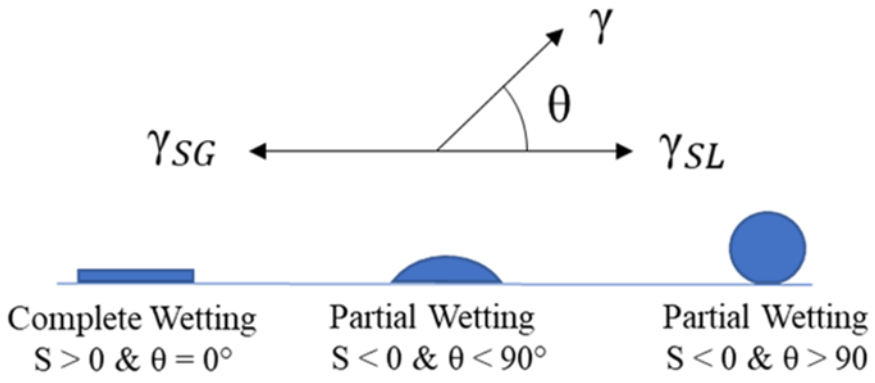

Figure 2: Wetting force balance and representative contact angles

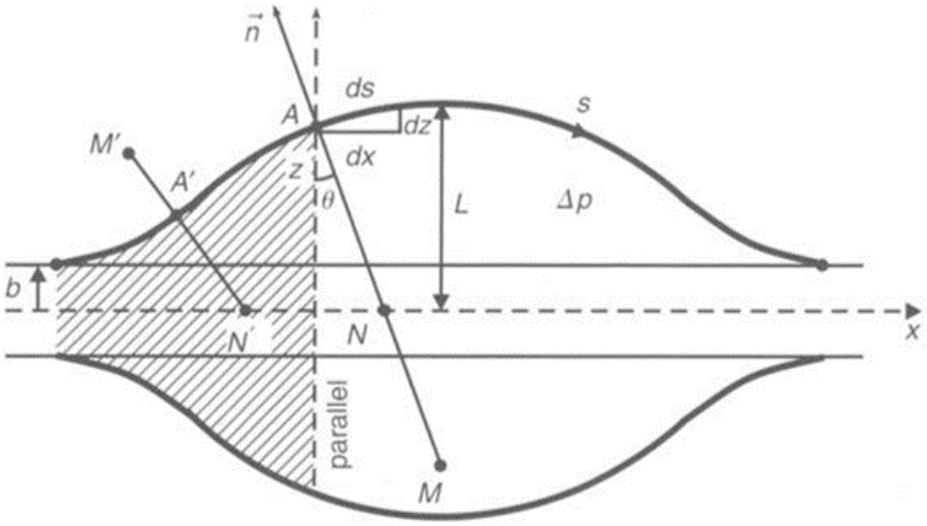

Figure 3: Representation of Laplace pressure in a liquid jet[10]

Rayleigh Plateau Breakup

The Rayleigh Plateau instability is a phenomenon observed in liquid jets in which the jet breaks up into particles. The driving force for this process is minimization of the system's free energy by reducing the surface area. This is accomplished through the Laplace pressure. The process occurs through the presence of natural perturbations in the liquid. When these surface modulations reach a sufficient wavelength, they will be amplified via the Laplace pressure and grow until breakup occurs. Though, the initial theory was developed for liquid jets, similar behavior is observed when introducing a substrate: a thin film that contracts into a jet or rivulet geometry upon heating, will be subject to Rayleigh Plateau instabilities.

Dewetting of Metallic Films

The pioneering research on thin film dewetting was focused on polymers and room temperature liquids due to the relative ease of experiments[10–13]. Additionally, in liquid dewetting, starting with a liquid, as opposed to melting a solid, eliminates potential contributions inherent to many solids, specifically, grain boundaries and strain energy[14]. Later, the dewetting behavior of metal thin films came to the forefront, though the experimental setup is much more complicated due significantly higher temperature requirements. Various methods of heating have been used to heat metals to induce dewetting. These can be broken down into two categories: rapid and gradual heating. The most commonly used rapid heating method is photothermal heating via a pulsed laser. The advantages of pulsed laser heating are several; beyond more rapid processing, pulsed laser heating allows for small area isolation and rapid temperature ramp rates with brief high temperature lifetimes. This is useful as it both reduces the likelihood of substrate/environment reactions and essentially quenches the high temperature morphology.

Mechanism of Breakup

Breakup of a continuous thin film, essentially an infinite 2D surface, can occur through two unique pathways: nucleation of holes or spinodal dewetting. Nucleation is initiated by the creation of dry spots, which accumulate material in a rim formed around them. Though homogenous nucleation is possible, most dry spots preferentially form through heterogenous nucleation at defects in the film or substrate. The rims surrounding the dry spots then break up into particles by way of Rayleigh Plateau instabilities. Conversely, spinodal dewetting involves the spontaneous rupture of the film through the amplification of thermocapillary waves. This process results in a specific, fastest growing wavelength that will dominate the process, and lead to a characteristic spacing between dewet particles. Conversely, nucleation demonstrates large circular patches that can have many different sizes coexisting. Figure 4 shows a model progression from spinodal dewetting to nucleation of holes to limited dewetting.

Spinodal dewetting is only possible in liquid films, thus there is only one pathway for solid dewetting: nucleation of holes. Again, nucleation is likely to occur at a defect, and in polycrystalline solids, grain boundaries are a common initiation point[15]. As with liquids, a rim will form around the nucleated hole, and it will travel into the existing film and grow.

It has been noted that as the hole progresses in size, it leads to a depressed area immediately beyond the rim[15]. When sufficient hole sizes are reached, this depleted area around the rim will create a new hole and rim pairing. Next, through either ‘pinch-off’ or ‘fingering’ instabilities, wires of material are created, which, by way of Rayleigh Plateau like instabilities, break up into particles[16]. Unlike in liquid dewetting, in the solid state, the nucleated holes are rarely circular, and the resulting particles are not as spherical, this leads to a unique dewetting morphology as observed in Figure 5.

Hydrodynamics

The governing equation for the breakup of a thin liquid film, ignoring contributions from potential unmixing behaviors, is shown in equation 4. A thorough description of the hydrodynamic relations can be found in[17,18].

$$3\mu\frac{\partial h}{\partial t} + \gamma\nabla(h^3\nabla\nabla^2 h) + \nabla[h^3\nabla\Pi(h)] = 0 \quad (4)$$

Here, the second and third term show the driving forces, while the first term represents the dissipation due to viscosity. The two driving forces are surface tension and the disjoining pressure, respectively. An additional driving force, gravity, can be ignored when a film is smaller than the capillary length, a threshold that is determined via a ratio of surface tension and gravitational effects:

$$k^{-1} = \left(\frac{\gamma}{\rho g}\right)^{\frac{1}{2}} \quad (5)$$

The variables in equation 4 are as follows: μ = viscosity, h = film thickness, and Π is the disjoining pressure, which can be written as:

$$\Pi(h) = \kappa f(h) = \kappa\left[\left(\frac{h_*}{h}\right)^n - \left(\frac{h_*}{h}\right)^m\right] \quad (6)$$

$$\kappa = S/Mh_* \quad (7)$$

The term, κ, is proportional to the Hamaker constant, which models the long-range forces between the film and substrate, while m and n are constants. The disjoining pressure is analogous to the Leonard-Jones potential, with first term serving as the repulsion term between the liquid film and solid substrate, and the second being the attractive term. The variable, h_*, is the critical thickness where stability is achieved. M is a relation of the constants m and n, and S is the spreading parameter.

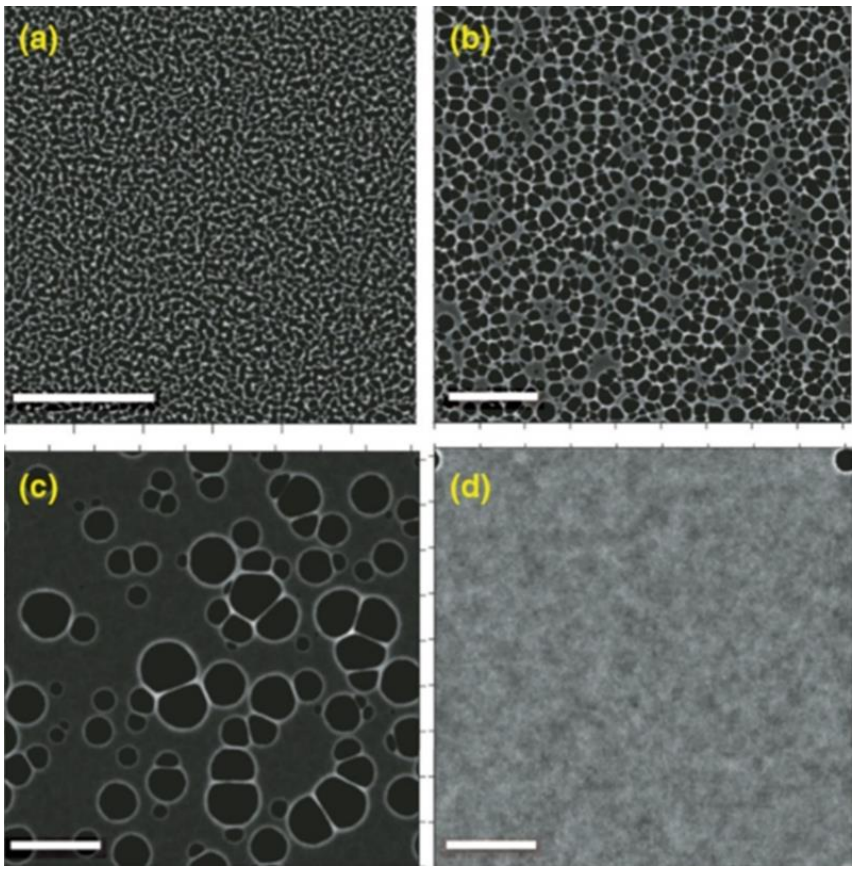

Figure 4: Example of Liquid State Dewetting: a) spinodal dewetting, b) small holes, or coexistence, c) nucleation of holes, d) limited dewetting[19]

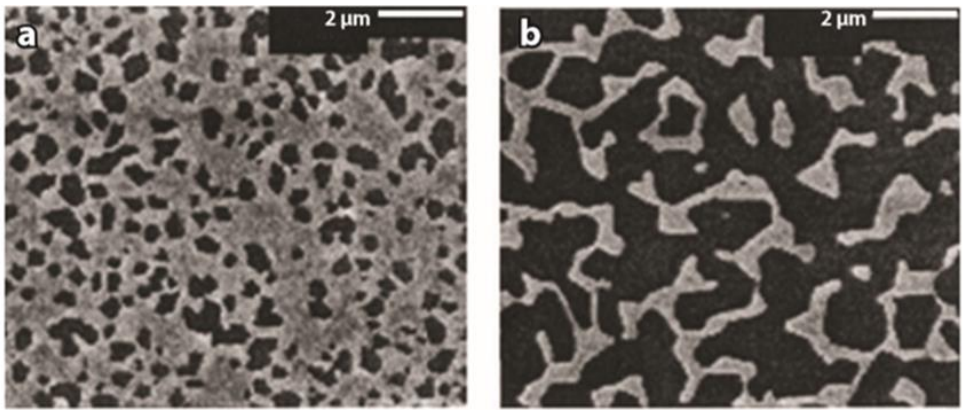

Figure 5: Example of Solid State Dewetting[15]

The film stability is quantified by agitating the film through the assignment of a surface perturbation with a wavenumber of k=2π/λ, where λ is the wavelength of the perturbation. The governing equation can then be solved to find a critical wavelength (λ_c) that describes the onset of instability in the film, as well as a fastest growing wavelength (λ_m). Interestingly, the two are related as: $k_m = \frac{k_c}{\sqrt{2}}$.

To generate a dispersion curve, the growth rate (equation 8) is plotted as a function of the wavenumber; Figure 6 shows an example dispersion behavior. The critical wavenumber is determined by a transition to a positive growth rate, i.e. the x intercept. The fastest growing wavenumber can be found by solving for the maximum in the dispersion relation; the solution is shown in equation 9.

$$\beta = h_0^3 k^2 (k_c^4 - k^2) \quad (8)$$

$$\beta_m = \frac{1}{4} h_0^3 k_c^4 \quad (9)$$

Solid State Dynamics

Dewetting in the solid state occurs through solid-solid diffusion, thus the kinetics are significantly different from the previously discussed liquid state dewetting. In a review of solid state dewetting by Thompson[15], several relations were included. First, the time for nucleation of holes is shown in equation 10. Here, D_s is the surface diffusivity and h is the film thickness.

$$t_n \propto \frac{h^4}{D_s} \quad (10)$$

Next, the resulting dewet area is expressed by equation 11. Here, N_b is the number of holes, τ is the time at which the first hole nucleates, t is time, and $\dot{r}_{dewet}$ is shown in equation 12.

$$X_{dewet} = 1 - exp[N_b \pi \dot{r}_{dewet}^2 (t - \tau)^2] \quad (11)$$

$$\dot{r}_{dewet} \propto \frac{D}{b^3} \quad (12)$$

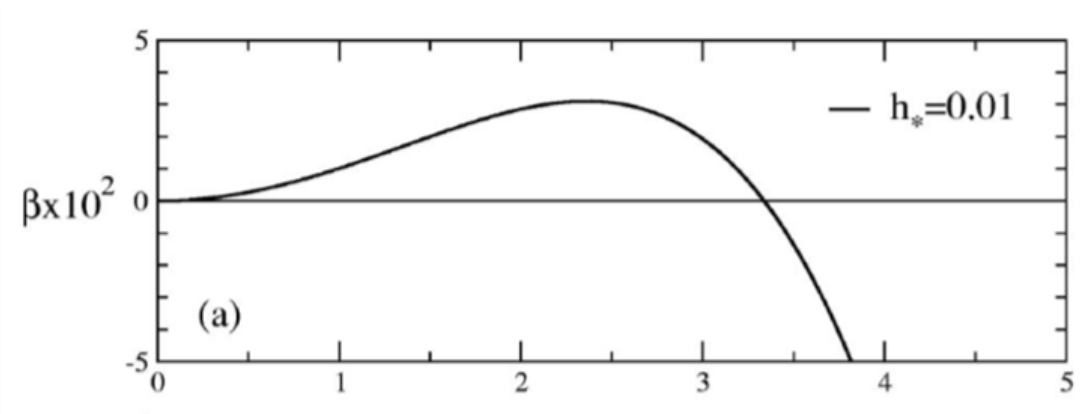

Figure 6: Example Dispersion Curve[14]

Finally, when hole nucleation is rapid, τ is small, the relationship for the rate of deweting, in terms of area affected can be simplified to equation 13. Here, Q_S is the activation energy for surface self-diffusion.

$$\dot{X}_{dewet} \propto \frac{exp\left(\frac{-Q_S}{kT}\right)}{h^3} t; \quad (13)$$

Plasmonics

In most bulk metals, a polished surface will exhibit a mirror like appearance. This is because the majority of metals reflect the visible spectrum. The inherent metallic electron gas prohibits propagation of electromagnetic waves below a characteristic frequency known as the plasma frequency, typically in the ultraviolet range. A few metals such as Cu, which has an orange color, deviate from this behavior due to interband transitions at characteristic energies within the visible spectrum: ~2 eV for Cu. This same phenomenon occurs in Au at ~2.4 eV, and thus gives Au its yellow color. Meanwhile metals such as Ag and Al have interband transitions that are above or below, respectively, the visible spectrum, and thus maintain the reflective grey appearance.

Contrary to the bulk behaviors mentioned above, when the dimensions of metals are significantly reduced (on the nanoscale) the interactions with light are fundamentally altered. This leads to properties pertaining to the plasmon, the quantized collective oscillation of charged particles, in this case: the metallic free electron gas. There are three primary classifications of the plasmon: the bulk, surface plasmon polariton (SPP), and localized surface plasmon (LSPR). A representation is demonstrated in Figure 7.

The bulk plasmon is a longitudinal oscillation, which means that the oscillation is parallel to the propagation of light, and thus cannot be excited by light. Instead, the bulk plasmon is excited by particle impact, and is characterized by methods such as electron energy loss spectroscopy (EELS).

Unlike the bulk plasmon, the SPP is, as the name implies, a surface phenomenon; the surface plasmon requires an interface between a thin conducting material and a dielectric for propagation to occur. The SPP is a transverse mode and can be optically excited, though prisms or gratings are required for phase matching.

Localized Surface Plasmon

When the lateral dimensions of a plasmonic metal are also reduced to the nanoscale along with the thickness, LSPR modes can be excited by an electron or the electric field of a photon. Here, there is not a single resonance associated with a particular nanostructure, instead there are a collection of electron oscillation configurations, with characteristic frequencies at which they occur. The energy at which the LSPR modes exist is determined not only by the dielectric properties of the material (and substrate), but also by the structure's physical dimensions. This means that the resonance can readily be tuned by altering a specific dimension or the overall shape of plasmonic nanostructure.

Individual Nanoparticle

The lowest energy LSPR mode (m = 1) is the dipole mode in which there are two opposite poles with the physical separation between them maximized, i.e. at either end of a rod or separated by a full diameter in a sphere (As seen in Figure 8 and Figure 9. The energy of this LSPR dipole mode can be easily altered by increasing (red shift) or decreasing (blue shift) the size of the nanoparticle. Beyond the m = 1 mode, at progressively higher energies, many additional modes (m = 2, 3, etc.) can exist with increasingly complicated polarization states. This will continue up until a critical energy is reached where a uniform excitation across the nanoparticle exists. Figure 8 demonstrates how these modes develop in a nanosphere, where a nomenclature of "l" is used instead of "m" to

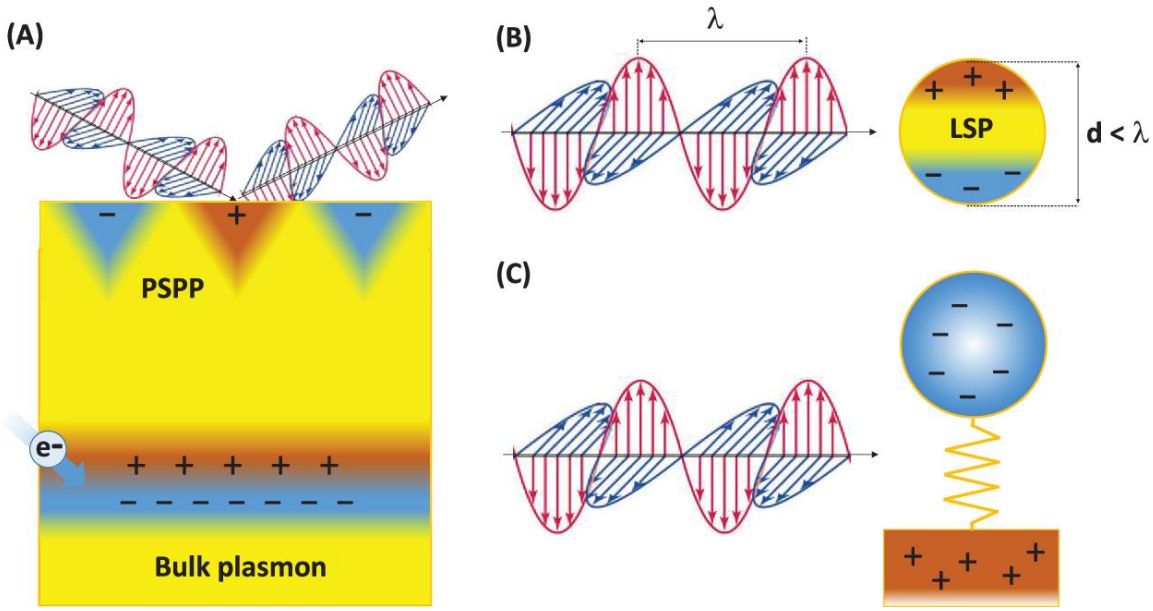

Figure 7: Representation of the surface plasmon polariton, bulk plasmon, and localized surface plasmon[19]

represent the modes. Figure 9 shows the LSPR modes for a rod structure. It is apparent that some of these modes have a net electric field associated with them, while others do not. The dipole clearly has a large net electric field with two nodes of opposite signs. The m = 2 mode, also called the quadrupole, on the other hand, has no net electric field as the two ends cancel one another out. This is an important feature of LSPR modes when considering measurement methods. Optical measurement techniques, in which photons are used to excite these modes, can only detect modes with a net electric field, so with these techniques the quadrupole is not observable. This issue can be remedied to an extent by introducing retardation effects through tilting the structure such that electric field of the photon is no longer fully in the plane of the structure. An electron, unlike a photon, can excite optically dark modes, and techniques such as EELS can be used to characterize all LSPR modes. There are also techniques, notably stimulated electron energy loss/gain spectroscopy (sEELS and sEEGS) that use both electrons and photons, via a laser, simultaneously to characterize the LSPR modes.

Plasmonic Coupling

Individual plasmonic structures with similar LSPR resonance energies can also interact with one another if they are in close enough proximity. Coupling between multiple structures will lead to the hybridization of their individual modes into additional modes above and below the resonance energy of the single structure. A representation of this behavior can be found in Figure 10. Here the dipole mode of the individual rods have hybridized into two unique modes. One corresponding to an in phase configuration and the other being out of phase. Also in Figure 10, coupled structures can be arranged in ring structures in which the in phase mode generates a circulating current which induces a magnetic field. The signature for the in phase and out of phase mode varies as can be seen in Figure 10: the out of phase configuration produces a bright area, indication of the near

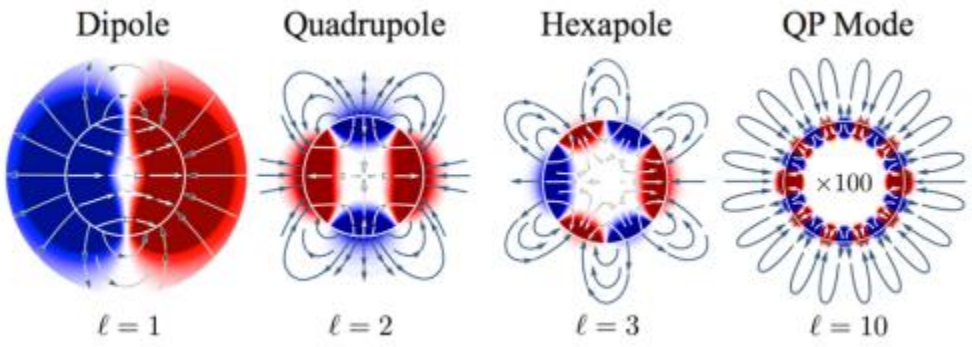

Figure 8: Localized surface plasmon modes in a spherical nanoparticle[20]

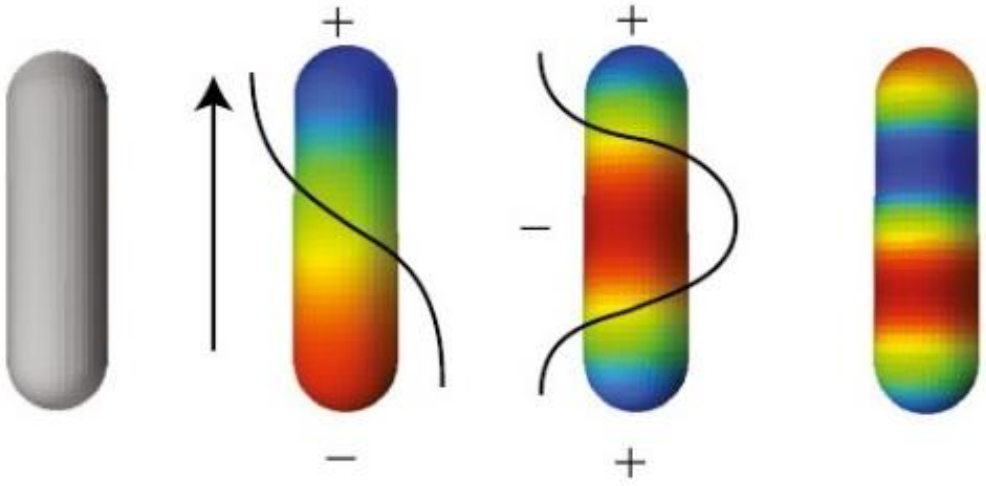

Figure 9: Representation of the localized surface plasmon modes in a rod structure[21]

field, at the vertex, while the in phase configuration is strongest at the ends of the rods. The number of available modes can be increased by increasing the number of nanostructures that are hybridizing.

Magnetism

The magnetic properties of a material are dependent on the electron configuration, namely unpaired electrons dominate the magnetic behavior of a material. This leads to several different types of magnetic responses: paramagnetism, diamagnetism, ferromagnetism, ferrimagnetism, and antiferromagnetism. A representation of these different behaviors can be found in Figure 11.

Types of magnetism

Diamagnetism is predominately observed in materials with non-magnetic individual atoms, due to the lack of unpaired electrons. A traditional diamagnetic material demonstrates a negative susceptibility, a measure of the induced magnetization of a material under an applied field, while showing minimal sensitivity to changes in temperature. A negative susceptibility implies that the induced magnetization in the material is opposite the applied field. The phenomenon of diamagnetism is caused by a change in the electron orbital motion induced by the applied field. Diamagnetism is present in all materials, but is dominated by the other forms of magnetism, listed below, in materials that possess these behaviors.

Paramagnetism occurs in materials with unpaired electrons that interact weakly with an applied magnetic field. Unlike diamagnetic materials, paramagnetic materials have a positive susceptibility, meaning the induced magnetic moment aligns with the magnetic field. Increasing the applied magnetic field will increase the internal magnetization, though the susceptibility of paramagnetic materials is rather small. Thermal agitation, caused by increasing the temperature,

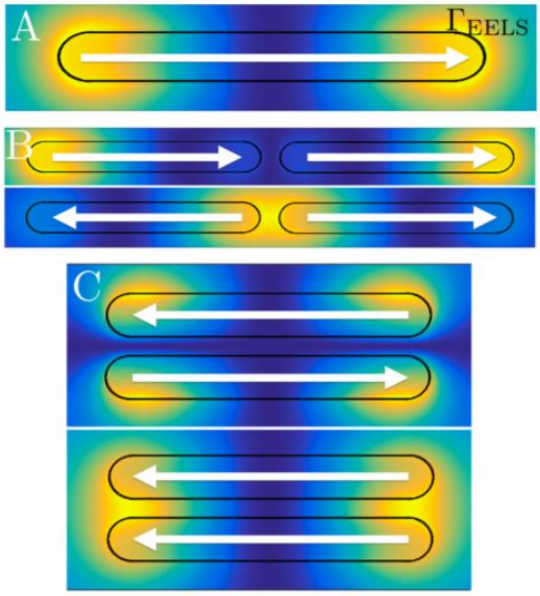

signifying that it is the net dipole mode. In mode β, rather than seeing nodal structure resulting from pairs of collinear dipoles, the EEL probability is more localized to the outer particles in both junctions. This is because the peak in the spectrum corresponds to two possible orientations of the dipole plasmon on the central particle. Because both are equally polarizable, the EEL map encodes the superposition of these two modes. Mode γ does not contain nodal structure or asymmetry in the EEL probability and is the maximally out-of-phase dipolar plasmon mode.

The EEL spectrum and corresponding maps of the triangular nanorod trimer system are shown in Figure 7. The spectrum,

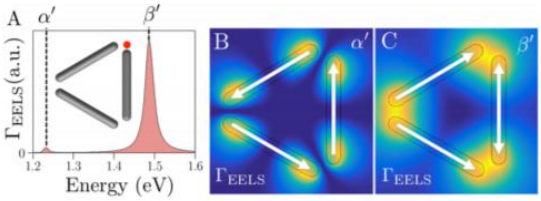

Figure 7. Simulated EEL spectrum and maps of a silver nanorod trimer arranged in an equilateral triangle. Each rod is 80 nm in length and 10 nm in diameter. (A) EEL spectrum of the trimer computed at

Figure 10: Coupling of individual plasmon rods into dimer and trimer structures, indicating the different hybridization modes[22]

leads to a reduction in susceptibility with increasing temperature, and the loss of magnetization in the absence of an applied field.

Antiferromagnetic materials have a specific temperature, the Neel temperature where an important transition occurs. Below this temperature there is an antiparallel alignment of magnetic moments that counteract each other and result in a significant reduction in susceptibility. Above the Neel temperature, thermal agitation is sufficient to prevent the formation of antiparallel magnetic moments, and thus all moments align with the applied field, this leads to a behavior similar to paramagnetism.

Ferrimagnetism is very similar to antiferromagnetism with a key difference. Below the critical ordering temperature, instead of antiparallel moments entirely canceling out, there remains a net magnetization. Below this temperature, ferrimagnetic materials behave close to that of a ferromagnetic material.

Ferromagnetism like paramagnetism is associated with a positive susceptibility, and in fact ferromagnetic materials do behave like a paramagnet at temperatures above a critical temperature called the Curie temperature. Below this temperature, however, a ferromagnetic material will possess magnetization in the absence of an applied field. On the macroscopic scale, this magnetization can be unobservable due to the formation of what are called magnetic domains.

Magnetic Domains and Hysteresis Behavior

In order to understand the behavior of ferromagnets, the behavior of magnetic domains must be considered. The exchange interactions present in a ferromagnetic material, which favor the alignment of all magnetic moments suggests that magnetization via a single domain should exist in the absence of an external magnetic field. This configuration, however, creates a large magnetostatic energy. The formation of domains within the material possessing moments of

Type	Example	Atomic/Magnetic Behaviour		
Diamagnetism	Inert gases; many metals eg Au, Cu, Hg; non-metallic elements e.g. B, Si, P, S; many ions e.g. Na^+, Cl^- & their salts; diatomic molecules e.g. H_2, N_2; H_2O; most organic compounds	Atoms have no magnetic moment. Susceptibility is small & negative, -10^{-6} to -10^{-5}	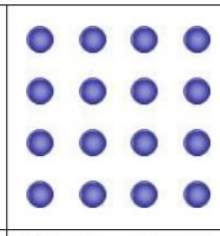	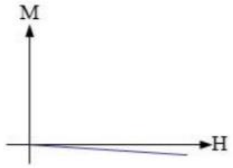
Paramagnetism	Some metals, e.g. Al; some diatomic gases, e.g. O_2, NO; ions of transition metals and rare earth metals, and their salts; rare earth oxides.	Atoms have randomly oriented magnetic moments. Susceptibility is small & positive, $+10^{-5}$ to $+10^{-3}$	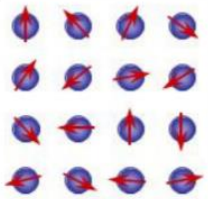	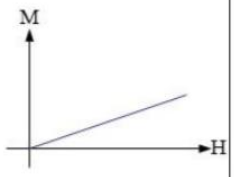
Ferromagnetism	Transition metals Fe, H, Co, Ni; rare earths with $64 \leq Z \leq 69$; alloys of ferromagnetic elements; some alloys of Mn, e.g. MnBi, Cu_2MnAl.	Atoms have parallel aligned magnetic moments. Susceptibility is large (below T_C)	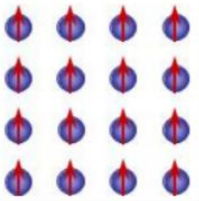	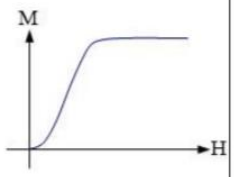
Antiferromagnetism	Transition metals Mn, Cr & many of their compound, e.g. MnO, CoO, NiO, Cr_2O_3, MnS, MnSe, $CuCl_2$.	Atoms have anti-parallel aligned magnetic moments. Susceptibility is small & positive, $+10^{-5}$ to $+10^{-3}$	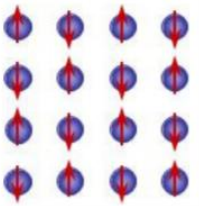	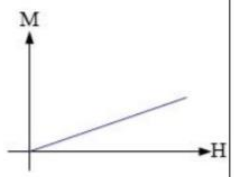
Ferrimagnetism	Fe_3O_4 (magnetite); γ-Fe_2O_3 (maghemite); mixed oxides of iron and other elements such as Sr ferrite.	Atoms have mixed parallel and anti-parallel aligned magnetic moments. Susceptibility is large (below T_C)	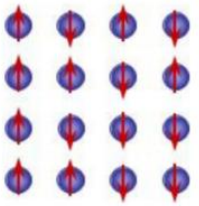	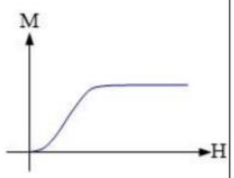

Figure 11: The various types of magnetism, with representations of the individual atomic behavior and M vs H curves[23]

opposite directions reduces this magnetostatic energy, but is unfavorable in terms of exchange interactions. Because the exchange interactions are highly localized to the immediate neighbors, the creation of a gradient in magnetic moment direction in between two domains, the domain wall, provides a compromise. The characteristic length that optimizes the long range dipolar interactions and the short range exchange interactions is termed the exchange length, and length provides the energetically favorable domain wall length that separates two regions of opposite moment. There is one additional material specific consideration, magnetocrystaline anisotropy, that favors specific preferred directions for magnetic orientation determined by the element and crystal structure. This anisotropy has a profound influence on the domain wall formation because, whereas the domains are oriented along an easy direction, the majority of the wall will be off of the preferred magnetic orientations. Thus, materials with exceedingly larger anisotropy will have much smaller domain walls than those with small anisotropy. It is also possible, when individual grains or nanostructures are sufficiently small, that single domains can exist. This is a necessary characteristic for another form of magnetism called superparamagnetism. A material is said to be superparamagnetic when single domains are present, and the magnetic anisotropy energy is close to the thermal energy. This leads to a specific temperature, the blocking temperature, where the material no longer behaves like a ferromagnet because thermal fluctuations are sufficient to remove any magnetization in the absence of an applied field.

The magnetic hysteresis curve, Figure 12, is a convenient way to express a material's magnetic properties. A demagnetized ferromagnetic material, like a paramagnet or superparamagnet, will possess zero net magnetization in the absence of an applied field. When a positive field is applied, the magnetic moments within these materials will begin aligning with the applied field, and the magnetization indicated on the y-axis of Figure 12, will increase. In a ferromagnetic material, this

process is dictated by the domains: those domains that are already oriented with the applied field will grow and eventually reach the saturation magnetization where all moments are aligned. Simultaneously new magnetic domains with the preferred orientation will form via nucleation at defects in the material, and then proceed to grow. At the saturation point, in which the magnetization reaches a maximum, there are no more domains as all moments have the same orientation.

Reversing the applied field to the negative saturation field, and then back to the positive saturation field creates the hysteresis loop. There a several characteristic points that are reached during this process, namely the point at which the applied field returns to zero, and the point at which the magnetization returns to zero. In a ferromagnetic material these two points will not be the same: the magnitude of the magnetization at zero applied field is termed the remanence, while the field at which magnetization is removed is termed the coercive field or coercivity. Reversal of the magnetic domains when the applied field is reversed is accomplished through various methods. Domains can rotate to align with the applied field, domains can nucleate at defects with the appropriate orientation, and domains can grow through the motion of the domain walls at the expense of misaligned domains. Interestingly, defects within the material have somewhat of a contradictory influence on the reversal behavior. As has been mentioned, defects are important for initiating nucleation of new domains; however, defects also act as pinning centers to impede domain wall movement.

Phase Diagrams of Ag-Ni and Au-Co

The calculated phase diagrams for both the Ag-Ni and Au-Co systems are shown in Figure 13 and Figure 14. The Ag-Ni phase diagram demonstrates complete solid immiscibility with a liquid miscibility gap up to ~2600 K. Pure Ag melts first at 1234.2 K, and then pure Ni at 1728.24 K.

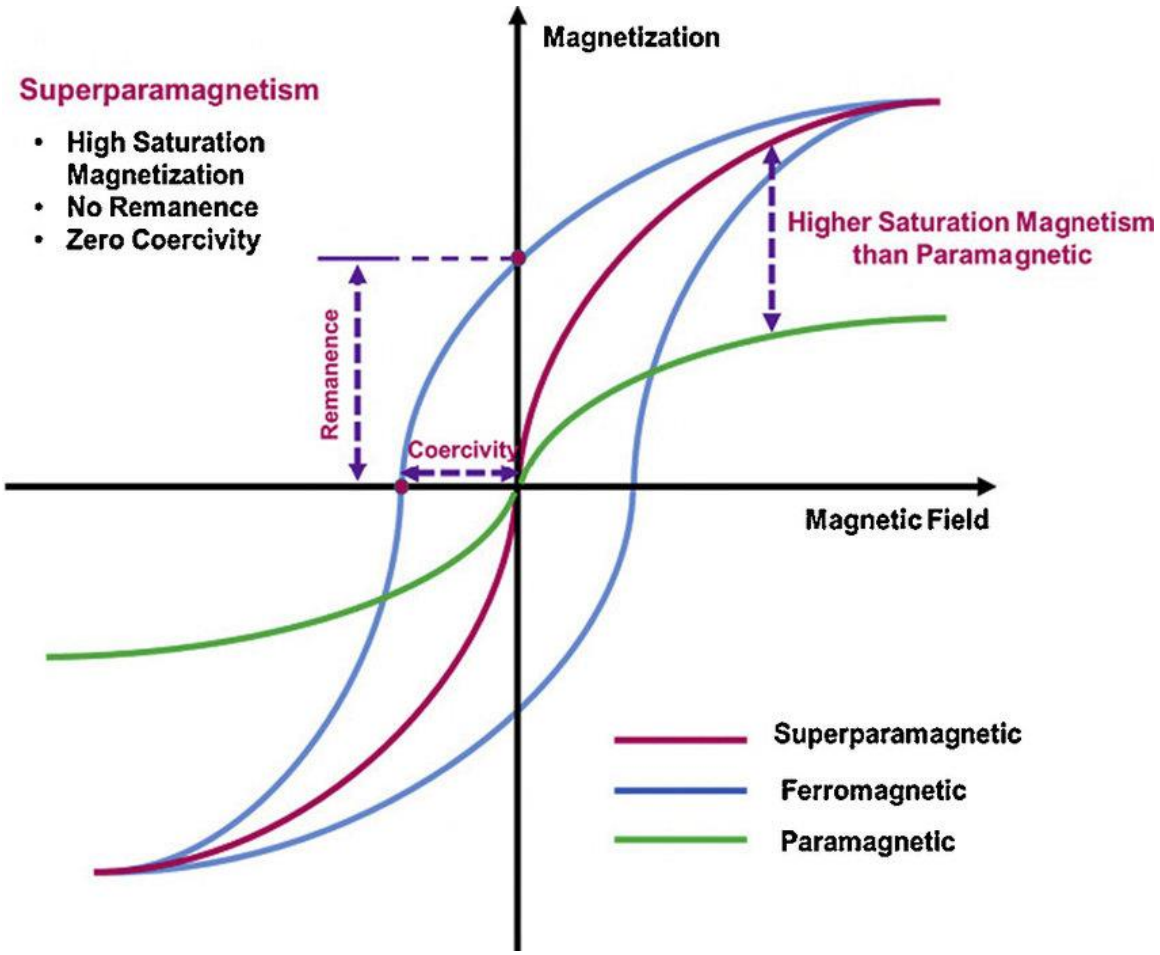

Figure 12: An example M vs H hysteresis curve indicating the coercivity and remanence in a ferromagnetic material, as well as the behavior of a paramagnetic and superparamagnetic material[24]

Between these two temperatures there exists near complete unmixing of the liquid and solid phases. The Au-Co phase diagram also has a region of complete solid immiscibility, below a temperature of 700 K. In this region Co exists in a hexagonal close packed (HCP) crystal structure while Au is face centered cubic (FCC). Above this temperature a small region of miscibility originates on the Au rich side, where miscibility increases with temperature. In the immiscible portion of this temperature range, both Co and Au are FCC. Finally, there is a eutectic point at ~1250 K at 25 at. % Au.

Literature Review

Additional review of literature beyond what is discussed here can be found in the introduction sections of Chapters I-IV.

Dewetting

2D Continuous Film Dewetting

The most commonly studied metal dewetting configuration is a continuous film deposited on a solid substrate. The primary reason for this is the minimal sample preparation requirements, which make experiments easy to perform. Additionally, the simplistic sample preparation makes continuous films a cheaper option for industrial applications.

Single Component

Within the scope of metallic continuous thin film dewetting, the most prevalent area of research is in single component systems. Some of the frequently studied metals include: Au[14,25–28], Ag[25,29–31], Ni[14,32–35], Cu[14,36], and Pt[37,38]. Most of this work has been focused on two topics: 1) understanding and controlling the mechanism of film breakup, and 2) regulating the size and spacing of the dewet particles.

Examination of the two liquid dewetting pathways has been conducted experimentaly[14,28,41] and computationally[28,42,43]. Film thickness was found to be the obvious parameter to program the desired dewetting mechanism: thinner films will dewet through spinodal dewetting, and thicker films through nucleation. However, defects and impurities on the substrate or in the film can result in nucleation occurring in thinner films. Interestingly, all of these studies observed a regime of coexistence between nucleation and spinodal dewetting. Figure 15 shows results from the experimental studies demonstrating the coexistence of the two mechanisms. Regions of nucleation are seen as the large circular dry spots, some of which have begun to break up into particles. The remainder of the sample exhibits a complex system of thickness modulations, representative of spinodal dewetting. The images on the right[8] demonstrate the surface modulations by slightly defocusing the microscope. On the computational side, Nguyen et al.[42] make an intriguing assertation that both homogenous nucleation and spinodal decomposition have the same origin in thin liquid films, thermal fluctuations. It was thus reasoned that it is the development process, beyond initiation, that differentiates the two pathways. The size of a nanoparticle affects its plasmonic behavior, and thus demonstrating control of particle size is of significant interest. Ruffino et al.[25] observed that laser fluence can be used to change the radius and spacing of particles in a nucleation regime: higher laser fluences led to larger particles. Also related to laser fluence, it was found that for gold films there is a minimum in laser fluence required to initiate dewetting at ~20 nm[26]. This was determined to be due to laser interactions with the film: for instance, in ultrathin films below the penetration depth at the laser wavelength, corrections for the thickness dependent reflectance must be taken into consideration. Oh et al.[29] found that increasing the thickness of Ag films led to larger, more sparse particles. Similar results have been reported elsewhere[30]. Finally, effort has also been devoted to examining the spacing and size of particles as

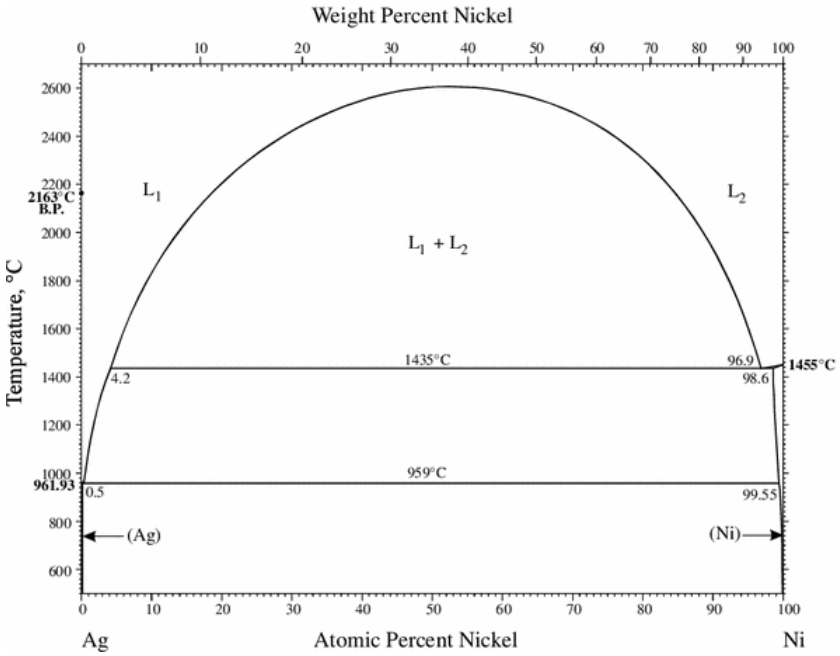

Figure 13: Phase diagram for the Ag-Ni material system[39]

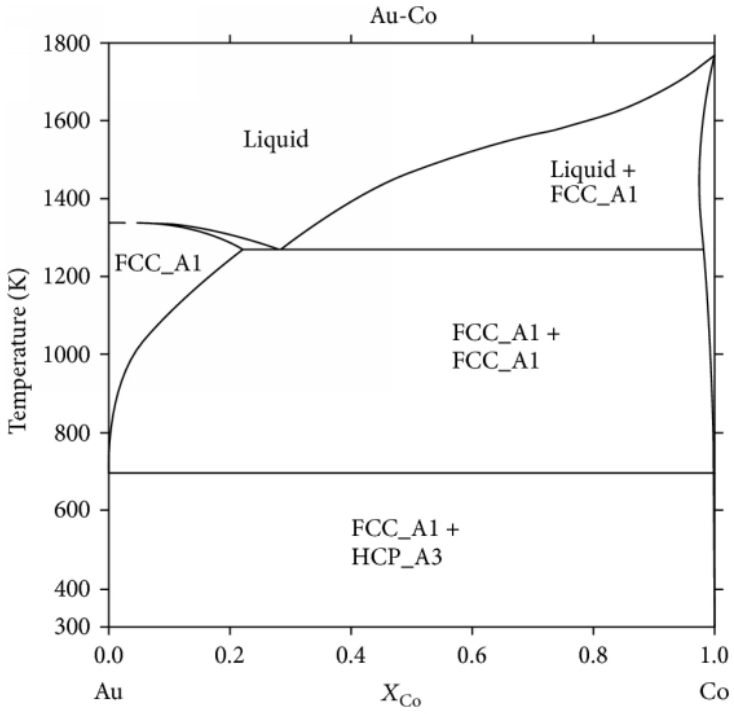

Figure 14: Phase diagram for the Au-Co material system[40]

a function of dewetting progression, and attempting to reconcile the fastest growing wavelength experimentally and computationally[36].

Multicomponent

Although much research exists studying single component metallic dewetting, the sheer number of material systems and phase equilibrium behaviors ensure that there remains significant work to be done on multicomponent metallic dewetting. Introducing a second component creates challenges for various reasons. First, adding a second material further complicates the determination of material specific properties: surface tension, viscosity, and density. These properties are now not only temperature dependent, but also composition dependent. Secondly, the atomic interactions of dissimilar atoms create chemical instabilities that can compete or synergize with the dewetting dynamics. Finally, due to differences in melting temperatures and vapor pressures, special consideration is required when heating the material.

Some examples of multicomponent (binary) material systems that have been previously studied include: Ag-Au[44–46], Ag-Co[47–50], Ag-Pd[51], Au-Co[47], Au-Pd[52], Cu-Co[53], Cu-Ni[54,55],Co-Pt[56], Ni-Pt[57], and Pd-Pt[58]. Of these material systems: Au-Ag, Cu-Ni, and Au-Pd are miscible, Ag-Co, Au-Co, and Cu-Co are mostly insoluble, Ag-Pd and Pd-Pt are mostly soluble with small miscibility gaps, and Co-Pt, Ni-Pt demonstrate a more complex phase equilibrium.

Miscible systems

When comparing the miscible systems[44–46,51,54,55], it was found that regardless of initial film configuration (bi-layer or co-sputtered), given sufficient thermal energy to fully dewet, the resultant particles were well mixed. Both laser excitation[44,54,55] and traditional annealling[44,45,51] were used to induce both liquid and solid dewetting, respectively. Although the particle shape and distribution varied between solid and liquid dewetting, the resulting particles remained completely

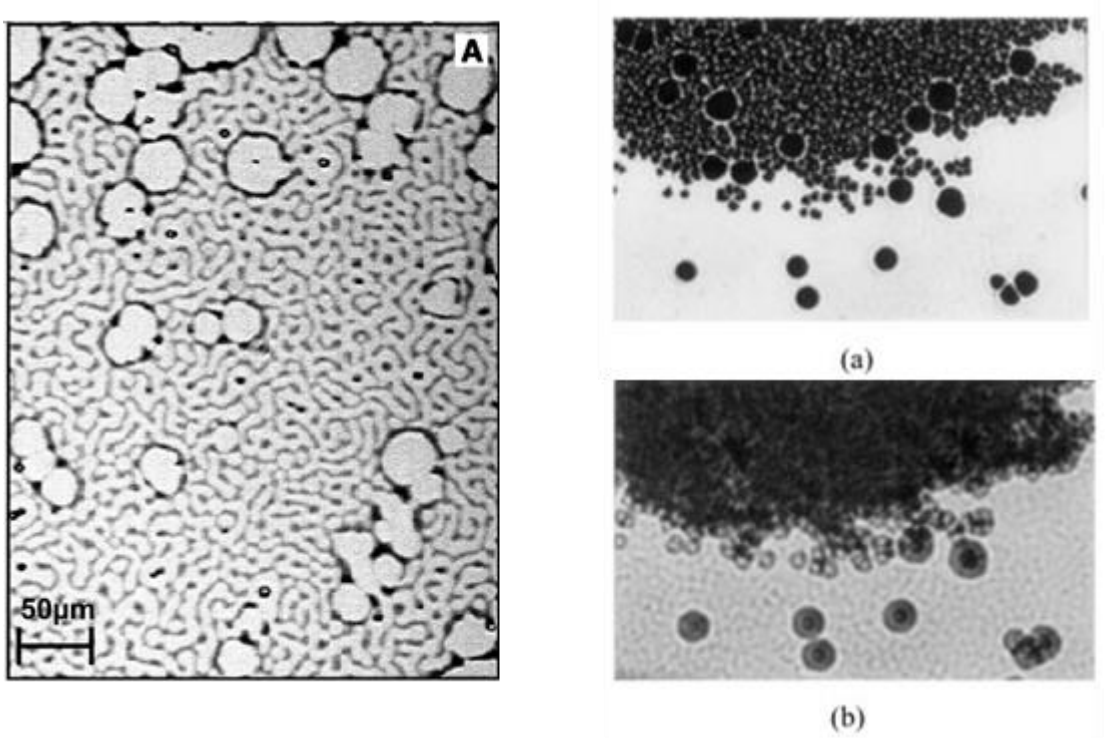

Figure 15: Coexistence of Spinodal Dewetting and Nucleation[8]

mixed in all studies. An insight from the bi-layer studies was the effect of different top layers. Using Au as a top layer instead of Ag led to a reduction in reflectance[46], and using a top layer of Ag instead of Pd led to more evaporation[51]. Finally, Wu et all[54] found that altering the composition in the Cu-Ni system allowed for programing the dewetting mode. For a constant film thickness, pure Cu demonstrated spinodal dewetting, pure Ni broke up by nucleation, and a $Cu_{50}Ni_{50}$ co-sputtered film dewetted via spinodal dewetting. However, increasing the relative composition of Ni shifted the behavior back to nucleation.

Immiscible systems

In immiscible systems[47–50,53], the phase separation interplay with the dewetting dynamics becomes much more difficult to predict. As with miscible systems, the vast majority of research has been devoted to bilayer configurations[47–50], though mixed alloys, through co-sputtering, have also been studied[53]. All studies discussed in this section utilized pulsed laser induced dewetting. Sachan et. al.[47] found that Ag-Co and Au-Co, both immiscible in the solid phase, demonstrated significantly different particle morphologies. Ag-Co formed half-half particles with the fully separated Co and Ag in hemisphere configurations connected at the center (Figure 16). Conversely, Au-Co formed particles with fine separated clusters of Au and Co in Figure 17. In another study by Sachan et. al.[48], the Ag-Co system was further investigated. Here, a SiO2 substrate was used instead of C on mica, which significantly altered the dewetting behavior. Resultant particles demonstrated an intricate morphology consisting of a top layer of Co, a bottom layer of Ag, and an intermediate layer of finely dispersed separated Co and Ag clusters. This variation in morphology can be seen in Figure 18. Yet another study from this group[50] found that Ag-Co could dewet into the same finely dispersed clusters of Ag and Co as was observed in Au-Co. Thus, Ag-Co was shown to dewet in three distinct morphologies when using three different substrates. In a separate study,

McKeown et al.[53] investigated the Co-Cu system using co-sputtering to create a nanocrystalline alloy. As shown in Figure 17, various particle morphologies were observed in a single sample depending on their size. The large particles were found to possess a core-shell structure, with the lower surface energy material, Cu, acting as the shell. Intermediate sized particles took on a half-half or a so-called Janus geometry, while the smallest particles appeared to be exclusively Co. This study was conducted on a TEM membrane, leading to a slower quench, and providing more opportunity to create higher order particle morphologies. It was suggested that the cooling rate was slow enough that the higher melting temperature Co solidified prior to the Cu and allowed for the Cu to wet its surface prior to freezing.

Directed Assembly

Although self-assembly, specifically in the spinodal dewetting regime, can produce ordered particle distributions with a correlated size and spacing, patterning a sample prior to dewetting allows for the creation of much higher order nanostructures. There are two primary categories of patterning that have been used in metallic dewetting: direct writing of the metal film, and templating of the substrate prior to metal deposition. Patterning of the metal film is most commonly done by way of electron beam lithography, though other techniques such as ion beam milling can also be used. Templating is mostly conducted by way of chemical etching.

Templated Substrate

The most commonly used technique for patterning a substrate is through the use of a KOH wet etch on a Si wafer with a lithographically patterned mask of SiN_4[56,59,60]. This method has demonstrated the ability to create ordered arrays of nanoparticles when the designed relationship between the substrate trench geometry and metal film thickness are optimized. One study[61] focused on this relationship, and found a critical size for the template to create a single particle

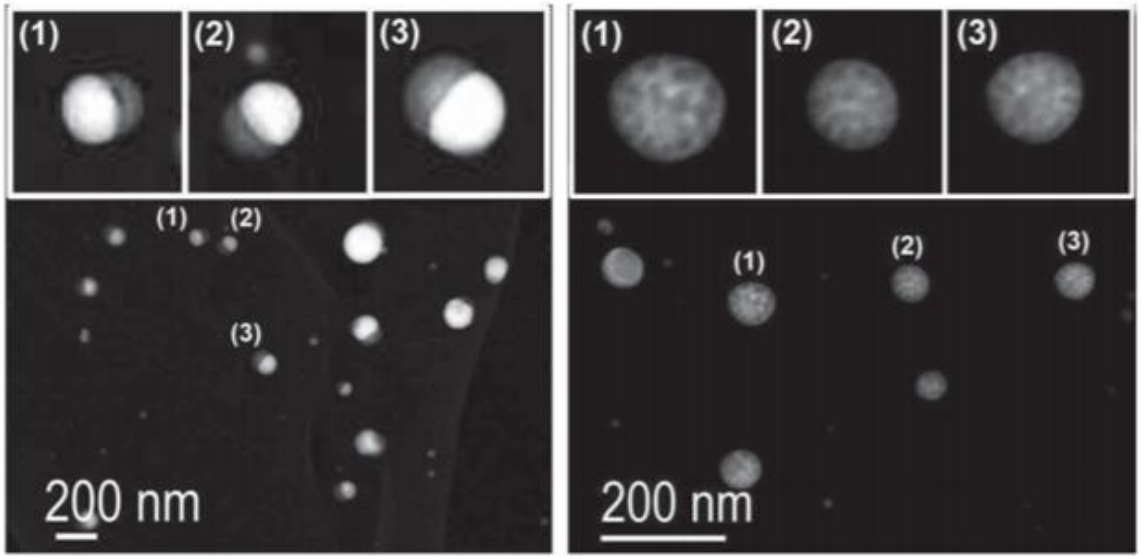

Figure 16: Half-half particles (Ag-Co) and fine phase separation (Au-Co)[47]

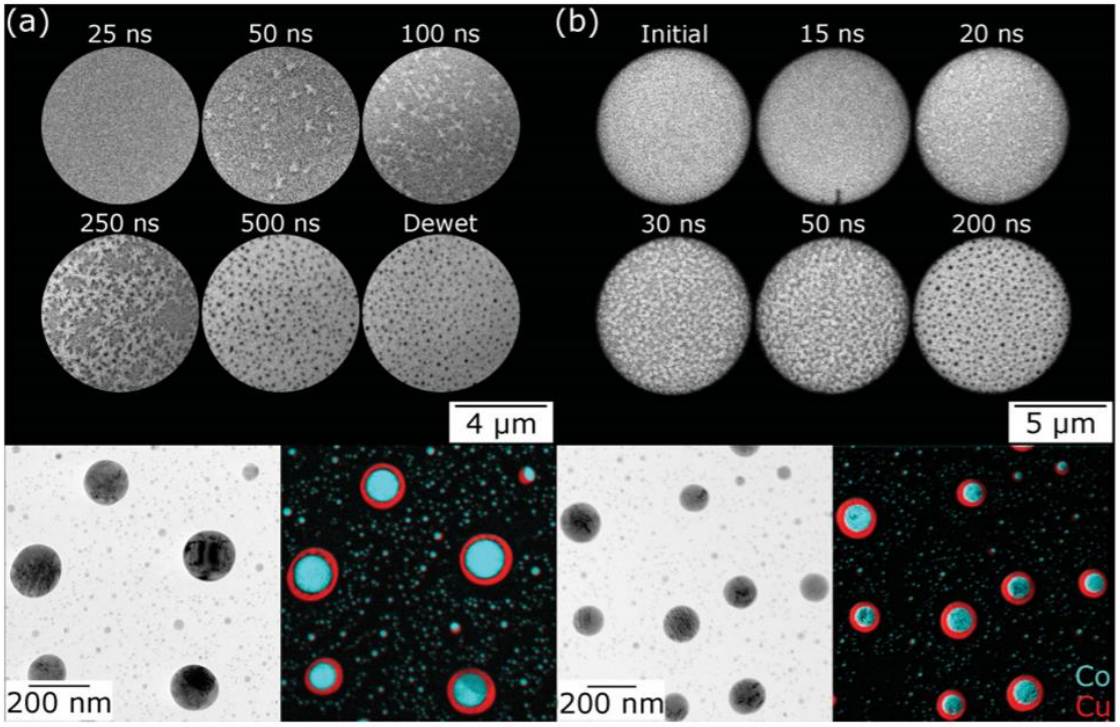

Figure 17: Resultant particles from dewetting a co-sputtered Co-Cu thin film[53]

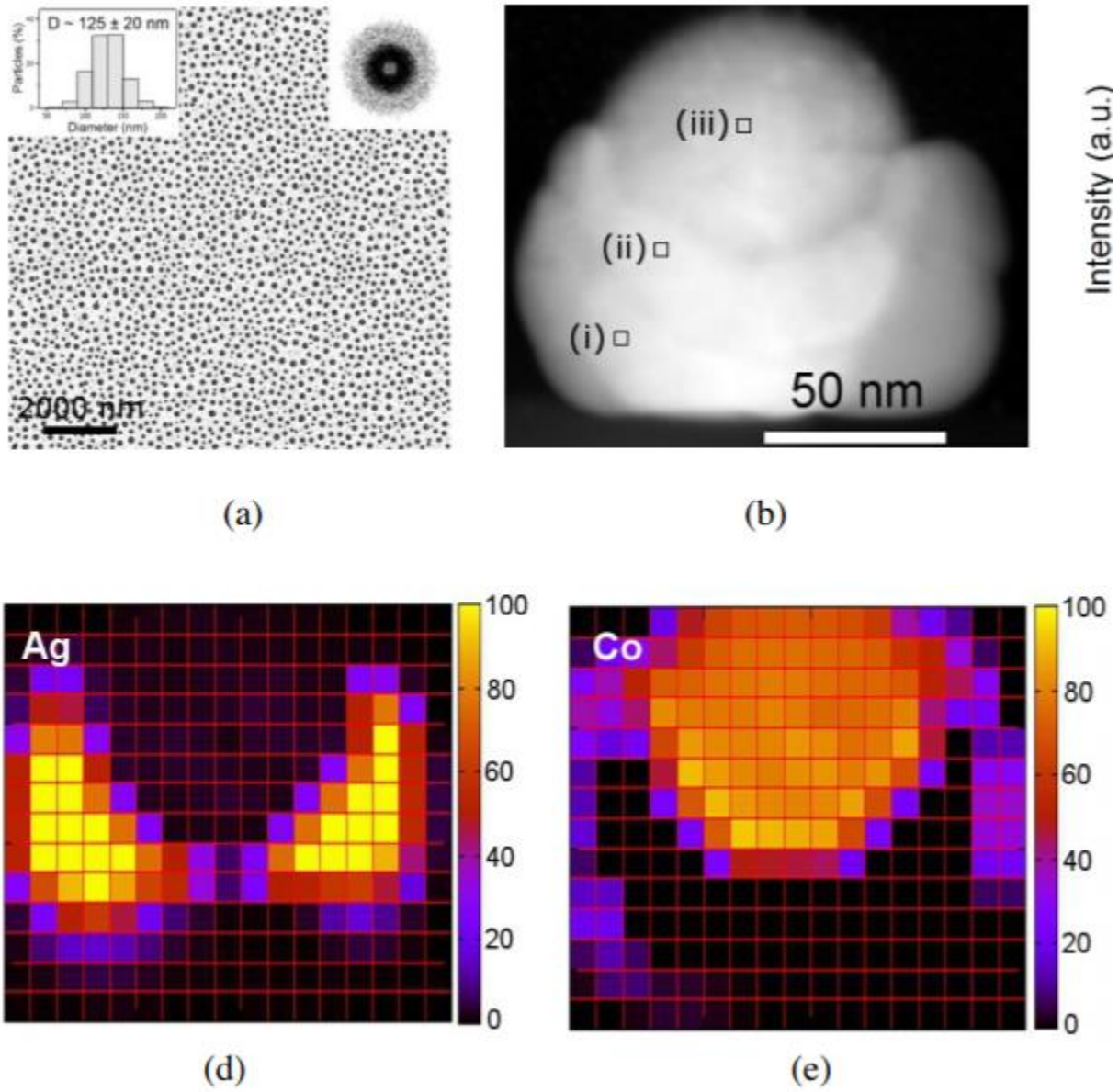

Figure 18: Complex particle morphology of Ag-Co[48]

versus the breakup into multiple drops. Alternately, anodic aluminum oxide (AAO), or monolayer colloidal crystals (MCC) with hexagonally arranged pores have been used as a substrate, and successfully demonstrated particle ordering[62,63]. In another study, a Ni template with square openings was clamped onto an Au film prior to dewetting, and successfully produced ordered nanoparticles[64]. Finally, TiO_2 nanotubes have also been used to form a template and created ordered dewetting[65].

Lithographic Patterning

Two instabilities can be leveraged in patterned dewetting: collapse into a single droplet and breakup of into multiple droplets. Dewetting of lithographically patterned metal films has been studied previously, however, the literature is relatively limited. Some of the earliest work, investigated the dewetting behavior of simple shapes of single component systems [33,66,67]. Here, it was found that shapes such as circles, squares, and triangles, depending on their geometry, can dewet into a single particle or a more complex distribution of particles.

After the initial exploration, the next step was to understand the mechanism of the instabilities driving the particle formation. First the breakup of a shape, specifically wires and rings, was investigated[1,68,69]. Figure 19 shows some results from these studies. Here, through experimental, simulation, and theoretical work, it was found that rings can break up via the Rayleigh Plateau instability, given the width of the rings is small enough that the ring can agglomerate into a liquid rivulet prior to competing spinodal instabilities. Building off of this, shapes were patterned with built in perturbations to drive assembly[2,55,70–72]. It was shown that perturbations can be patterned as stable or unstable, where stable modes do not grow, whereas unstable modes are amplified and lead to breakup. Further, it was observed that patterning at wavelengths longer than the fastest growing mode can produce secondary particles and require added energy input to initiate breakup.

Additional research attempting to comprehend the instabilities related to a rectangular strip were conducted[35,61]. Hartnett et al.[61] focused on the previously mentioned competition between collapse to a single particle and breakup into multiple particles. Here, a critical length in which a rectangular solid will form a single particle compared to multiple particles was determined. This relationship was rationalized as a competition between axial retraction of the two ends of the rectangle and the Rayleigh Plateau instability driving a breakup, and a time scale was determined that could predict the dominant mechanism. From a continuum viewpoint[35], the breakup behavior of a thin Ni strip was modeled, and found good agreement with experimental results.

Finally, a second component was added to the patterned dewetting process[54,55]. Fowlkes et al.[55], introduced the second component by a two-step lithography process which created triangles of dissimilar metals in contact with each other. Here, half-half particles of Cu-Ni were successfully created. Wu et al.[73] used patterned disks and a two-step, single component, deposition process to create a complex distribution of primary and secondary particles. This process was also used with two components (Cu-Ni) to further the complexity of the particle distribution. The results from this work are shown in Figure 20.

Optical Properties

Isolated Particles

There has been significant research on the plasmonic properties of isolated metallic nanoparticles via optical techniques as well as EELS, though due to the relative ease of sample preparation, testing, and cost, optical techniques tend to dominate the literature[74,75]. These nanoparticles are fabricated by self-assembly methods such as dewetting[76,77], and more controlled techniques such as chemical synthesis[78–80], and lithography[81,82]. Here, various shapes and materials have been

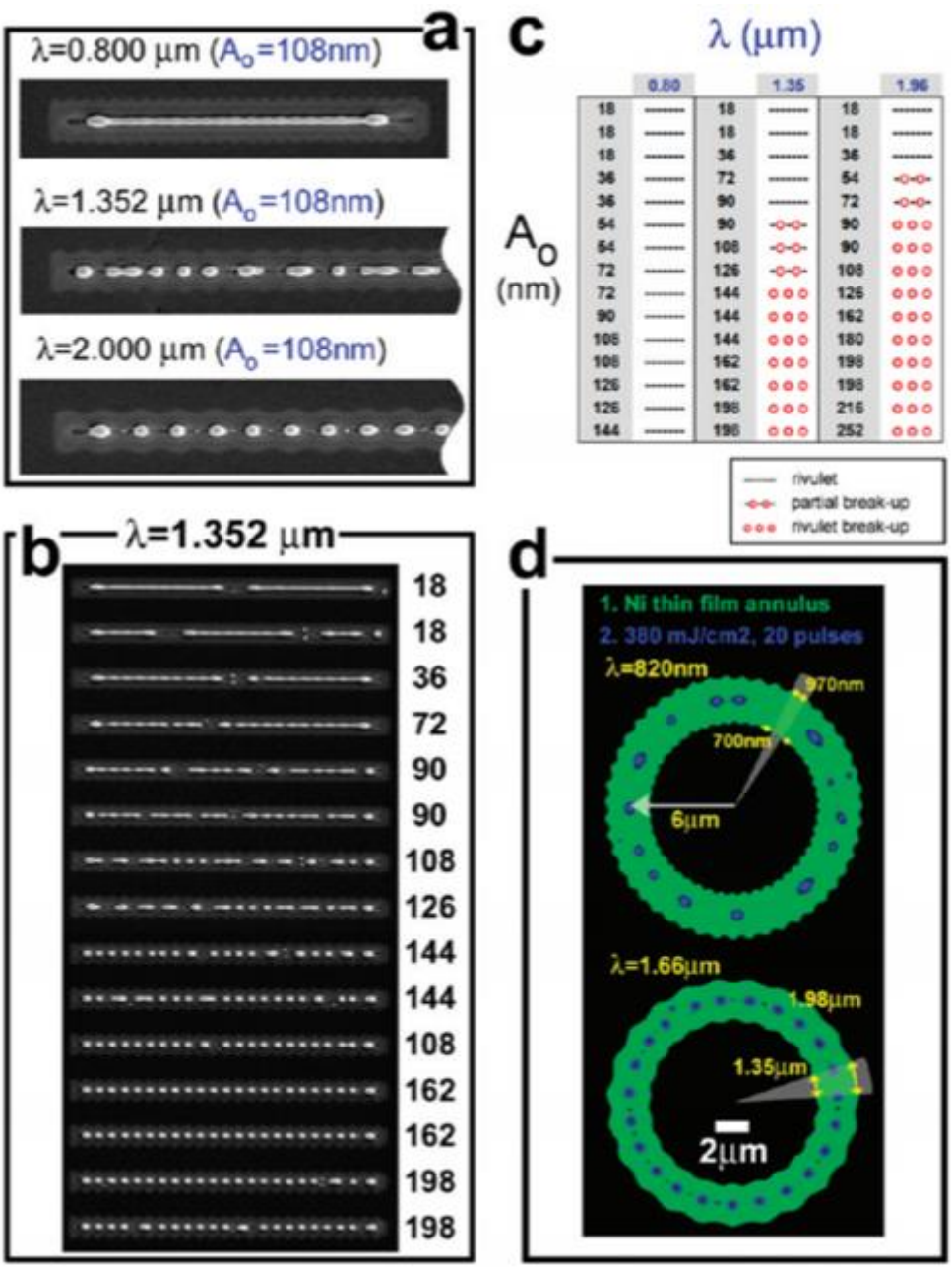

Figure 19: Example of unperturbed rectangles and rings, as well as rectangles and rings with various wavelength perturbations[72]

studied; however, the most common material used is Au. The majority of this research has been focused on controlling the LSPR resonance through the shape of the nanostructures. Additionally, the addition of a capping dielectric material has been investigated. Singh et al[83] investigated the influence of a TiO_2 layer around Au nanoparticles. They demonstrate the expected blue shifting of LSPR resonance with decreasing nanoparticle size, and also discuss the size dependance on the photodegradation of the nanoparticles. Another work concerned with Au on a quartz substrate[84] investigated not only the influence of nanoparticle size on the LSPR resonance energy, but also on the behavior of the peaks associated with interband transitions. They found that the intensity and sharpness of these peaks increased with decreasing particle size. A study of a more complex structure, a rod, demonstrates the same blue shifting behavior with increased rod length[85]. Here, they demonstrate the influence of the chemical synthesis parameters on the quality of the structures, and thus the LSPR peaks. The aspect ratio of the structures is specifically mentioned as a way in which to control the sharpness of the LSPR peaks.

EELS of Isolated Particles

Although the less common technique, EELS represents a more powerful method to determine the optical properties of nanostructures. EELS allows for the observation of individual nanoparticles, with incredibly high special resolution. Further, EELS provides the opportunity to probe specific positions on a structure to better characterize individual modes. Finally, optically dark modes can be measured in EELS. As was the case with optical excitation techniques, the spherical nanoparticle has been studied in EELS[19,86,87]. A study on the behavior of Au_xAg_{1-x} solid solution nanoparticles[20] demonstrates that nanoparticles of small enough size (~50 nm for Au) will exhibit a single resonance at the quasiplanar mode. This mode is the high energy limit for LSPR modes, and is a combination of higher order modes. Increasing the size of the nanoparticles reveals dipole

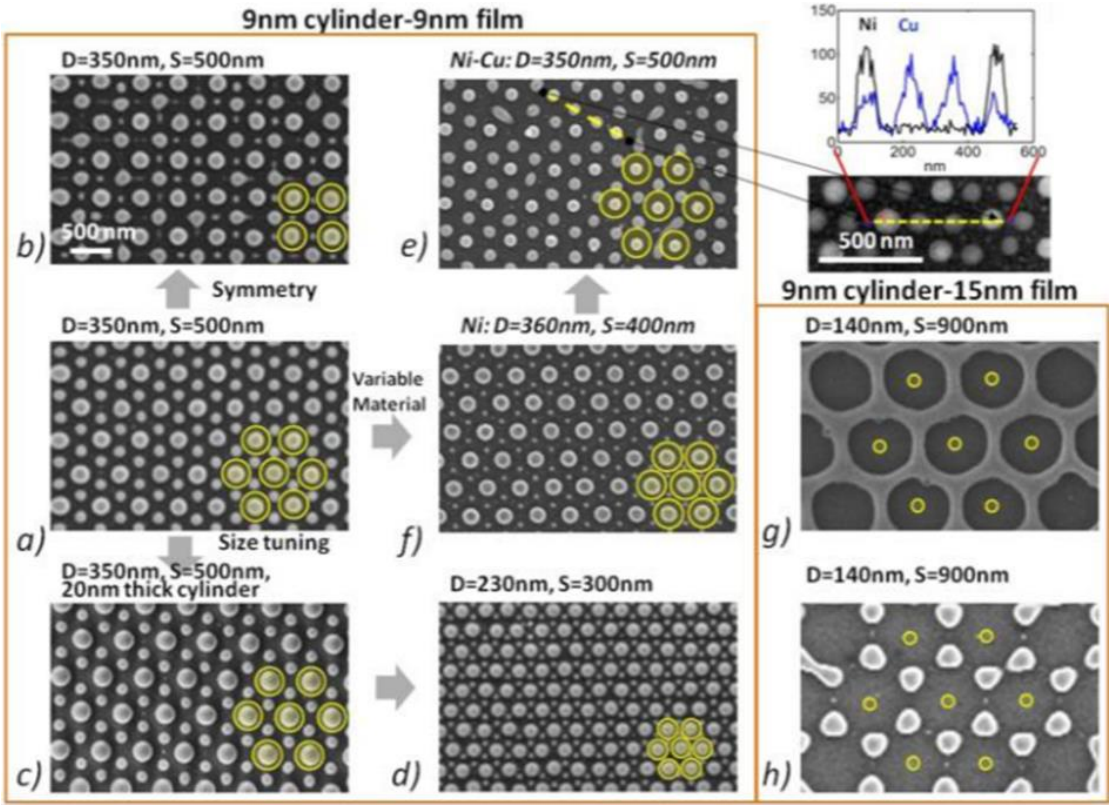

Figure 20: Highly ordered array of nanoparticles from a two step deposition method[73]

and quadrupole modes that are shifted based off of the relative content of Au and Ag. While a spherical nanoparticle will exhibit multiple LSPR peaks in EELS, depending on the size, the symmetry of the shape does not fully utilize the capabilities of EELS to map mode specific signatures: uniform spherical nanoparticles will demonstrate a uniform intensity all around the nanoparticle for each LSPR mode.

Increasing the geometric complexity of the nanostructures to a rod for example, unlocks the unique capabilities of EELS. Figure 21 (theory), as well as Figure 22 and Figure 23 (experimental) demonstrate the mapping potential of EELS spectrum imaging theoretically[88] and experimentally[89]. The EELS intensity near the ends of the rods are bright for all LSPR modes; however, the intensity at this location decreases with the number of nodes. For higher order modes, such as the m = 2 mode it is more efficient to excite at the center position, whereas for the m = 3 the intensity is at a maximum at the 1/3 and 2/3 locations along the rod. As the polarization order increases, the intensity of excitation is reduced, and at ~3.5 eV (for Ag) there is an approximately equal intensity around the structure, this corresponds to the quasiplanar mode. Rods of extremely high aspect ratio[90], due to lengths up to 10 μm, have also been measured in EELS. The resonance of the LSPR modes, up to greater than m = 6, are included in Figure 24. Beyond the rod, structures such as a triangular[91] (Figure 25) have been measured and analyzed through a combination of modeling and experiments. In this particular study, various modes are distinguished up to the bulk resonance. The slight increase in nanostructure complexity has a significant influence on the LSPR modes. Here, the first mode is bright at each corner of the triangle instead of the two edges in a rod structure.

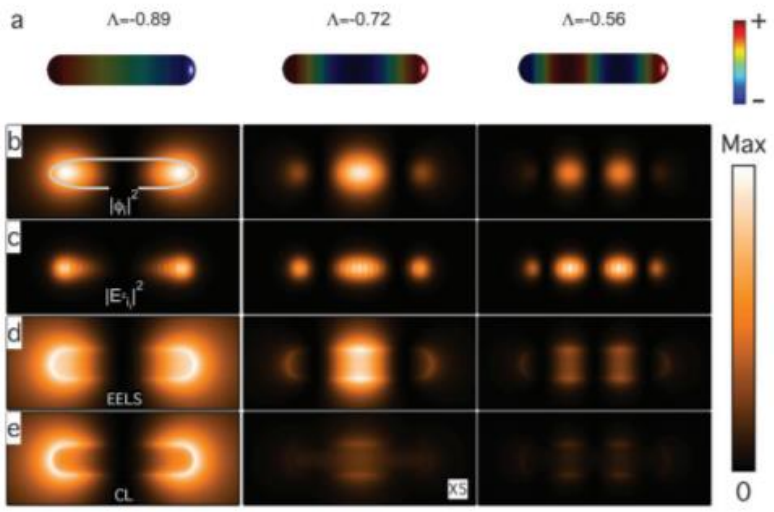

Figure 21: Modelled EELS behavior of different localized surface plasmon modes in a rod[88]

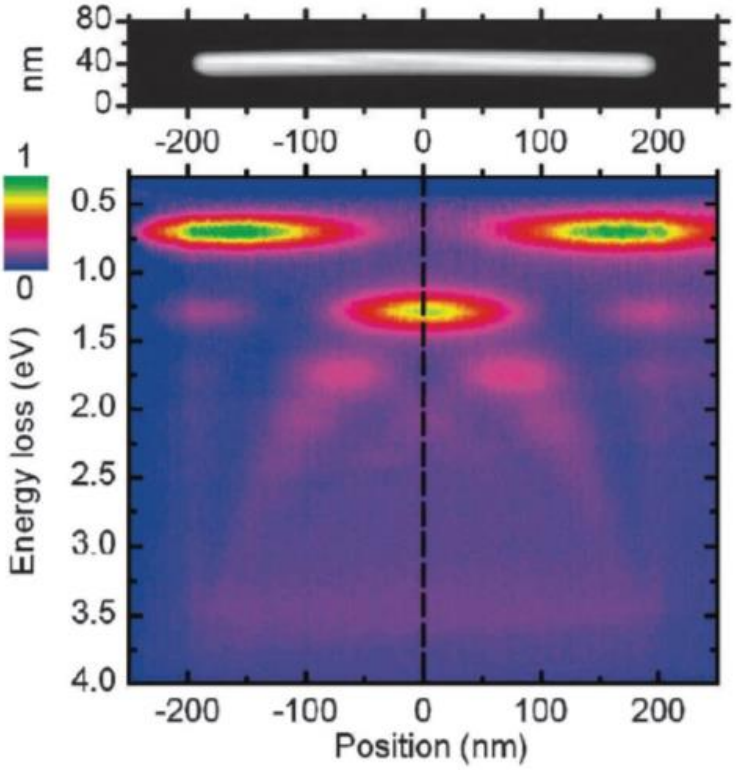

Figure 22: Experimental EELS localized surface plasmon modes in a rod structure[89].

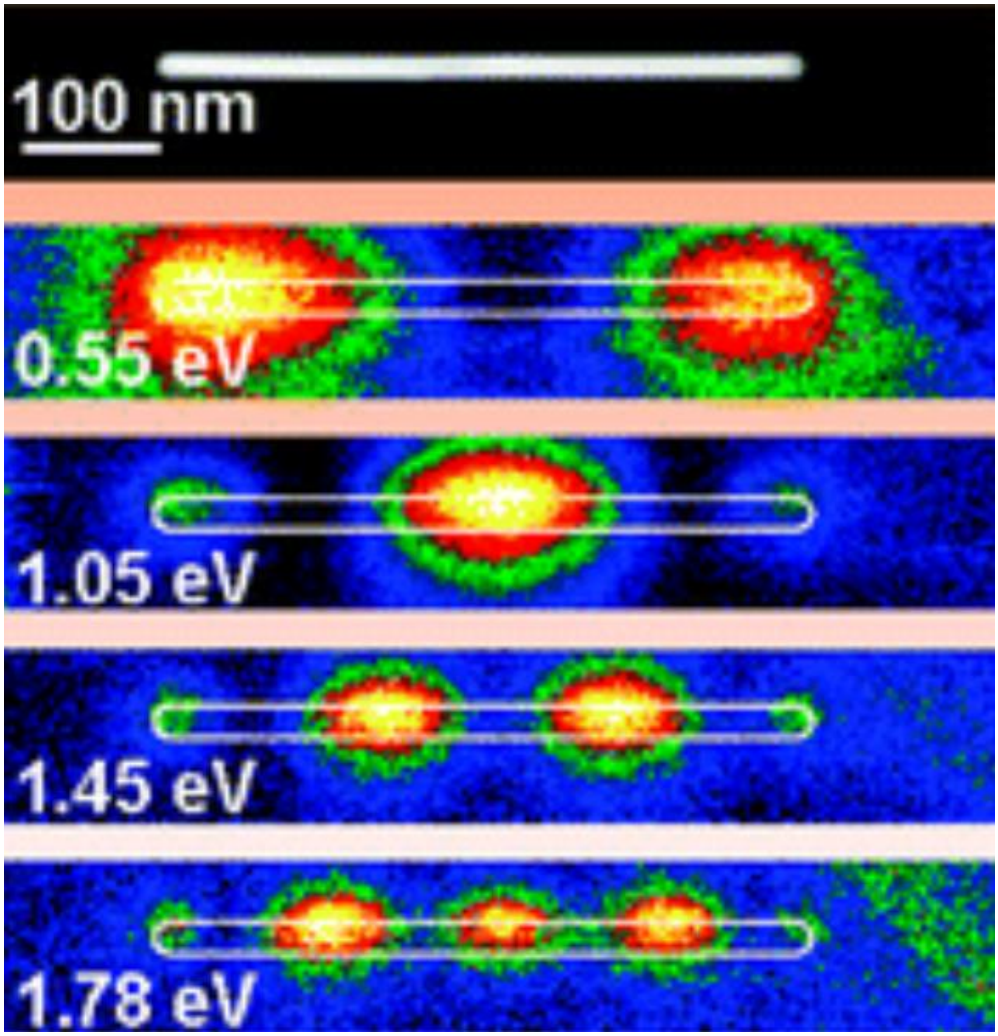

Figure 23: Experimental spectrum images demonstrating the modes of a long rod in EELS[89].

Split Ring Resonators

Another nanostructure that has been the subject of significant research is the split ring resonator (SRR). The split ring resonator, as can be seen in Figure 26, is a U-shaped structure. An interesting feature of the split ring resonator is that its geometry allows for an end-to-end dipole mode generating a partially circulating current. Optical studies on both coupled and individual SRR arrays have conducted extensively, in which subjects such as substrate effects[92], gap size[93], and asymmetry[94] have been investigated. SRR structures have also been measured in EELS by Von Cube[95,96]. Here, they also consider the behavior of inverted structures. Figure 27 shows the ability to tune the various modes in the SRR through the characteristic dimensions. It can be seen that the first mode, which possesses the magnetic dipole, could not be raised beyond ~1.2 eV.

Substrate Effects in EELS

In a study by Kadkhodazadeh et al.[97], the influence of the substrate on the plasmonic response was investigated. Here, they compare a SiO_2, SiN_x, and Si substrate to the vacuum condition. The work is predominately theoretical with basic experiments to provide a degree of validation. It was found that the resonance of the LSPR mode can be dramatically altered by the substrate. A red shift from the vacuum condition, associated with the dielectric properties, was maximized with Si and minimized with SiO_2. Further, the reduction of the substrate thickness was demonstrated as a method to shift modes to higher energies. They also demonstrate the variation in the spectra as a function of impact parameter (distance of probe position from the metal), where there is the expected drop in intensity as this value increases.

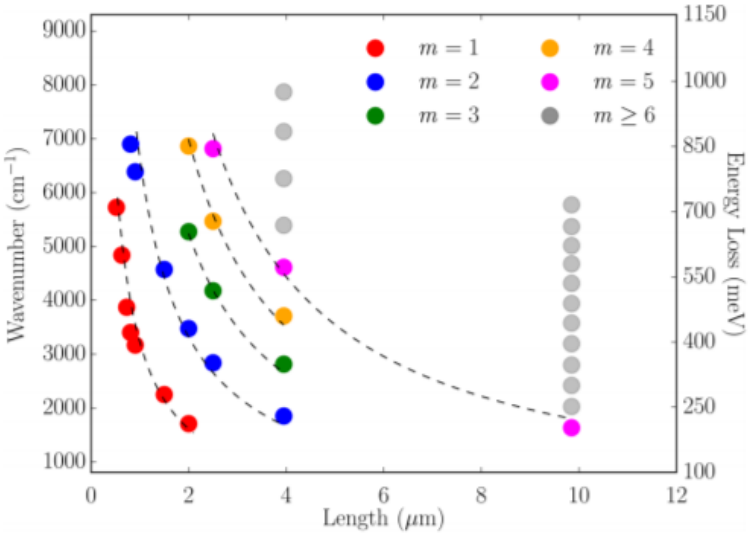

Figure 24 Resonance energy of very high aspect ratio rods[90].

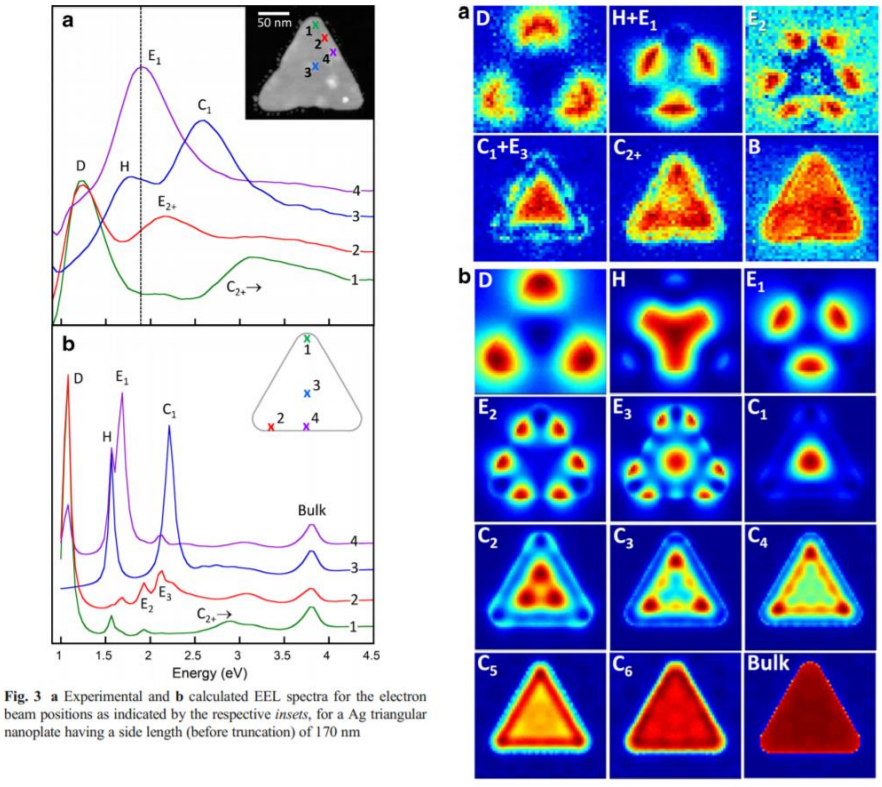

Fig. 3 **a** Experimental and **b** calculated EEL spectra for the electron beam positions as indicated by the respective *insets*, for a Ag triangular nanoplate having a side length (before truncation) of 170 nm

Figure 25: The plasmonic modes observed in a triangular structure[91].

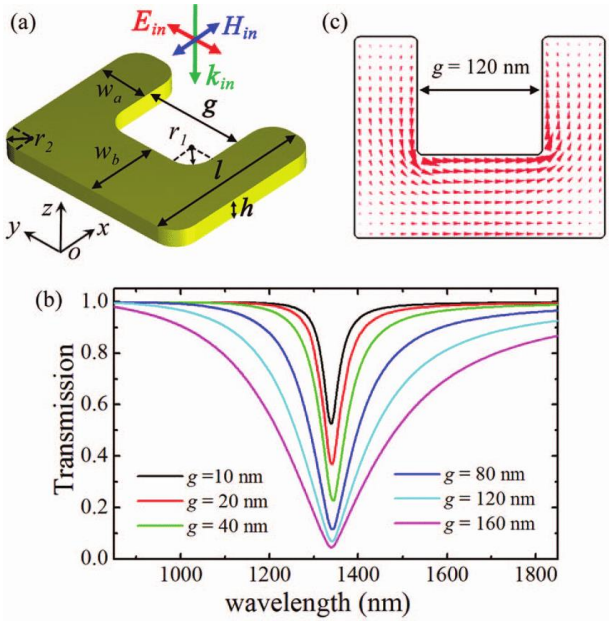

Figure 26: Split ring resonator geometry[93]

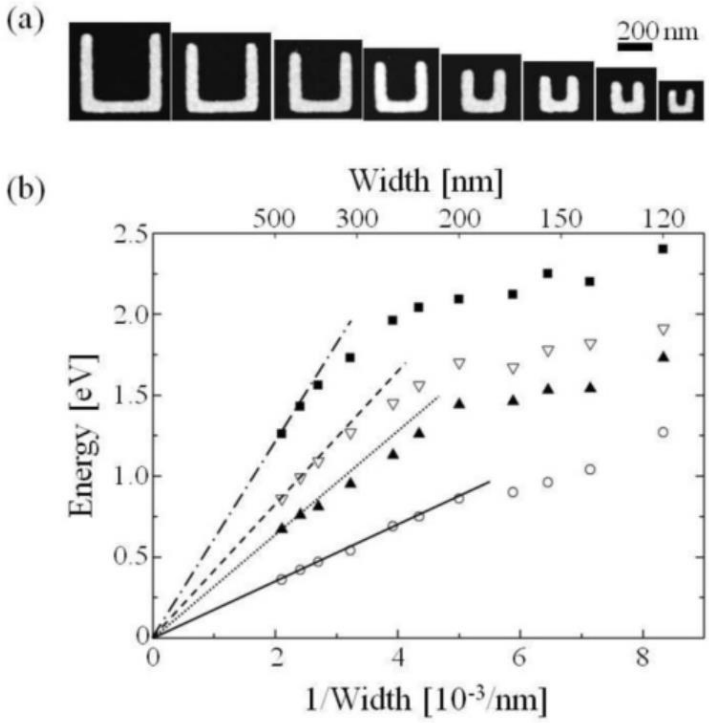

Figure 27: Resonance energy of the SRR modes with size. The open circles represent the first mode[95]

Coupled Structures

Another source of added complexity that can be used to augment the functionality of a plasmonic material is placing individual nanoparticles in close enough proximity to encourage coupling. This coupling creates a hybridization of the individual structures. The most basic coupled system is the dimer, in which the metaatom is comprised of two individual structures. Au spherical nanoparticles with a varying gap size[98] demonstrated a single peak that shifted from the single rod resonance to lower energy as a function of decreasing gap size via optical measurements. In a dimer structure only the lower energy bonding mode is observable, due to the net electric field of the LSPR mode, and thus it can be deduced that the higher energy dark mode is exhibiting the opposite behavior, and thus enhancing the mode splitting. Observing this structure in EELS, as was done in[97,99] reveals the optically dark mode, and verifies that increasing the gap size decreases the splitting between the two modes. The response from optical excitation can be observed within an EELS setup by introducing an optical source to create stimulated electron energy gain and loss spectroscopy. This was demonstrated on a dimer structure by Collette, et al.[8].

Beyond the dimer, higher order coupled structures have also been investigated in EELS. One study[100] considered coupled ring structures consisting of individual Au rods in which various influences such as number of rods (or "mers") in the system from a trimer to a hexamer, gap size, and rod length were characterized. Figure 28 shows these the coupled LSPR modes for these structures. The generation of these coupled structures in closed ring structures have been studied by other groups due to the circulating current that can achieved in modes where all individual rods align head to tail[22]. As was discussed previously, this circulating current generates a magnetic field. These coupled structures can be advantageous for creating higher energy resonance modes compared to connected magnetic structures such as the SRR, due to lithographic limitations. The

lengths of the individual cut rod structures can be nearly as large as the entire SRR and provide a similar resonance energy.

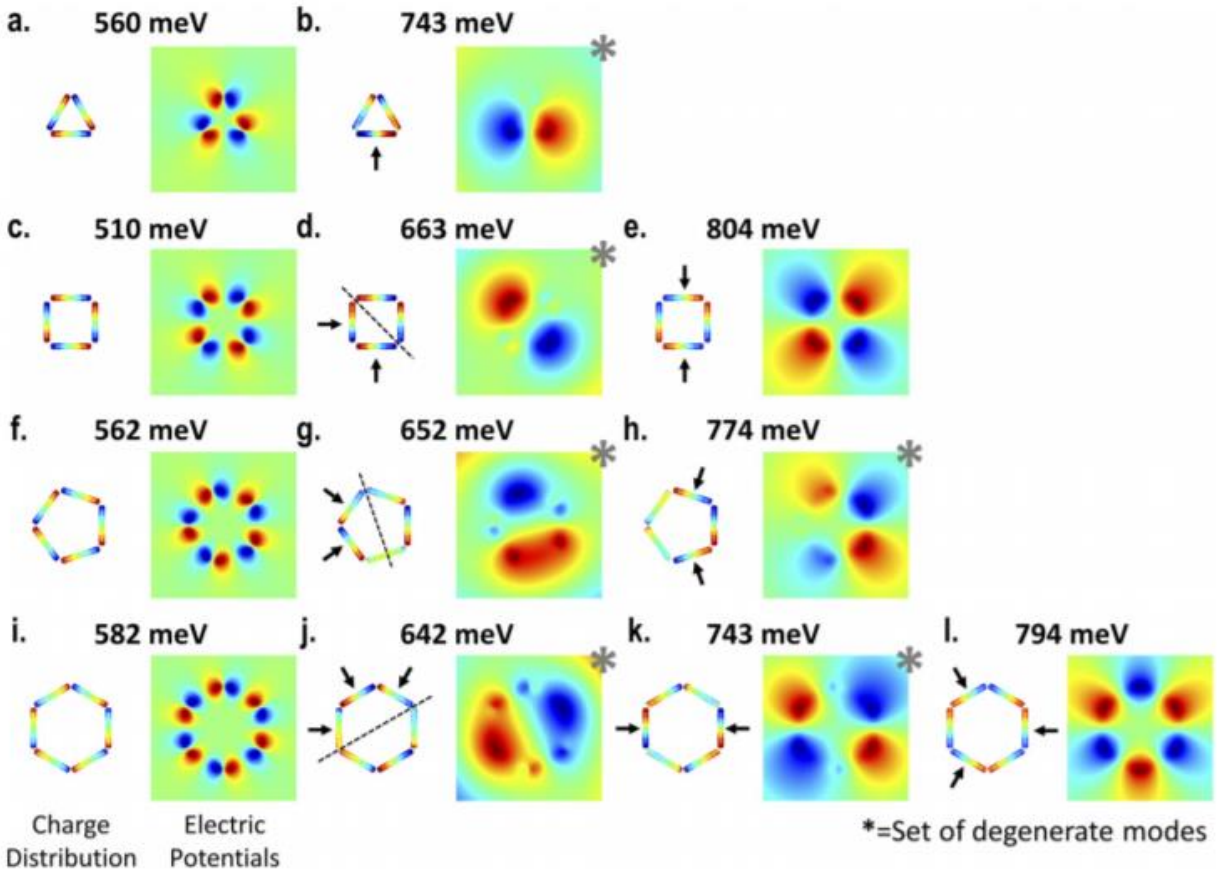

Figure 28: Modelled excitation modes in ring structures with increasing number of members[100]

CHAPTER I
SIMULTANEOUS DECOMPOSITION AND DEWETTING OF NANOSCALE ALLOYS: COMPARISON OF EXPERIMENT AND THEORY

Published in Langmuir (2021)

Simultaneous Decomposition and Dewetting of Nanoscale Alloys: Comparison of Experiment and Theory

Javier A. Diez[1], Alejandro G. Gonzalez[1], David A. Garfinkel[2], Philip Rack[2], Joseph McKeown[3], and Lou Kondic[4]

1. Instituto de F´ısica Arroyo Seco, Universidad Nacional del Centro de la Provincia de Buenos Aires, and CIFICEN-CONICET-CICPBA, Pinto 399, 7000, Tandil, Argentina

2. Department of Materials Science & Engineering, University of Tennessee, Knoxville, TN 37996, USA and Center for Nanophase Materials Science, Oak Ridge National Laboratory, Oak Ridge, TN 37831

3. Materials Science Division, Lawrence Livermore National Laboratory, Livermore, CA 94550, USA

4. Department of Mathematical Sciences, New Jersey Institute of Technology, Newark, NJ 07102, USA

Authors Contribution

The author's contributions were focused on the experimental aspect of the bi-metallic dewetting process. In addition to synthesis of the $Ag_{40}Ni_{60}$ thin films, the author was responsible for performing pulsed laser induced dewetting (PLiD) on the thin films. The samples were then characterized by scanning electron microscope (SEM) and energy-dispersive x-ray spectroscopy (EDX) to determine chemical segregation time scales compared to dewetting. Dynamic transmission electron microscopy (DTEM) was conducted at Lawrence Livermore National Laboratory, by Joseph McKeown; however, data analysis, interpretation, and the generation of figures was conducted by the author. Finally, the author was responsible for generating a finite element thermal model to approximate the timescales for liquid lifetime in both the DTEM and bulk experiments. The author was responsible for generating the text for the experimental portions of the paper. The theoretical aspect of the paper was conducted by collaborators, Javier Diez, Alejandro Gonzalez, and Lou Kondic. The majority of the text discussing the theory has been removed from this dissertation, as it does not directly pertain to work done by the author, though

the figures are included. The abstract, introduction, and conclusions have not been altered from the original text, and thus include discussion of the theory portion of the paper to provide insights on the motivation and direction of the collaborative research.

Abstract

We consider the coupled process of phase separation and dewetting of metal alloys of nanoscale thickness deposited on solid substrates. The experiments involve applying nanosecond laser pulses that melt the $Ag_{40}Ni_{60}$ alloy films in two setups: either on thin supporting membranes, or on bulk substrates. These two setups allow for extracting both temporal and spatial scales on which the considered processes occur. The theoretical model involves a longwave version of Cahn-Hilliard formulation used to describe spinodal decomposition, coupled with asymptotically consistent longwave based description of dewetting that occurs due to destabilizing interaction between the alloy and the substrate, modeled using the disjoining pressure approach. Careful modeling, combined with linear stability analysis and fully nonlinear simulations, leads to results consistent with the experiments. In particular, we find that the two instability mechanisms occur concurrently, with the phase separation occurring faster and on shorter temporal scales. The modeling results show strong influence of the temperature dependence of relevant material properties, implying that such dependence is crucial for the understanding of the experimental findings. The agreement between theory and experiment suggests the utility of the proposed theoretical approach in helping to develop further experiments directed towards formation of metallic alloy nanoparticles of desired properties.

Introduction

Metal thin films of nanoscale thickness deposited on solid substrates and exposed to laser pulses melt and dewet into nanoparticle arrays, which find application in a number of different fields including solar cells, plasmonics, sensing and detection, among others, see[101,102] for recent reviews. In addition to the basic scientific interest, understanding these interface driven instabilities is further motivated by their potential to drive various self– and directed–assembly mechanisms[103,104]. During the past decade experimental techniques have improved significantly, which lay the foundation for new theoretical insights into the dynamics of pure metals and also bilayer films[14,105,106]. However, there has been very limited experimental work on immiscible systems going through phase separation while being unstable with respect to dewetting type of instability, see[104] and references therein. Such systems are of particular interest since they allow for multi–functional properties, associated with the multiple phases that emerge in the nanoparticle, to be realized[49,107–110]. From the theory point of view, the considered systems are challenging since they involve two coupled instability mechanisms operating in parallel. In addition, the presence of a substrate clearly influences the dewetting process, and may also play a role in phase separation. Although models describing unstable multicomponent systems are available (e.g., Cahn-Hilliard formulation[111]), further work is needed to formulate a tractable formulation, in particular when the domain of interest (the film itself) is evolving as well. We note that a film geometry (film between two substrates) was considered in[112,113] including discussion of the boundary conditions between film and the substrate. Phase separation was coupled to fluid dynamics in model-H, see[114,115] for reviews. To describe coupling of dewetting and decomposition, model-H needs to be completed by boundary conditions; such a model was studied without dewetting but including the substrate and consideration of films with free surface[116–118]. Then, model-H was simplified in longwave approximation, considering also the coupling between decomposition and dewetting instability[119,120]. We are, however, not aware of any previous work

applying these models to describe and model instabilities of films of nanoscale thickness in the context of a specific experiment.

This paper is organized as follows. First we discuss two types of pulsed laser induced dewetting (PLiD) experiments that provide complementary information about free surface and chemical phase–separation instabilities in the $Ag_{40}Ni_{60}$ system, where a liquid phase miscibility gap exists below 2800 K: (i) experiments on thin supporting membranes that provide time–resolved information about free surface instability, as well as for long–time analysis of the chemical composition of the resulting nanoparticles, while (ii) experiments carried out on bulk silicon provide simultaneous information about both free surface and chemical instabilities, albeit with lower temporal resolution. Then, we discuss the theoretical model that we have further developed and adapted. As we will see, direct connection between experiments and theory is insightful, since the experimental results immediately justify the choice of material parameters in the model. We then proceed to discuss the results of linear stability analysis as well as of fully nonlinear time dependent simulations that provide additional insight into the physical mechanisms governing the instabilities.

Experimental Methods

Two different substrates were used in our experiments: 1) a thin 15 nm SiNx membrane supported at the perimeter with 200 μm thick Si, and 2) 100 nm thermally grown SiO2 on 500 μm Si ”bulk” samples. $Ag_{40}Ni_{60}$ thin films were grown on both substrates via radio frequency magnetron co-sputtering from individual Ag and Ni targets powered with 40 and 70 W, respectively. The as-deposited film forms as a supersaturated nanocrystalline solid solution,[23] and is liquefied using nanosecond laser pulses[121]. The first set of experiments is carried out on the thin membranes[122,123]. The experiments use DTEM (dynamic transmission electron microscope) that offers the unique

ability to resolve small scale morphological changes on the nanosecond timescale *during* in situ photothermal heating. Thus, this technique allows for the direct determination of the metal liquid thin film free surface evolution. DTEM utilizes two pulsed lasers: one directed to the cathode to photoexcite an electron beamlet and a second directed at the substrate to photothermally heat the sample. The two laser sources are synchronized such that the imaging electrons arrive at various "delay" times relative to the heating pulse, and thus provide snapshots of the evolving system with nanosecond temporal resolution. For these experiments, the average laser fluence was (38 ± 1.5) mJ/cm^2, using a 1064 nm wavelength and 12 ns (full-width of the laser beam at $1/e^2$ of the maximum fluence) Gaussian laser profile, and 20 ns square wave electron beamlet with a 75 ns electron beamlet interpulse delay time (blue double arrow in Figure 29 The metal temperature after a single laser pulse computed using finite element method (FEM) for a stationary 10 nm $Ag_{40}Ni_{60}$ film on the 15 nm SiNx membrane is shown as well. FEM simulations, including discussion of the parameters entering the simulations were described previously[121] (see also SI, Section 1 for more details). The FEM result suggests that the temperature exceeds both the Ag (1234 K) and Ni (1728 K) melting temperatures, and thus the film fully liquefies; furthermore, the high temperature Ni melts ~ 7 ns after the laser pulse peaks. Subsequently, the liquid state is maintained for long times (> 1 μs) (such long times are not included in Figure 29). Figure 29 also shows the DTEM delay time (green double arrow), defined as the difference between the center of the imaging electron beamlet and the simulated time at which the film temperature reaches the Ni melting temperature. The latter time is for simplicity used as origin for the time axes. We note that since the electron beamlet used for imaging has a 20 ns pulse width, the information (about the laser pulse pulse) ± 10 ns from the times denoted contributes to the results.

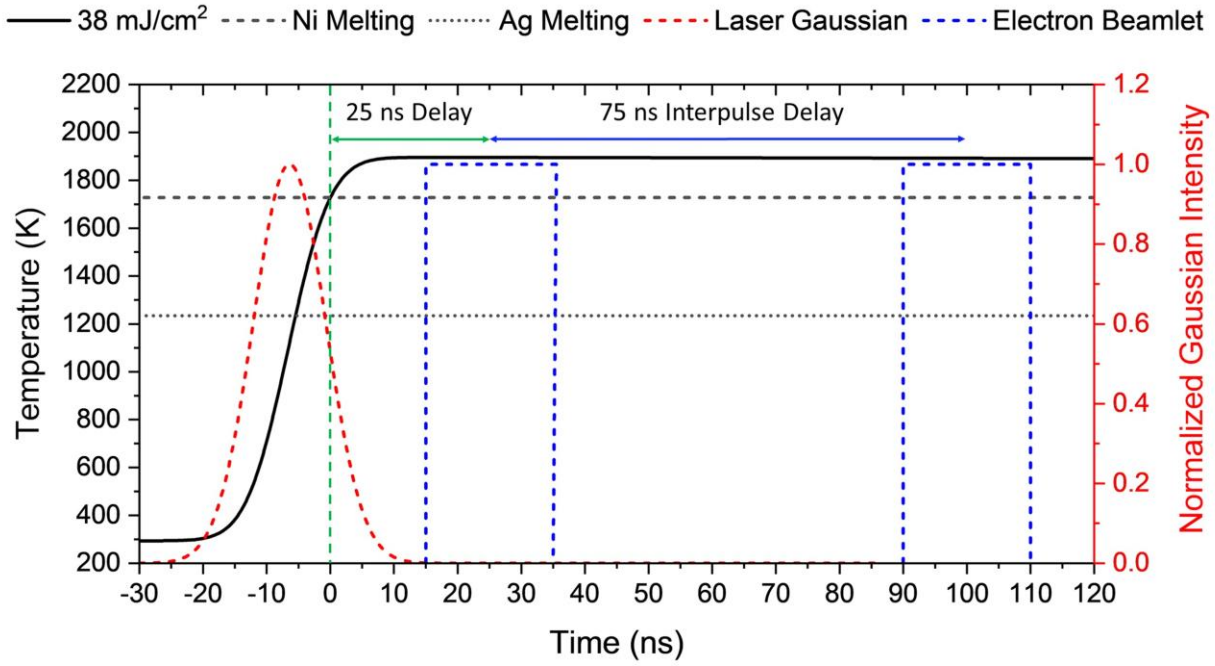

Figure 29: FEM (finite element method) based temperature simulation of Ag40Ni60 thin film DTEM experiment illustrating imaging at 25 ns and 100 ns liquid lifetime. The red dashed curve is the normalized laser intensity, the solid black curve is the temperature profile of the Ag40Ni60 assuming a 38 mJ/cm2 laser fluence, and the blue dashed square waves denote the electron beamlets. See Supplementary Information (SI), Section 1, for more details regarding FEM simulations.

The second experimental setup considers metal films on a bulk substrate, which is a much better heat sink, and thus requires higher laser fluence, and yields significantly faster cooling rates. Thus a 248 nm KrF laser with a 20 ns Gaussian pulse width and a laser fluence of 170 mJ/cm^2 was used to perform PLiD on the bulk samples. The rapid cooling allows for subtle changes associated with the brief high–temperature liquid lifetime to be frozen into the microstructure, and then characterized ex-situ (Figure 32 later in the text includes the example of simulation results).

Experimental Results

Before presenting the experimental results, it is instructive to first review the general dewetting dynamics that are observed in metallic thin films. A thin solid metal film, while not in its lowest energy state due to is high surface area to volume ratio, is typically stable at room temperature (on experimental time scales) since the requisite diffusive material transport is slow. When pulsed with a laser at a fluence sufficient to melt the film, the liquid film can dewett via spinodal dewetting or by nucleation of holes.[3] After a hole formation, the rim surrounding the hole expands, coalescing into a network of rivulets. These rivulets subsequently destabilize via Rayleigh-Plateau type of instability into drops that solidify into truncated nanoparticles sitting on the substrate with wetting angles with the substrate governed by the balance of liquid metal-substrate-vacuum interface energies. In this work we are interested in elucidating how these fluid instabilities and consequent material transport are affected via the simultaneous phase separation of an immiscible alloy. To accomplish this we perform in situ DTEM experiments to determine the dewetting time scale and then compare results on bulk substrates where we can observe the resultant competition between the free surface instabilities and the phase separation. The sequence of images shown in Figure 30 is generated through the combination of four separate (PLiD/DTEM) experiments, with each experiment denoted by a specific color in the border of the images where two cathode pulses are generated for each experiment with an interpulse delay time of 75 ns (note the blue double arrow in Figure 29). Figure 30 shows DTEM results demonstrating a progression from a 10 nm $Ag_{40}Ni_{60}$

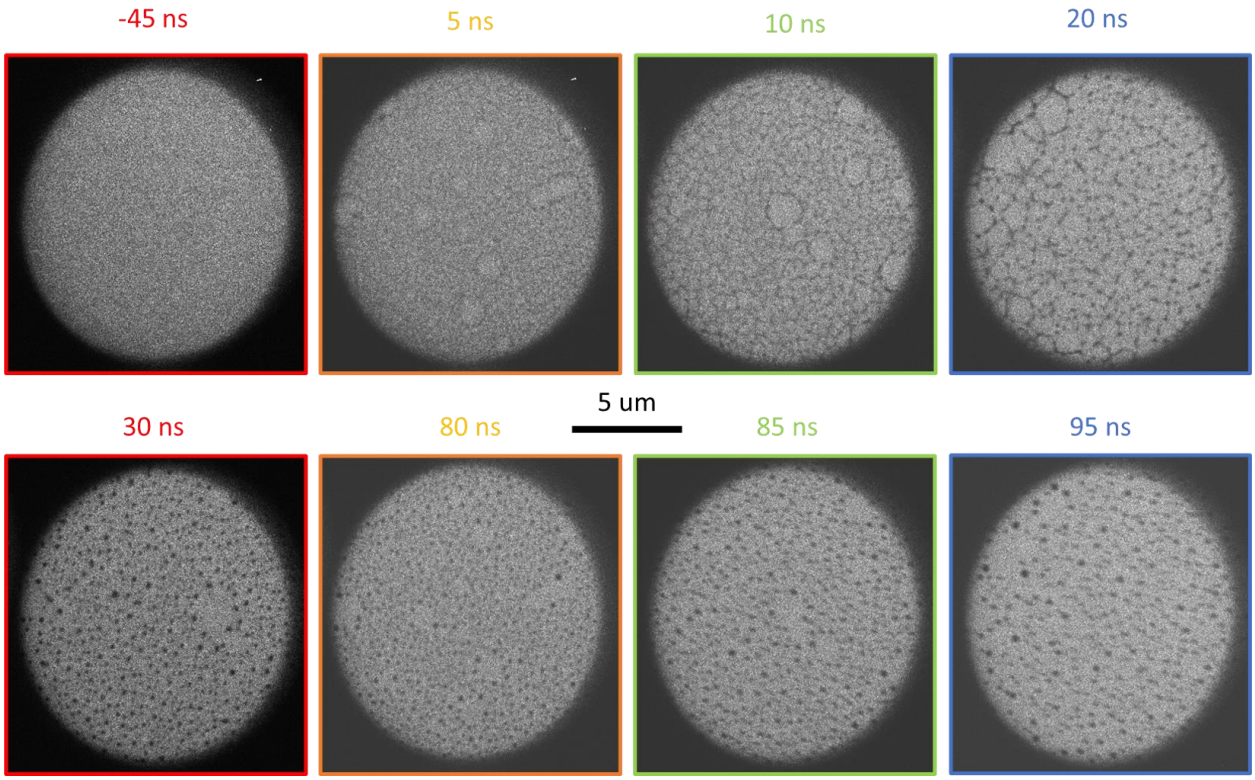

Figure 30: DTEM images of Ag40Ni60 thin film dewetting progression as a compilation of four separate experiments (denoted by image border color. The time is measured relative to the onset of Ni melting. The length of the horizontal black line corresponds to 5 µm.

thin film deposited on a thin Si_3N_4 membrane to an array of nanoparticles formed via PLiD. Changes to the sample morphology are observed after 5 ns, in the form of isolated hole formation. The film then progresses to partial breakup into rivulets at 20 ns, and nanoparticles by 30 ns. These results are consistent with previous DTEM experiments.[24] We also note similarity of the emerging patterns to the ones observed during dewetting of polymer films[124–126], although the latter occur on very different timescales due to significantly larger viscosities[104].

Beyond film breakup, we also observe phase separation in the resultant nanoparticles. Figure 31 illustrates a high angle annular dark field (HAADF) image and energy dispersive x-ray spectroscopy maps of the combined Ag and Ni concentrations from the dewetted film.

The HAADF images are generated from electrons scattered at high angles so that they have both thickness and atomic number contrast. Thus, the larger particles appear brighter and for areas that are not saturated, the Ag is brighter than Ni. Several nanoparticle morphologies emerge, including bimetallic Janus nanoparticles, and for larger particles we find Ni regions decorating the Ag core particles.

The competition between dewetting and phase separation was observed through PLiD experiments on a bulk substrate (Figure 32, Figure 33, and Figure 34, where cooling times are much more rapid. Note that a higher fluence and slightly longer pulsewidth is used for the bulk substrate experiments. Figure 32 demonstrates a PLiD progression from one to five pulses for three different initial film thickness: (a) 10, (b) 20, and (c) 30 nm. Each image was taken near isolated hole formations, indicating the film is in the initial stages of dewetting. Whereas dewetting was sufficiently slow in the thicker films (20 and 30 nm) to capture holes in the laser center, the 10 nm film produced fully formed nanoparticles in the laser center after one pulse. Thus, for the 10 nm film, images were taken just outside the laser hot spot to observe this same stage of dewetting. Also shown in Figure 32d) are FEM simulations which indicate the rapid cooling associated with the 20 ns Gaussian laser pulse width. The liquid lifetime for the 10 nm Ag40Ni60 film determined through FEM simulations is ≈ 20 ns, which is consistent with the ≈ 30 ns evolution time determined in

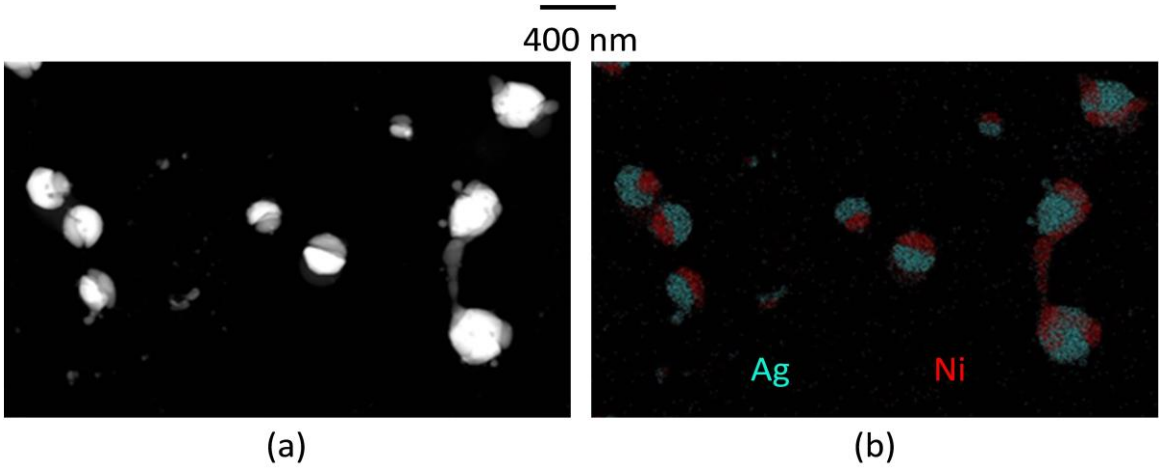

Figure 31: (a) High angle annular dark field (HAADF) scanning transmission electron image of AgNi nanoparticles, and (b) Energy dispersive x-ray spectroscopy (EDS) image of (a) illustrating the chemical morphology of the resultant nanoparticles (where red denotes Ni and light blue denotes silver). Note that the results are long time configurations, obtained after solidification which occurs on the microsecond time scale.

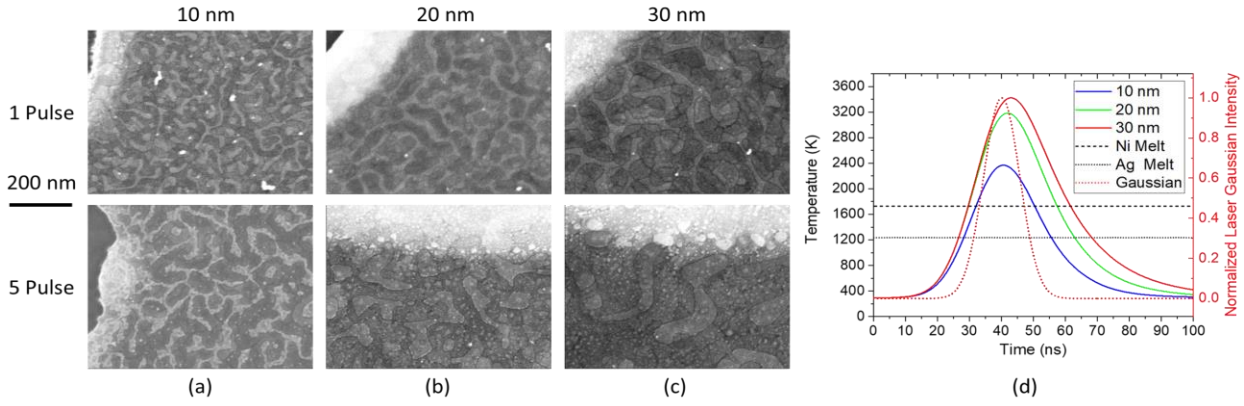

Figure 32: (a-c) Images of phase separation for films of thickness 10, 20, and 30 nm; (d) FEM simulations for a single pulse for 10, 20, and 30 nm thick films. Note that the red dashed line is the normalized laser intensity (left axis) and the two horizontal dashed and dotted lines are the Ni and Ag melting temperatures, respectively.

Figure 30. Figure 32 demonstrates that there are obvious signs of phase separation for all film thicknesses after one laser pulse, as seen by the contrast in the film neighboring the holes. Here, Ag develops as the darker matrix of the microstructure, and the Ni as the brighter islands. Further validation of chemical segregation, discussed below, indicates that phase separation starts developing prior to spinodal dewetting, and that there is a coarsening observed for longer times (multiple laser pulses). The Ni lamella width in the 10 nm thick film is on the order of 9.2±1.9 nm (24.7±3.4 nm center-to-center spacing) and 15.8±3.6 (42.0±7.4 nm) for a 1 pulse and 5 pulse sample, respectively. The corresponding results for thicker films.

To verify the origin of the contrast occurring within the metal film, chemical analysis, via EDS (energy dispersive x-ray spectroscopy), was performed. Figure 33a) shows an SEM (scanning eletron miscroscopy) image with an overlaid green arrow denoting the region where an EDS linescan was measured. Figure 33b) illustrates the Ag and Ni composition along the green line shown in Figure 33a). The Ag and Ni concentrations fluctuate in a manner consistent with the contrast seen in the SEM image. To further validate that the contrast observed in Figure 32a-c) can be attributed to chemical segregation, Figure 33d) shows a two–dimensional map of Ag and Ni in the box selected in Figure 33c). Once again there is a correlation between chemical segregation, as demonstrated by the green (Ag) and red (Ni) regions in Figure 33d), and the contrast observed in Figure 33c).

The length scale of dewetting for a 10 nm film was determined by nearest neighbor analysis of dewetted particles, as seen in Figure 34. The images were processed using the ImageJ software. The contrast was optimized and the image was thresholded to generate a pure black and white image. Subsequently the average spacing was determined using the ImageJ nearest neighbor plugin (NND) which generates a list of nearest neighbor spacings for each particle. Figure 34a) is a SEM image of the dewetted film and b) shows a nearest neighbor distribution. Small areas of the part (a) of the image were selected (c and e), where the image is processed (d and f) and analyzed to

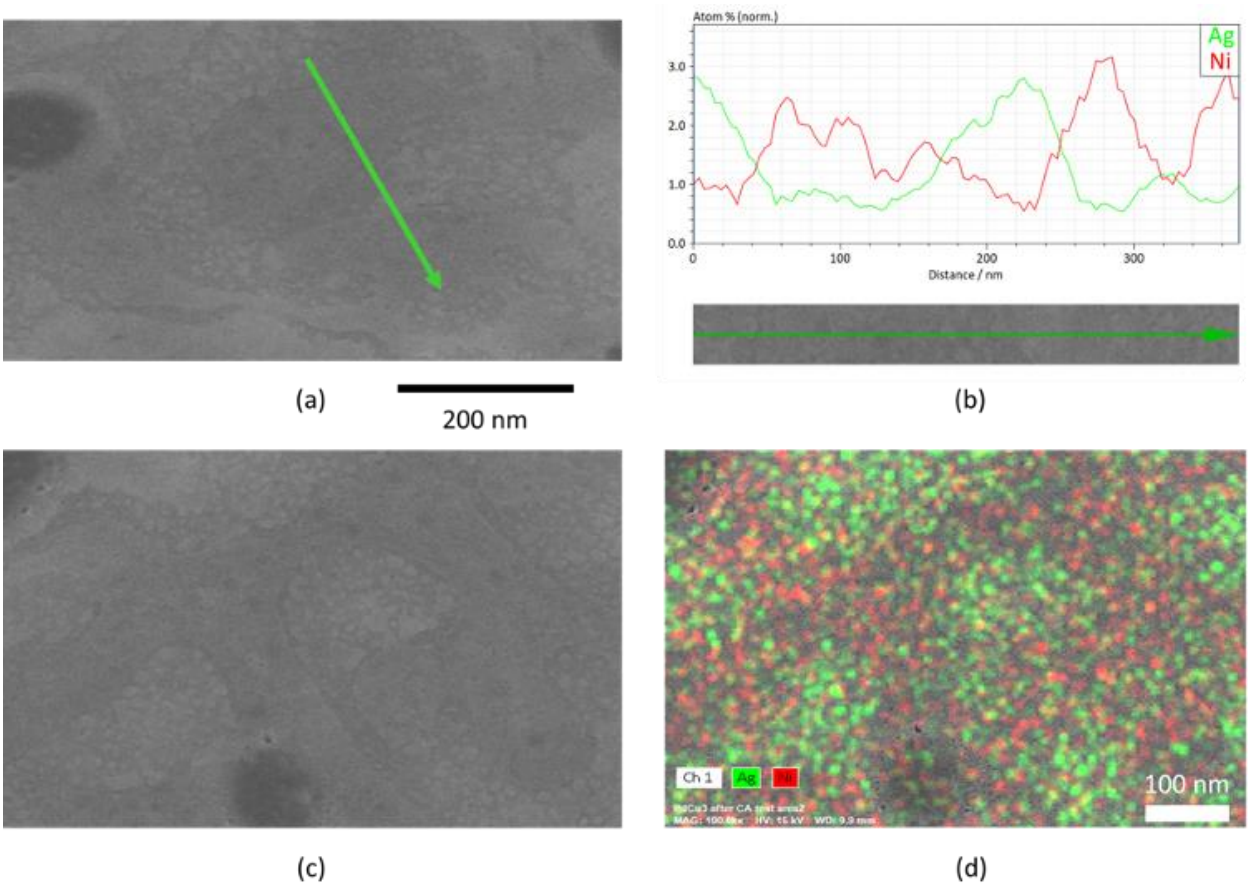

Figure 33: a) SEM image of 30 nm thick AgNi film following 20 pulses, b) EDS line scan associated with (a), c) SEM image of 30 nm AgNi film following 20 pulses, d) EDS map of Ag (green) and Ni (red) associated with (c). Note that the parts (a) and (c) show different regions of the film.

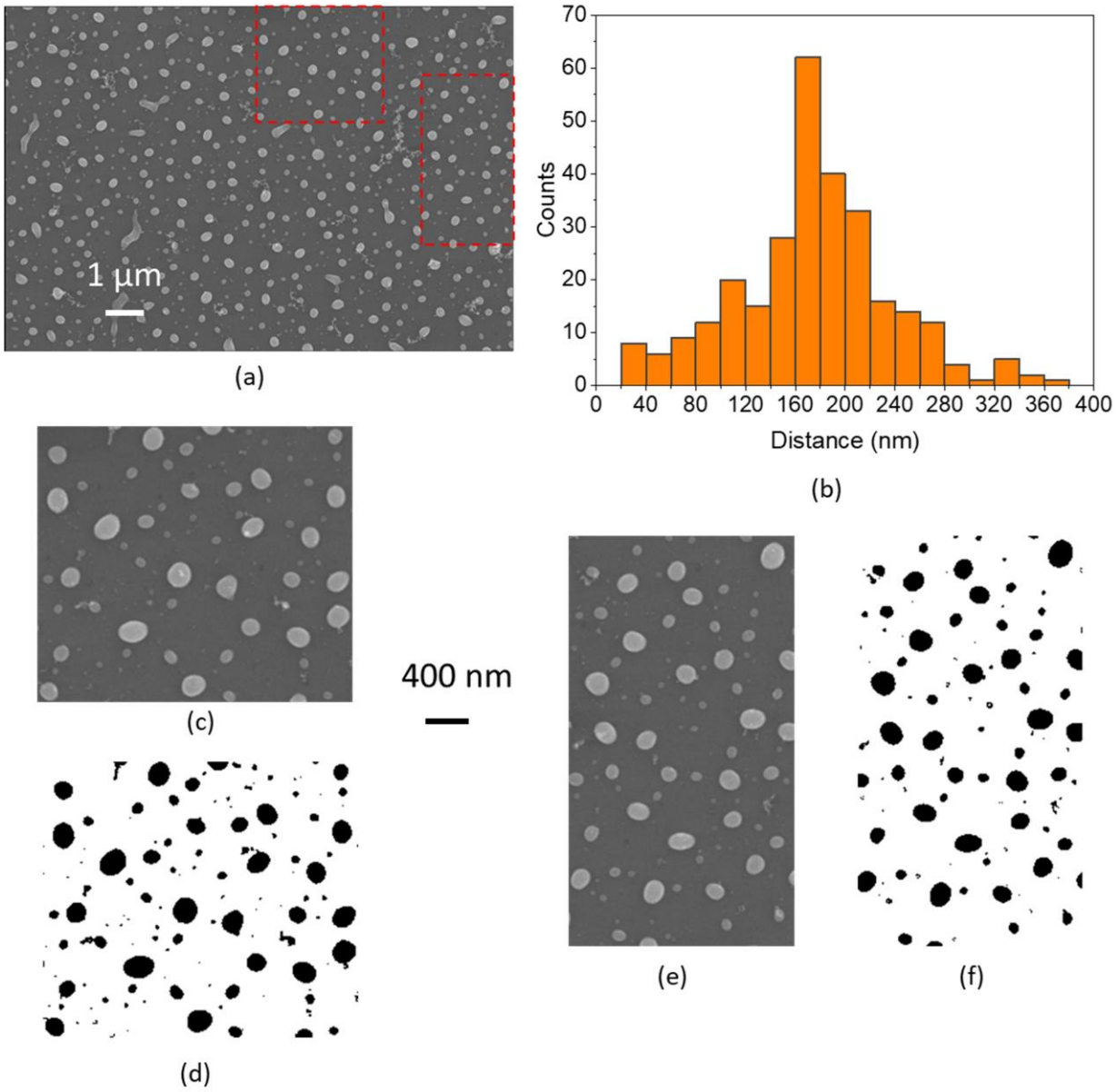

Figure 34: a) SEM image of laser hot spot for 10 nm sample after one pulse, b) distribution of measured particle spacing from (a), c-f) examples of raw and processed selections from (a) for particle analysis.

determine the nearest neighbor distribution. The peak of this normal distribution (160-180 nm) is consistent with the average spacing (175 nm) determined from this distribution.

Conclusions

Two experimental setups, considering thin alloy films evolving either on thin supporting membranes or on bulk substrates, have allowed us to obtain simultaneous information about two instability mechanisms: breakup of liquid alloy films into drops, and a chemical instability, involving phase separation of constitutive metals. These results have guided further development of the theoretical model based on the longwave Cahn-Hilliard formulation governing phase separation, asymptotically consistent model describing free surface evolution, and utilizing disjoining pressure describing destabilizing forces driving film breakup. The model that we have presented may be considered as a first step in developing a more complete approach that would include a number of aspects that have not been considered in detail (or not at all) in the present work. These include in particular coupling of the present model with self-consistent computations of the temporally and spatially dependent temperature field, as well as including the fact that the metal/substrate interaction forces, modeled by the disjoining pressure formulation, may depend on alloy composition.

Despite the implemented simplifications, we have shown that the current model can be used to accurately describe the experimental results. The model therefore provides a basic setup to help devise novel experimental setups directing the coupled free surface and phase separation instabilities to produce particles of desired properties. We hope that the presented work will encourage further research that will provide even more precise information about the liquid phase evolution of immiscible alloy films toward bimetallic functional nanoparticle assemblies.

Acknowledgments

We acknowledge support by NSF Grants CBET-1603780 (DAG and PDR) and CBET1604351 and DMS-1815613 (LK). All the authors acknowledge that the scanning electron microscopy was

conducted at the Center for Nanophase Materials Sciences, which is a DOE Office of Science User Facility. JAD and AGG acknowledge support from Consejo Nacional de Investigaciones Cient´ıficas y T´ecnicas (CONICET, Argentina) and Agencia Nacional de Promocio´n Cient´ıfica y Tecnolo´gica (ANPCyT, Argentina) with grant PICT 1067/2016.

Appendix 1: Collaboration Theory Figures

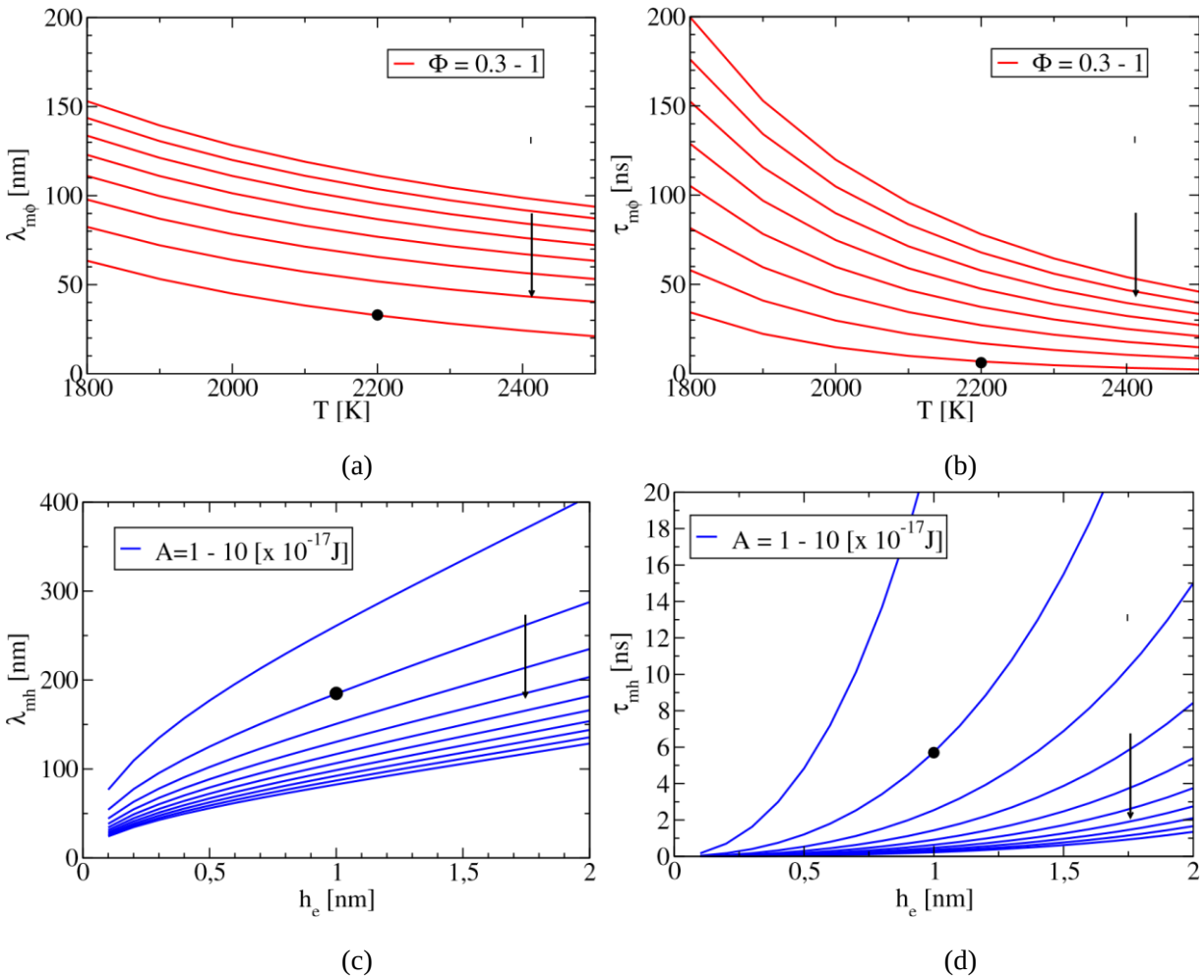

Figure 35: (a) Characteristic length and (b) characteristic time of the concentration instability as a function of temperature T for given values of the Girifalco–Goods coefficient, Φ. The arrow shows the direction of Φ increase. (c) Characteristic length and (d) characteristic time of the thickness instability as a function of he for parametrically specified values of the Hamaker constant A. The arrow shows the direction of A increase. In all cases, the black points indicate the chosen values for the simulations: (a) $\lambda_{m,\varphi}$ = 33 nm, (b) $\tau_{m,\varphi}$ = 6.1 ns, (c) $\lambda_{m,h}$ = 185 nm, (d) $\tau_{m,h}$ = 5.7 ns. $\lambda_{m,h} = 2\pi/k_{m,h}$ and time $\tau_{m,h} = 1/\omega_{m,h}$ as a function of h_e for given values of A. Figure 7(c) and (d)) and the experimental observations shown in Fig. 6 lead to the choice h_e = 1 nm and A = 2 × 10^{-17} J (black points in Fig. 7(c) and (d)). We point out that the choice of appropriate value for h_e is also governed by practical considerations: the simulations that will be discussed in what follows are difficult to carry out for very small values of h_e, for this reason we chose h_e = 1 nm, although the realistic value may be smaller, see Ref.[42]

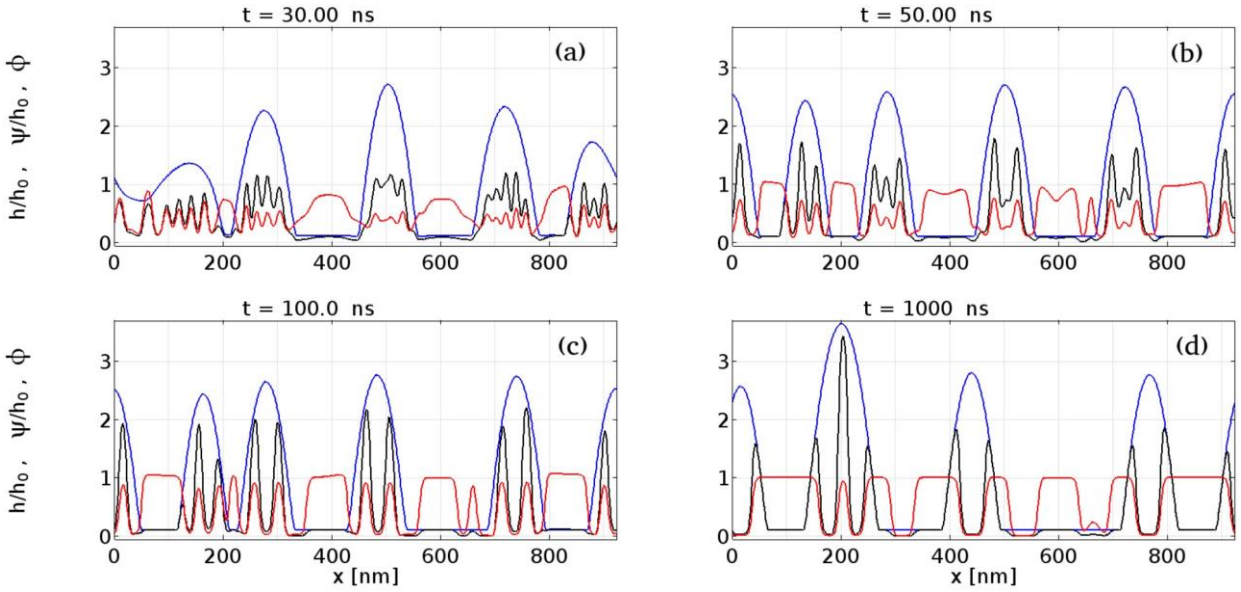

Figure 36: Time evolution of h/h_0 (blue), ψ/h_0 (black) and $\varphi = \psi/h$ (red) for a film of thickness $h_0 = 10$ nm and Ag–concentration $\varphi_0 = 0.4$ in a domain $L = 5\lambda_{m,h} = 956.2$ nm: (a) t = 30 ns, (b) t = 50 ns, (c) t = 100 ns, (d) t = 1000 ns. See SI, movie-2D for animations.

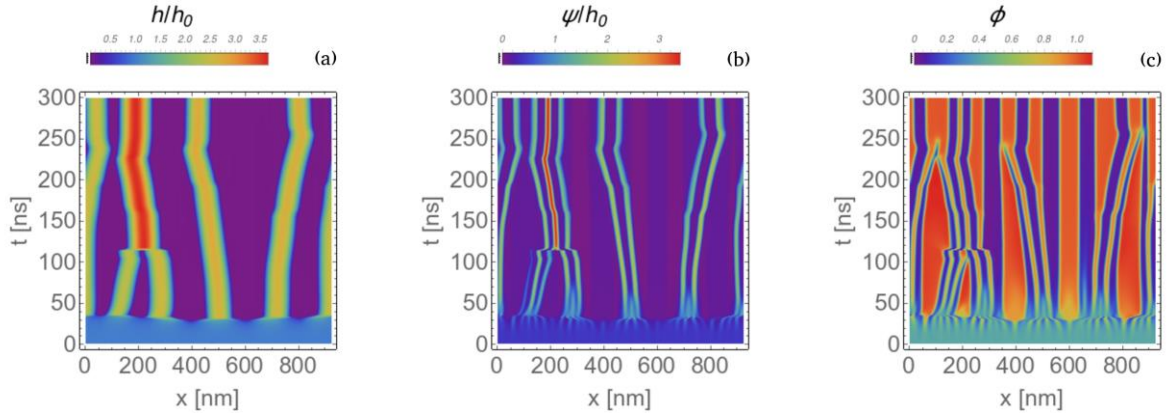

Figure 37: Space-time plots showing evolution of the patterns from Fig. 8 (for early times). As in Fig. 8, φ corresponds to Ag concentration. The kinks that are visible around times $\sim 220 - 230$ ns are discussed in the text, see also SI movie-2D for animations.

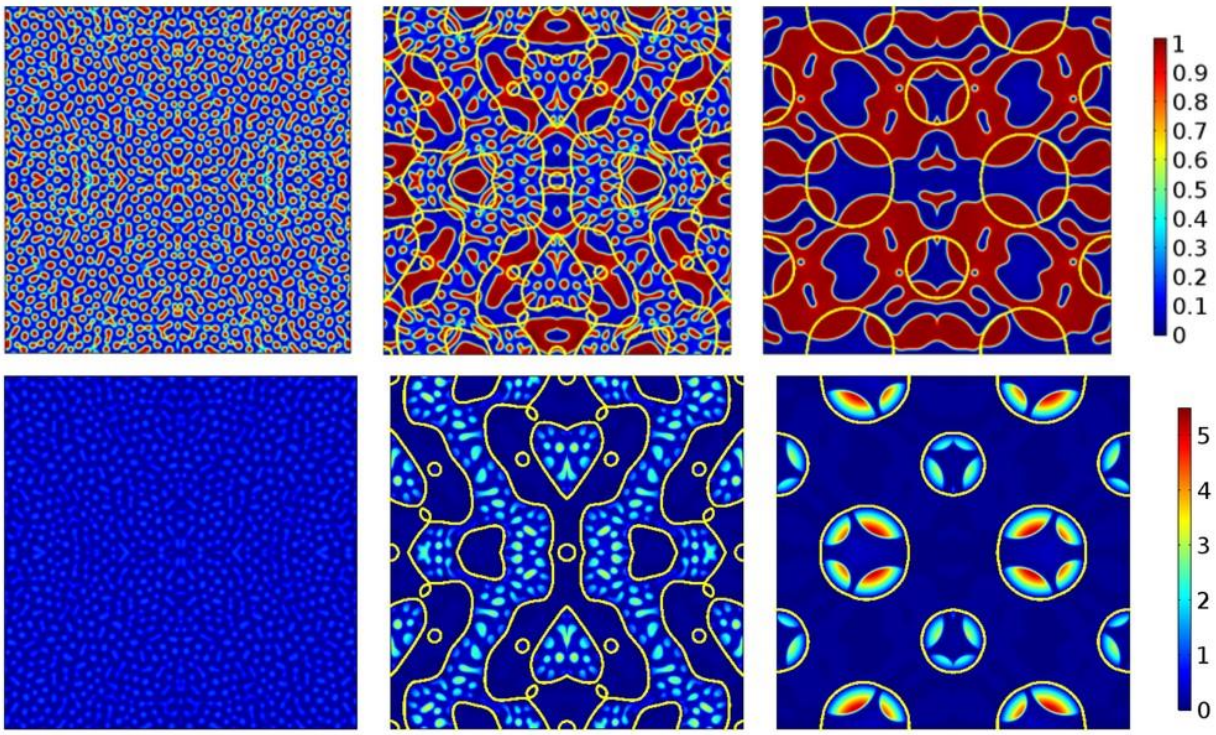

Figure 38: Evolution of (top) φ = ψ/h and (bottom) ψ/h0 (h0 = 10 nm and φ0 = 0.4) for (left to right) t = 40, 80 and 700 ns. The yellow solid curves show the drop border (level line for h = 1.5he). The linear dimension is 6λm,h, twice as large as the actual computational domain size. See SI, movie-3D-phi and movie-3D-psi for animations.

CHAPTER II
OPTICAL AND MAGNETIC PROPERTIES OF AG-NI BIMETALLIC NANOPARTICLES ASSEMBLED VIA PULSED LASER INDUCED DEWETTING

Published in ACS Omega (2020)

Optical and Magnetic Properties of Ag-Ni Bimetallic Nanoparticles Assembled via Pulsed Laser Induced Dewetting

David A. Garfinkel[1], Grace Pakeltis[1], Nan Tang[1], Ilia N. Ivanov[2], Jason D. Fowlkes[1,2], Dustin A. Gilbert[1], Philip D. Rack[1,2,*]

1. Department of Materials Science and Engineering, University of Tennessee, Knoxville, Tennessee 37996, United States

2. Center for Nanophase Materials Sciences, Oak Ridge National Laboratory, Oak Ridge, Tennessee 37831, United States

Authors Contribution

The author of this dissertation was the lead writer and experimentalist on this paper. Fabrication of the bi-metallic thin films as well as pulsed laser induced dewetting (PLiD) was conducted by him. The author is responsible for all scanning electron microscopy (SEM), bright field transmission electron microscopy (TEM), and optical transmission spectroscopy results. Collaborators Nan Tang and Dustin Gilbert provided vibrating sample magnetometry measurements, while Grace Pakeltis provided scanning transmission electron microscope and electron energy loss spectroscopy results. The author performed all data analysis, interpretation, writing, and figure generation for the results included in this paper.

Abstract

Pulsed laser induced dewetting (PLiD) of $Ag_{0.5}Ni_{0.5}$ thin films results in phase separated bimetallic nanoparticles with size distributions that depend on the initial thin film thickness. Co-sputtering of Ag and Ni is used to generate the as-deposited nanogranular supersaturated thin films. The magnetic and optical properties of the as-deposited thin films and PLiD nanoparticles are characterized using a vibrating scanning magnetometer (VSM), optical absorption spectroscopy, and electron energy loss spectroscopy (EELS). Magnetic measurements demonstrate that $Ag_{0.5}Ni_{0.5}$ nanoparticles are ferromagnetic at room temperature when the nanoparticle diameters

are > 20 nm, and superparamagnetic < 20 nm. Optical measurements show that all nanoparticle size distributions possess a local surface plasmon resonance (LSPR) peak that red-shifts with increasing diameter. Following PLiD, a Janus nanoparticle morphology is observed in the scanning transmission electron microscope (STEM) and low-loss electron energy loss spectroscopy (EELS) reveals size-dependent Ag and Ni LSPR dipole modes, while higher order modes appear only in the Ag hemisphere. PLiD of Ag-Ni thin films is shown to be a viable technique to generate bimetallic nanoparticles with both magnetic and plasmonic functionality.

Introduction

Nanoparticles possessing magneto-plasmonic bi-functionality have recently emerged as an innovative tool in biomedicine. Magnetic nanoparticles can be used to guide drug delivery, provide contrast in magnetic imaging, and generate heat via an alternating magnetic field[127,128], while plasmonic particles are used for optical imaging, sensing, and drug delivery[129]. These two properties can be combined for specific applications utilizing bi-functional magneto-plasmonic nanoparticles, including magnetic resonance imaging[130], magnetic hyperthermia therapy[131], and detection of tumor cells[132,133].

Chemical growth techniques[127] are most commonly utilized for fabricating magneto-plasmonic nanoparticles; however, another highly robust technique exists: pulsed laser induced dewetting (PLiD)[14,16–18]. PLiD exploits the inherent metastability of a metallic thin film on a substrate. Rapid heating of the thin film (typically less than 20 nm thick), via a nanosecond pulsed laser, generates a random array of spherical caps with a wetting angle dependent on substrate/film interactions. An added degree of control can be achieved by lithographically patterning the metal thin film prior to dewetting in order to design the size, spacing, and location of these nanoparticles[1,2,33,35,72]. In lieu of lithography, the initial metal film thickness can be used to influence the resultant nanoparticle

size as thicker films yield a distribution with larger particles. While PLiD nanoparticles are typically exploited on substrates, it is envisaged that free nanoparticles can be released from the substrate via a post-etching or release process.

Nanoparticles exhibiting both plasmonic and magnetic properties have primarily been achieved using a noble metal, Au[127,128,131,133] or Ag[134,135], and $Fe_{3-x}O_4$[127,128,131,133–135] or Co[135], respectively. While much research has been conducted on single component metal dewetting, a few studies have explored multi-component dewetting[45,47,110,123,136,137]. In a multi-component system, atomic interactions between dissimilar atoms create chemical instabilities that can compete or synergize with the dynamics observed in single component dewetting. While these interactions add complexity to the nanoparticle self-assembly dynamics, the enhanced functionality, such as bi-functional magneto-plasmonic nanoparticles, has stimulated several groups to explore PLiD of both miscible[55] and immiscible[123,138] bi-metallic systems. The overarching goal is to understand the simultaneous hydrodynamic and chemical energy landscape to create intricate nanoparticle morphologies.

The binary material system investigated here, Ag-Ni, offers significant potential for magneto-plasmonic nanoparticles via PLiD for three primary reasons. First, the individual elemental properties are compelling, with Ag exhibiting strong plasmonic properties, and Ni being a high-moment ferromagnet. Second, both Ag and Ni are biocompatible, allowing their integration into medical treatments. Finally, the thermodynamic mixing behavior of Ag and Ni is interesting in that the alloy has very limited solid solubility with a liquid miscibility gap. Immiscibility across a large temperature range is expected to facilitate the emergence of complex particle morphologies during the liquid phase dewetting process. Depending on initial film geometry, substrate, and laser heating conditions, various particle architectures can be achieved, including Janus, core-shell,

homogenously dispersed fine grains, and variations thereof[139].Through an improved understanding of multi-component dewetting, the size and chemical morphology can be tuned to generate specific magnetic and plasmonic properties.

Here we sputter various thickness Ag0.5Ni0.5 thin films and expose them to 20 ns laser pulses to induce liquid state dewetting of the films. We correlate the nanoparticle size distribution of the resultant nanoparticles to the as-deposited film thickness. We then compare the magnetic properties and optical properties of the as-deposited thin films and the PLiD nanoparticle arrays. Finally, low-loss EEL spectra for individual Ag-Ni Janus nanoparticles are measured and the full plasmonic spectra are elucidated as a function of nanoparticle size.

Results and Discussion

Dewetting

As has been shown previously[121], the as-deposited co-sputtered Ag0.5Ni0.5 films are a nanogranular mixture of supersaturated Ag-rich and Ni-rich grains. The size distribution of the nanoparticles derived from PLiD for five initial film thicknesses is shown in Figure 39. Due to differing resolution requirements, the nanoparticles resulting from the initial film thicknesses of 20 and 10 nm were analyzed with a scanning electron microscope (SEM) on bulk substrates, while the 5, 3 and 2 nm samples required transmission electron microscopy (TEM), and thus were prepared on suspended membranes. As Figure 39f illustrates, and as has been demonstrated in numerous materials, controlling the initial film thickness is a convenient tool to control the nanoparticle size, where thinner films produce smaller particles. Except for the 20 nm thick sample, the resultant PLiD nanoparticles exhibit a clear bimodal size distribution.

The hydrodynamic evolution of liquid thin films has been studied in detail, and is initiated by instabilities such as spinodal and homogeneous and heterogenous nucleation[14,28,41,122,140,141].

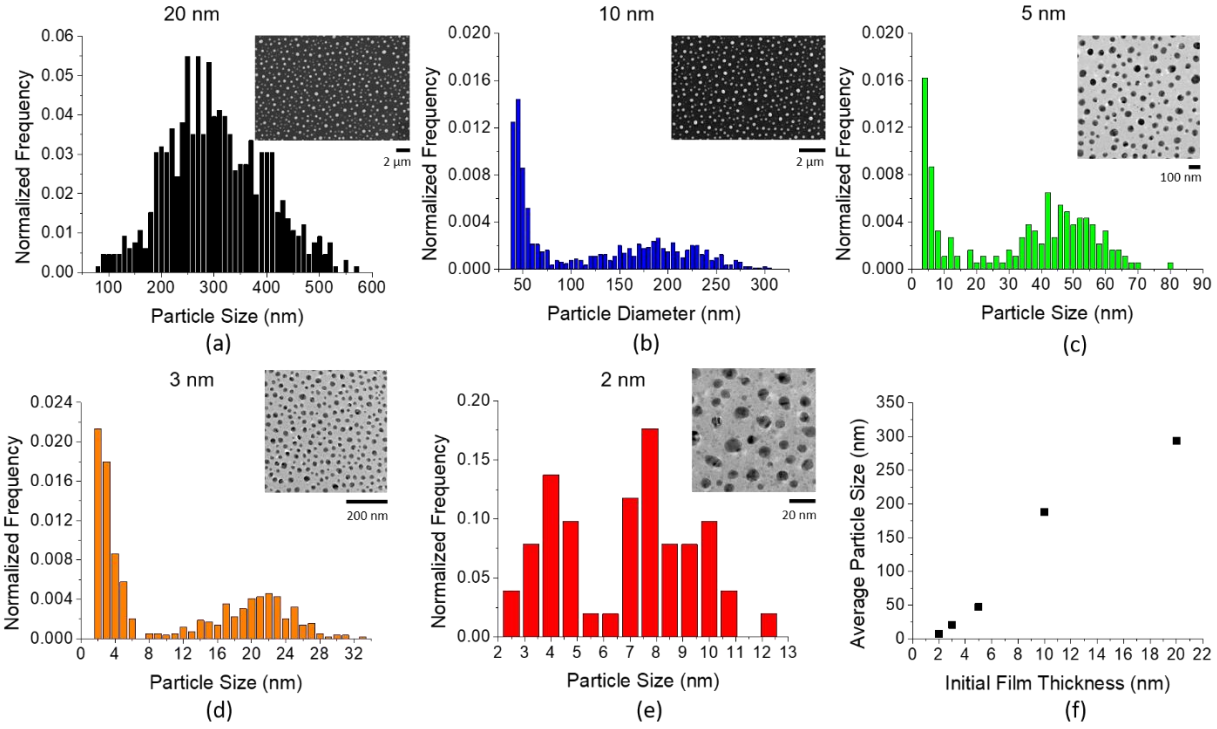

Figure 39: a-e) Particle size distribution of PLiD samples from initial film thickness of 20, 10, 5, 3, and 2 nm, respectively. f) Average particle size of larger mode as function of initial film thickness.

Briefly, an instability is nucleated in the liquid film, which grows and intersects the substrate forming a hole, and a circular rim develops. The circular rims accelerate away from the hole center due to a balance of the capillary, inertial and viscous forces. The circular rims intersect and form a web of rivulets, which subsequently break up into nanoparticles via a Rayleigh-Plateau-like instability mitigated by the substrate. The small nanoparticles typically result from satellite nanoparticles that form in long wavelength Rayleigh-Plateau instabilities[72]. Auspiciously, the larger mode should dominate the behavior of the nanoparticle distribution since these particles dominate the overall material mass. With this in mind, for convenience in the remaining text, PLiD samples will be commonly referred to by their average size of the primary mode, where values 300, 180, 45, 20, and 8 nm, are representative of the 20, 10, 5, 3, and 2 nm initial film thicknesses, respectively. As illustrated in the STEM image in Figure 39c and d (see supplemental information, *Figure S**40***, for enlarged view) a predominantly phase separated Ag-Ni Janus nanoparticle morphology results from the PLiD versus the nanogranular supersaturated solution of the as-deposited thin film.

Magnetic Measurements

To correlate the as-deposited nanogranular mixture of Ag-rich and Ni-rich supersaturated solutions in the as-deposited thin films to the phase separated PLiD nanoparticles, magnetization versus magnetic field (M-H) curves of the as-deposited Ag0.5Ni0.5 thin films (a and b) and nanoparticles generated by PLiD (c and d) are demonstrated in Figure 41 Figure 2. The figures show the M-H results for thin films at 300 K (a and c) and 1.9 K (b and d), respectively. The five curves correspond to the different as-deposited film thicknesses (a and b), which correlate to a peak in the nanoparticle size distribution (c and d) as illustrated in Figure 39.

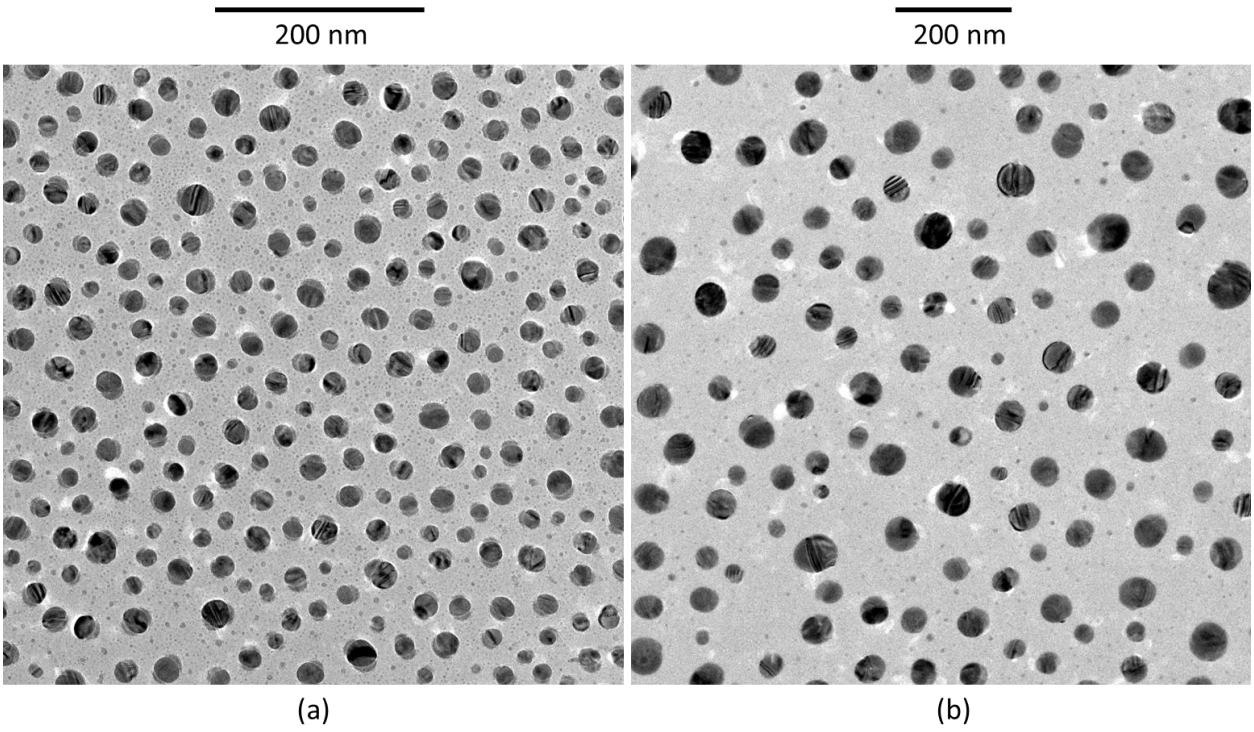

Figure S40: Enlarged TEM images (found in Figure 1) of 3 nm (a) and 5 nm (b) PLiD samples demonstrating Janus particles

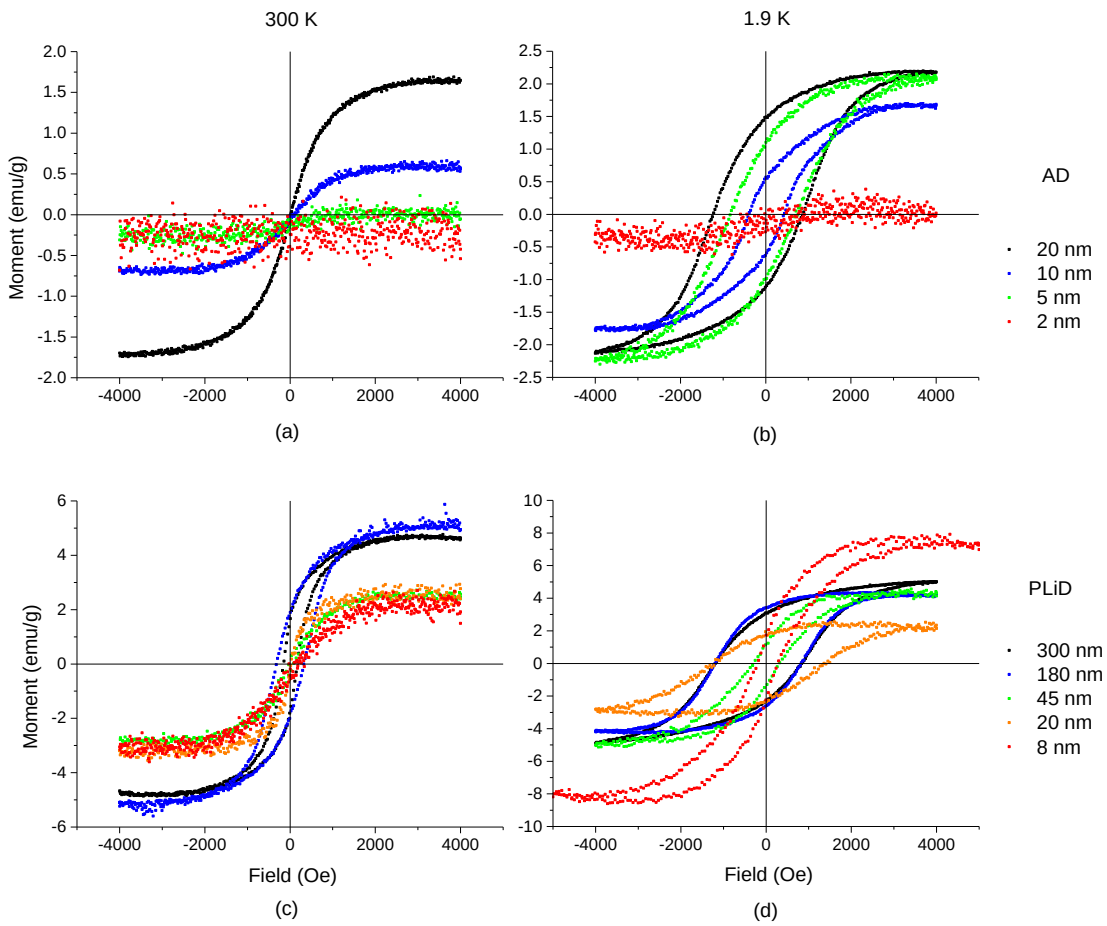

Figure 41: a) and b) Moment vs field plots measured at 300 K and 1.9 K, respectively, for the as-deposited (AD) films, and the c) and d) the PLiD nanoparticles also at 300 K and 1.9 K, respectively.

Excluding of the 2 nm thick film, which has a signal below the noise level of the vibrating scanning magnetometer, all as-deposited films (Figure 41c) are superparamagnetic at 300 K, as indicated by the closed hysteresis loop and sigmoidal field response. At 1.9 K (Figure 41b), the as-deposited films behave as ferromagnets, with the 2 nm film demonstrating a slight diamagnetic tilt, likely from the substrate. Thus, it can be deduced that the blocking temperature, TB, is somewhere between these two temperatures. M-H results at additional temperatures (see Figure S42 in supplemental information) indicate that TB is approximately 200 K for the 20 nm film, 50 K for the 10 nm film, and 1.9 K for the 5 nm film.

Another trend observed in Figure 41b, c, and d is the establishment of an exchange bias in the hysteresis loops, such that they are not centered about zero field. This is most likely an indication of oxidation at the surface of the nanoparticles and the as-deposited film, which leads to the formation of the antiferromagnetic NiO phase. While the Néel temperature of NiO is far above room temperature (525 K), the thin surface oxide does not possess sufficient anisotropy to bias the hysteresis loop and is likely below its blocking temperature as-well. Upon cooling the thermal fluctuations become suppressed, stabilizing the ordering of the antiferromagnet and establishing the exchange bias.

At 300 K, Figure 41c shows that the larger particles (180 and 300 nm) are ferromagnetic, as is evidenced by the open hysteresis loop. The behavior observed in the 45 nm particles, however, is much more subtle, as the measured coercivity is significantly reduced; the coercivity is on the order of 50 Oe (45 nm) compared to 600 Oe (180 nm) and 300 Oe (300 nm). The reduction in coercivity in the 45 nm sample is likely an indication that this particle size is near the single domain transition. For smaller particles, the reversal occurs by a coherent rotation mechanism, while larger particles reverse by a domain nucleation-propagation mechanism. There is an expected loss in

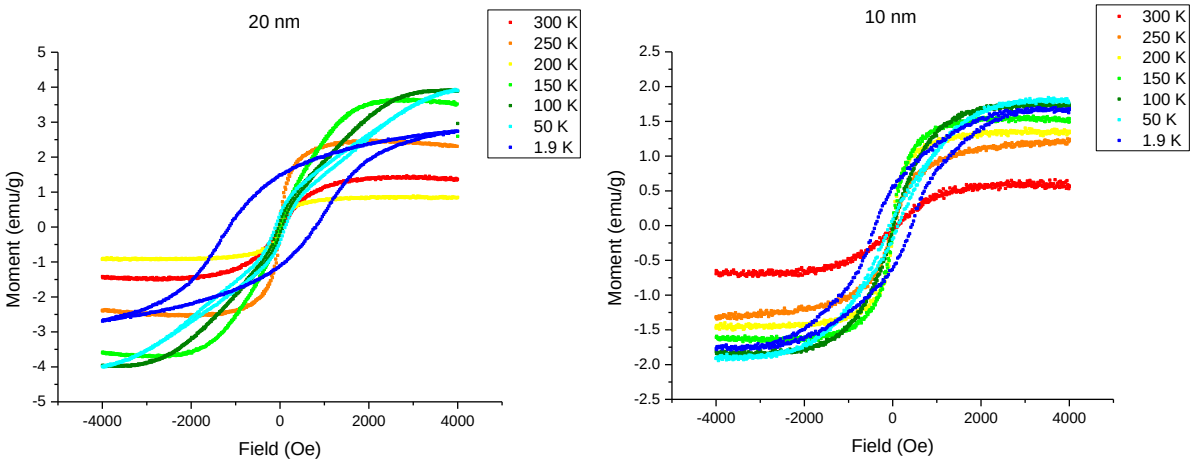

Figure S42: Magnetic hysteresis loops as a function of testing temperature for the 20 and 10 nm as-deposited films

coercivity as the reversal mechanism becomes coherent rotation, that is recovered in the multiple domain regime[142,143].

The two smallest nanoparticle distributions are superparamagnetic at 300 K, as indicated by the sigmoidal and closed hysteresis loop. In this regime, the product of the magnetic anisotropy and magnetic volume is comparable to the thermal energy, resulting in a coherent alignment of the moments within the nanoparticle, but a lack of long term stability of their collective orientation. Thus, it appears that at 300 K the superparamagnetic transition occurs somewhere between 20 and 45 nm in the bimetallic $Ag_{50}Ni_{50}$ nanoparticles. Pure Ni nanoparticles have been found to exhibit room temperature superparamagnetism below a critical diameter of ≈30 nm which agrees well with the observed results[143]. Figure 41d shows the M-H loops measured at 1.9 K, and illustrates that at this temperature all the samples exhibit coercivity. This indicates that even for the 8 nm nanoparticles, the superparamagnetic-to-ferromagnetic transition occurs above 1.9 K.

In Figure 43a-c the M-H plots are included at test temperatures from 1.9 K up to 300 K for the 45, 20 and 8 nm PLID nanoparticles. The 8 nm particles demonstrate a clear superparamagnetic transition between 1.9 K and 50 K, while the 20 nm particles have a transition between 150 K and 200 K, and the 45 nm particles exhibit no superparamagnetic transition up to 300 K. To more accurately determine the blocking temperatures, Figure 43d,e,f is a plot of the magnetic moment as a function of temperature for the 8, 20 and 45 nm particles, respectively. The peaks in the zero field cooled (ZFC) curve reveal the blocking temperatures of the nanoparticle distributions. Experimental values are compared against the calculated values, determined by the equation listed below, where KU is the magnetocrystalline anisotropy of nickel (5.7 ×103 J/m3), V is the particle volume, KB is the Boltzmann constant, τ is the observation time (2 s), and $\tau 0$ is the characteristic flipping time, assumed to be 10-9 s.

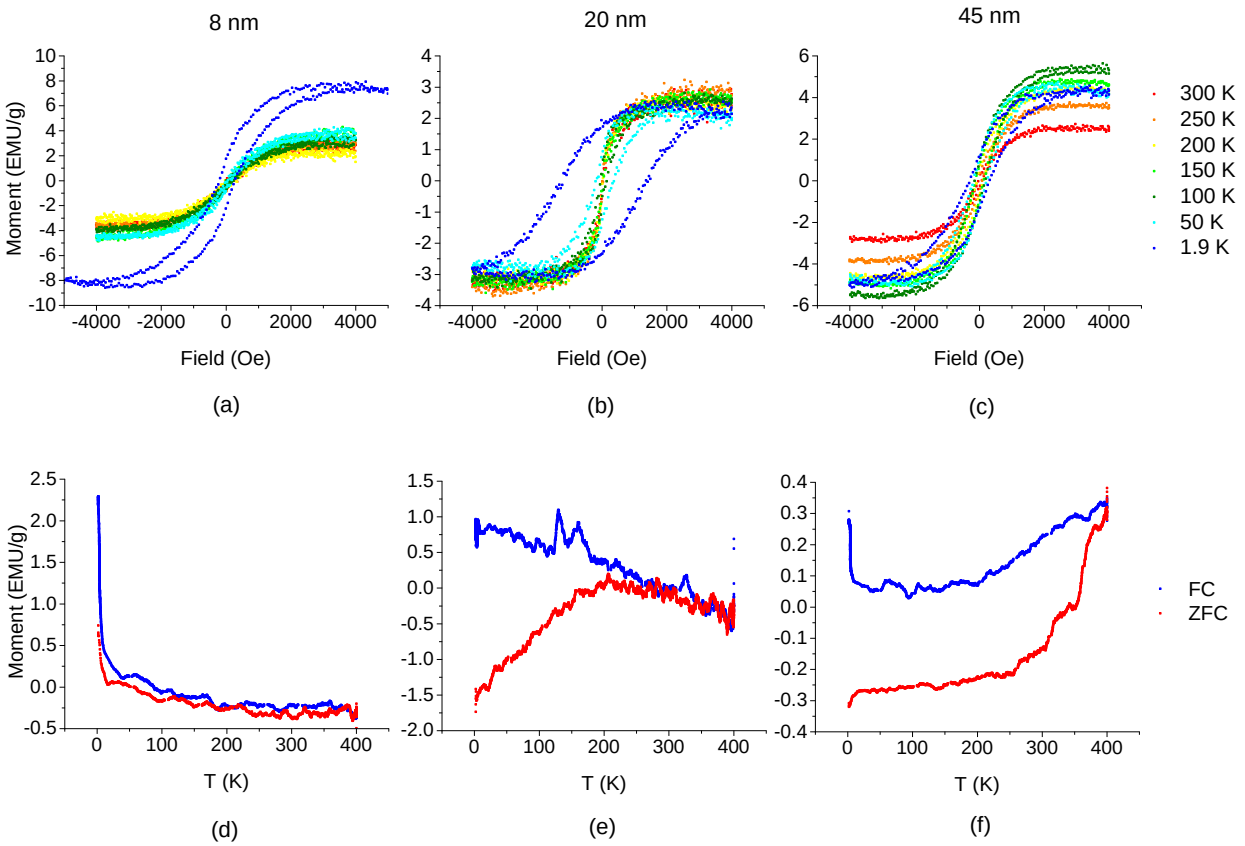

Figure 43: a-c) Moment vs field plots as a function of testing temperature for nanoparticles with sizes of 8, 20 and 45 nm, respectivley, d-f) moment vs T plots showing the field cool and zero field cool for particle sizes of 8, 20 and 45 nm, respectively.

$$T_B = \frac{K_U V}{K_B} \frac{1}{Ln[\frac{\tau_0}{\tau}]}$$

The calculated T_B for the 8 nm particles is 5 K, and so the measurements starting at 2 K leave too little temperature range to resolve the 'bump'. This is consistent with Figure 43d, which shows an up-swing in the M-T curve, but no bump, and Figure 43a, which shows that at 1.9 K the nanoparticles are below T_B. Figure 43e demonstrates a much more pronounced peak, in this case at approximately 200 K, again in agreement with the corresponding M-H plot. However, the calculated value for T_B is lower, at 80 K. The experimentally determined T_B will be sensitive to the largest particles, and so it is not surprising that the experimental value is larger than the calculated. Finally, the 45 nm particles show no blocking temperature, even up to 400 K, consistent with Figure 43c. Calculating T_B for the 45 nm particles indicates a temperature of 982 K, higher than the Currie temperature of Ni.

Optical Transmission

To correlate the as-deposited nanogranular mixture of Ag-rich and Ni-rich supersaturated solutions in the as-deposited thin films to the phase separated PLiD nanoparticles, optical transmission spectroscopy measurements on as-deposited films and PLiD nanoparticle arrays were also performed. Figure 44 illustrates optical absorption spectra for as-deposited films (a) and PLiD samples (b). The as-deposited films exhibit no plasmon peaks except in the 2 nm thick film, where a broad peak is observed at 425 nm (2.92 eV). Here, a peak is observed because the 2 nm thick film is not continuous and instead form isolated islands of material. As film thickness increases the film is continuous by 5 nm thick, and beyond this the absorption increases due to the high imaginary index of refraction of both silver and nickel in this wavelength range.

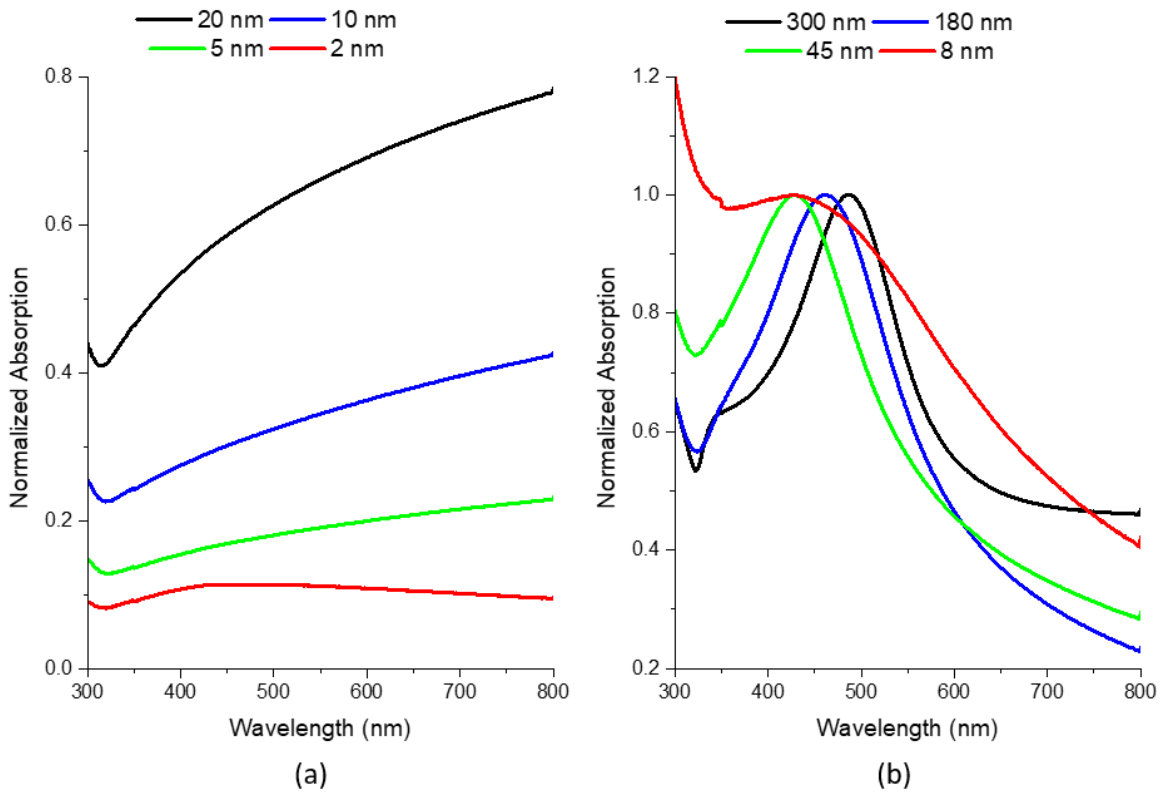

Figure 44: Transmission absorption spectra for a) as-deposited films denoted by their thickness, and b) PLiD samples denoted by their peak in the resultant particle size distribution.

In the PLiD samples, all four particle diameters produce a plasmon peak in the range of 400 – 550 nm (3.10 – 2.25eV). There is the expected blue-shift with decreasing particle diameter, as observed in EELS, from the 300 nm through the 45 nm nanoparticles. From 45 nm to 8 nm, there is slight shift in the peak position back to lower energies; however, there is a significant degree of broadening observed for the 8 nm particles. This broadening obscures the location of the peak, and is likely due to increased scattering from the extremely small size of the nanoparticles. The peak breadth of the 300, 180, and 45 nm samples is quite similar which is surprising due to the variation in particle size distribution observed in Figure 39.

Electron Energy Loss Spectroscopy

In addition to absorption measurements of PLiD nanoparticle arrays, STEM and low-loss EELS were measured on several individual nanoparticles. The most commonly observed particle morphology revealed in the dark field scanning transmission electron microscopy is a Janus particle (see Figure 45e for high angle annular dark field STEM image). Interestingly, while the ensemble composition is ~ $Ag0_{.5}Ni_{0.5}$, the individual nanoparticle composition can vary based on the dewetting dynamics. The slower cooling time associated with the thin suspended membranes allows ample time for the kinetics to drive the particles to what appears to be an equilibrium Janus morphology. Low loss electron energy loss spectroscopy (EELS) is a useful tool to measure the full plasmonic spectrum of plasmonic nanostructures. The Ag-Ni Janus particle morphology yields obvious differences when probing the two sides of a nanoparticle; the EELS spectra for the Ag and Ni sides as a function of particle diameter are included in Figure 45a and b.

In the smallest nanoparticles, probing the Ag hemisphere excites two localized surface plasmon resonance (LSPR) peaks beyond the Ag bulk plasmon (located at ≈3.8 eV): the dipole at 2.9 eV and the quasiplanar mode, which is a mixture of higher order modes with an energy of ≈3.5 eV.

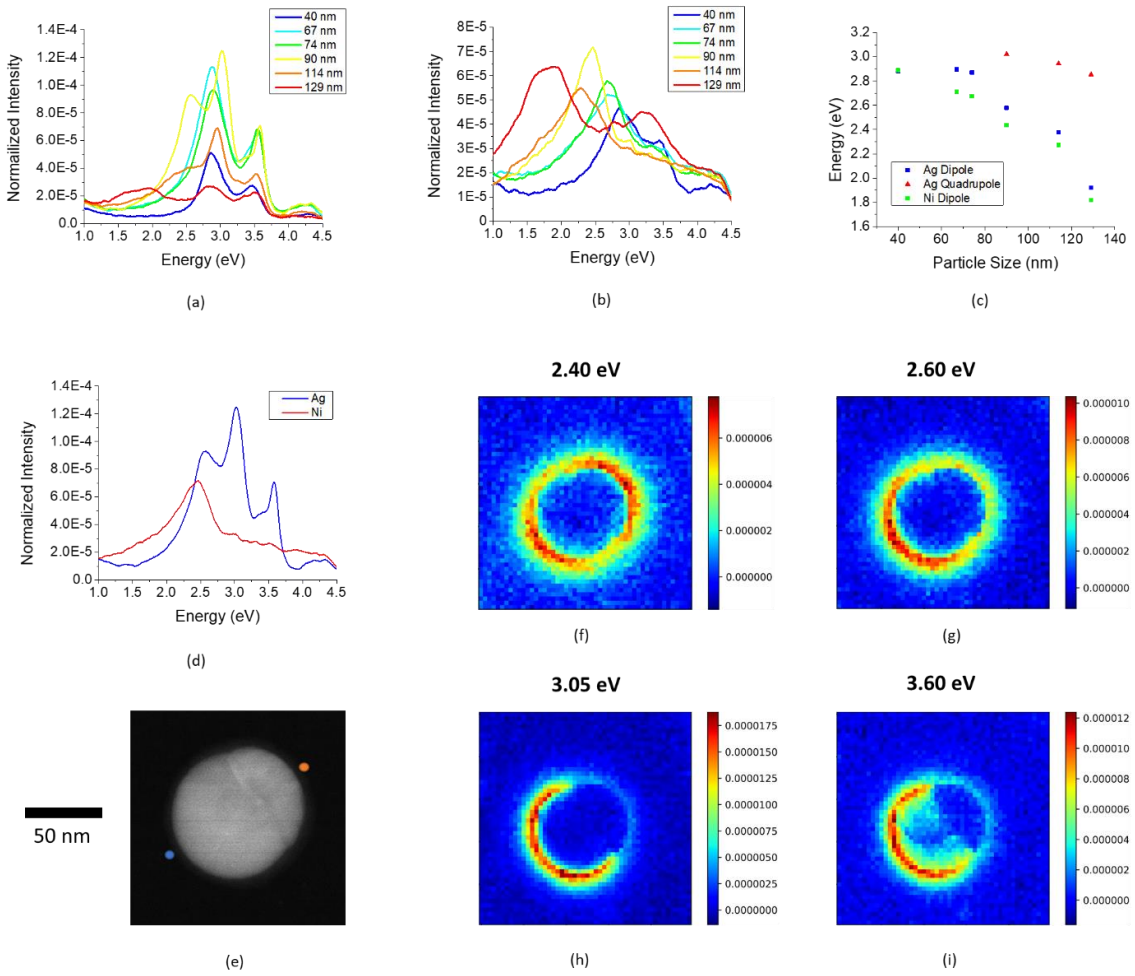

Figure 45: a) EELS spectra from a probe position on the Ag hemisphere as a function of particle size, b) EELS spectra from a probe position on the Ni hemisphere as a function of particle size, c) peak position of Ag and Ni dipole, and Ag quadrupole as a function of particle size, d) EELS spectra for 90 nm particle probed at Ag and Ni ends e) STEM image of 90 nm Ag-Ni Janus particle, f-i) EELS spectrum images demonstrating the plasmon modes of the 90 nm particle shown in e).

As particle size increases the expected red-shift of the dipole peak occurs where the 129 nm nanoparticle exhibits a dipole peak at an energy of 1.9 eV. In addition to the dipole shift, as the particle size increases, the quadrupole first becomes distinguishable from the quasiplanar mode in the 90 nm nanoparticle and then also red-shifts at larger sizes. No other higher order modes emerge from the quasi-planar mode. When probing the Ag side of the 90 nm and 114 nm particles, the peak positions of the dipole, quadrupole, and quasiplanar modes are in very good agreement with the reported peak positions for a pure Ag 100 nm particle[20].

When probing the Ni side of the nanoparticles there is a dipole that is slightly shifted to lower energy relative to the Ag dipole, which is consistent with the Ni dielectric constant. This approximate offset is maintained across all nanoparticle sizes. Because the Ni surface plasmon is significantly damped relative to the silver, identification of any modes beyond the dipole is much more challenging relative to the silver Ag side. There is, however, an additional peak at ≈2.8 eV for the 129 nm particle when probed on the Ni side. The peak position of the Ag dipole and quadrupole, along with the Ni dipole is plotted as a function of particle size in Figure 45c.

The individual point spectra for the Ag and Ni hemispheres of the 90 nm particle are included in Figure 45d (see Figure S46 in supplemental information for STEM images Figure 45e-i shows the HAADF STEM image of the 90 nm nanoparticle and the associated EELS maps for this particle to visualize the LSPR modes. Each map is associated with a specific energy window, and the color contrast indicates the relative intensity in the chosen energy range. The lowest energy map, at 2.4 eV, demonstrates the Ni dipole where the intensity is elevated all around the particle, and is a maximum at the Ag and Ni ends; the peak on the Ag end is due to the fact that the Ag dipole peak has an appreciable signal at 2.4

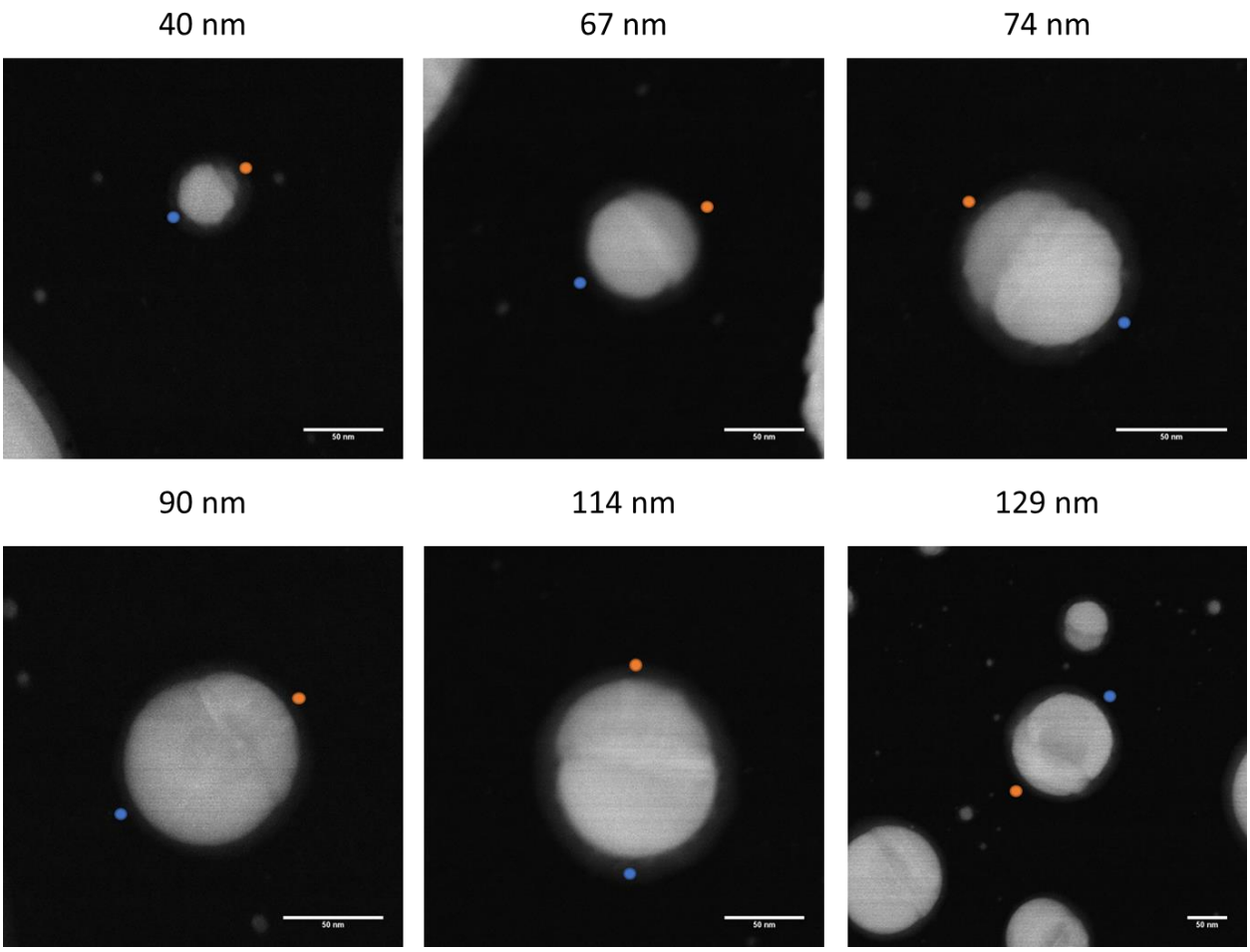

Figure S46: STEM images of PLiD EELS samples demonstrating Janus particles via Z-contrast imaging

eV. The Ag dipole, 2.6 eV, possesses a similar signature, however, the intensity is much lower on the Ni side. The final two maps (Figure 45h and 5i) show the Ag quadrupole and the Ag quasiplanar modes. Both modes are brightest around the Ag hemisphere. The primary difference between the two modes is that the quadrupole near field extends farther from the nanoparticle surface, whereas the quasiplanar mode has a much stronger signature in the bulk.

Conclusions

Magnetic and optical characterization has demonstrated that Ag-Ni nanoparticles fabricated via PLiD possess interesting magneto-plasmonic bi-functionality. The initially nanogranular continuous 2D thin films are composed of an Ag-enriched supersaturated solid solution and a Ni-enriched supersaturated solid solution. The Ag-Ni films form Ag-Ni nanoparticles on various substrates following photothermal nanosecond pulsed laser heating. Varying the thickness of the $Ag_{0.5}Ni_{0.5}$ thin films prior to dewetting provided good control over nanoparticle size distributions. By controlling the size of the nanoparticles, room temperature magnetic properties can be tailored from ferromagnetic (>20 nm) to superparamagnetic (<20 nm). Additional trends, such as a transition from a single to multi domain magnetic regime, and the superparamagnetic transition temperature were also demonstrated. Optically, STEM EELS and optical absorption measurements show the expected trend of red-shifting the LSPR peak with increasing nanoparticle size. Samples fabricated for STEM EELS demonstrated Ag-Ni Janus particles as the dominant nanoparticle morphology. These Janus nanoparticles were found to possess an LSPR dipole peak at an energy corresponding to both Ag and Ni, depending on the hemisphere where the sample is probed. The Ni hemisphere in general have more damped and lower energy LSPRs, whereas the stronger LSPRs in the Ag hemispheres exhibit a clear dipole, quadrupole and quasiplanar mode at larger particle sizes.

Methods

Materials

$Ag_{0.5}Ni_{0.5}$ thin films were synthesized via radio frequency magnetron co-sputtering. A base pressure of < $4x10^{-7}$ Torr was achieved for all samples, and sputtering was conducted at a pressure of 5 mTorr with an Ar flow rate of 25 sccm. Forward powers of 70 W and 40 W were used for Ni and Ag targets, respectively, to ensure an ~50/50 composition (confirmed via energy-dispersion x-ray spectroscopy). The as-deposited film forms as a supersaturated nanocrystalline solid solution[121].

Films of 20 nm, 10 nm, 5 nm, 3 nm, and 2 nm were deposited on various substrates and tested as-deposited as well as following PLiD. Magnetic samples were deposited on 100 mm diameter, 500 µm thick Si wafers coated with 100 nm of thermally grown SiO_2 to act as a thermal and chemical insulating layer. Samples prepared for optical transmission testing were deposited on 100 mm 500 µm thick quartz substrates. Finally, transmission electron microscope (TEM) and electron energy loss spectroscopy (EELS) samples were deposited on commercial 20 nm thick, 50 µm x 50 µm SiO_2 membranes.

Nanoparticles were formed through PLiD using a krypton fluoride excimer laser with a wavelength of 256 nm. The laser has a Gaussian temporal distribution with a full width half max of ≈20 ns. Samples were subjected to 10 pulses with a fluence of approximately 170 mJ/cm^2 for samples deposited on the 100 nm SiO_2/silicon wafers, and 1 pulse at ≈50 mJ/cm^2 on TEM membrane samples. Due to the significant difference in substrate heat conduction, more pulses at higher fluence were required for the 100 nm SiO_2/silicon wafers to achieve a similar stage of dewetting as was achieved with a single pulse at lower fluence on the 20 nm SiO_2 suspended membrane.

VSM

The magnetic properties of AgNi were characterized using a vibrating sample magnetometer (VSM) on a PPMS DynaCool. The magnetization vs temperature curve was measured by zero field cooling (ZFC) and field cooling (FC) from 1.9 K to 400 K with an external magnetic field of 50 Oe. The measurement time per point was 2 s. The magnetic hysteresis loop of the sample proceeded from -4000 Oe to 4000 Oe at temperatures between 2 K and 300 K.

Transmission:

Optical transmission spectroscopy was conducted on as-deposited thin films and PLiD samples. A 10 mm aperture was used for the as-deposited films, while a 1 mm aperture was used following laser treatment. A wavelength range of 200 – 1000 nm was used.

EELS

Low-loss EEL spectra and spectrum images were taken using a Nion aberration-corrected high energy resolution monochromated EELS-STEM (HERMES) operated at an accelerating voltage of 60 kV. The convergence and collection semiangles used for the spectrum acquisition were 30 and 15 mrad, respectively. The energy resolution (full width at half-maximum of the zero-loss peak) was approximately 20 meV. The EEL spectra presented in **Error! Reference source not found.** were normalized to the zero-loss peak.

Acknowledgements

PDR and DAG acknowledge support from the National Science Foundation (CBET-1603780). IV and JDF acknowledge support from the US Department of Energy (DOE) under grant number KC 0403040 ERKCZ01. GP acknowledges the National Science Foundation (NSF DMR 1709275). DAG acknowledges support from the DOE Early Career Program. All the authors

acknowledge that the absorption and EELS measurements was conducted at the Center for Nanophase Materials Sciences, which is a DOE Office of Science User Facility.

References

CHAPTER III
MAGNETO-PLASMONIC PROPERTIES OF AU_XCO_{1-X} SOLID SOLUTION AND PHASE SEPERATED THIN FILMS AND NANOPARTICLES

Magneto-Plasmonic Properties of Au_xCo_{1-x} Solid Solution and Phase Separated Thin Films and Nanoparticles

David A. Garfinkel[1], Nan Tang[1], Grace Pakeltis[1], Reece Emory[1], Ilia N. Ivanov[2], Dustin A. Gilbert[1], Philip D. Rack[1,2]
1. Department of Materials Science and Engineering, University of Tennessee, Knoxville, Tennessee 37996, United States
2. Center for Nanophase Materials Sciences, Oak Ridge National Laboratory, Oak Ridge, Tennessee 37831, United States

Authors Contribution

The author led all sample fabrication including thin film sputtering, pulsed laser induced dewetting, and annealing. The author also performed all scanning electron microscope (SEM), energy-dispersive x-ray spectroscopy (EDX), profilometry, and transmission spectroscopy with initial assistance from Ilia Ivanov. The author was also responsible for all data processing, analysis, generation of figures, and writing of the paper. Collaborator Grace Pakeltis performed the electron energy loss spectroscopy, while Nan Tang and Dustin Gilbert were responsible for the measurement of the magnetic properties.

Introduction

Alloying in metallic nanomaterials is a powerful technique to not only control individual material properties, but also to create multi-functionality i.e., simultaneous magnetic and plasmonic properties. When introducing additional components to a material system, factors such as chemical composition, mixing behavior, and changes to equilibrium crystal structure, all can have a profound influence on the material properties. Physical vapor deposition provides a convenient tool for rapidly achieving thin film nanomaterials over a large compositional range. Further, the high energy deposition process allows for the realization of material configurations that are outside of bulk thermodynamic behaviors. An example being the as-deposited supersaturated solid

solution found in various sputtered nanoalloys[121,144,145]. Annealing can then be used to achieve the thermodynamic state of the system through recrystallization, grain growth, and phase separation. Higher temperature heat treatments can be used to alter the physical morphology of the metallic thin films through a process called dewetting. The exceptionally high surface energy inherent to thin films, due to the large ratio of surface area to volume, renders the as deposited films metastable. The energetically stable configuration is an array of spherical caps with wetting angles and diameters dependent on the substrate/material properties and thin film thickness. Timescales to reach this state at room temperature are exceedingly long, and thus thin films maintain their shape at room temperature for long periods of time. Introduction of heat greatly accelerates the dewetting dynamics and can shorten the duration to nanoseconds when ultrathin films liquify. The use of a pulsed laser to generate these arrays of nanoparticles is termed pulsed laser induced dewetting (PLiD), and a review on the hydrodynamics can be found here[17,18,33,146]. The rapid processing time associated with this technique can also create chemical configurations outside of equilibrium that can be altered with annealing.

Nanomaterials possessing combined magnetic and plasmonic properties have recently emerged as enticing functional materials in various applications including cancer detection and treatment[128,147–149], magnetic resonance imaging[150,151], data storage[152], and mechanochromic devices[153]. These properties are predominantly achieved with nanoparticles in the $Fe_{3-x}O_4$ material system, though AuCo also demonstrates this bi-functionality, in addition to attractive catalyst capabilities[154,155]. The majority of research on AuCo nanoparticles has been focused on nanoparticles achieved via chemical growth techniques[156–158]. Research in the thin film configuration have been studied as multi layers for data storage[152], and as deposited, via evaporation[159–161] and sputtering[40,162,163] with much of the fucus on the material structure[160,162],

which has been observed as a solid solution, amorphous, and a solid solution with interspersed Au and Co particles.

In previous work we have demonstrated magneton radio frequency sputtering and PLiD as a robust technique for synthesis of magneto-plasmonic bi-functionality[164]. The size of as deposited $Ag_{50}Ni_{50}$ thin films and PLiD nanoparticles provided a tunable parameter for the magnetic and plasmonic properties, namely exhibiting control in LSPR resonance frequency and superparamagnetic blocking temperature. Here, we expand upon this research in a new material system, Au_xCo_{1-x}, by examining the influence of composition and chemical morphology on the material properties. The as deposited thin film and as PLiD nanoparticles are compared with phase separated thin films and nanoparticles at three compositions within a large compositional range. We perform exhaustive characterization that includes vibrating sample magnetometry (VSM), ellipsometry, optical transmission spectroscopy, and electron energy loss spectroscopy (EELS) to better under the interplay between composition, physical and chemical morphology, and magnetic and optical properties.

Materials Synthesis

Sputtered Thin Film

Figure 47a is a schematic of the sputtering configuration used to synthesize a wide range of compositions of mixed Au_xCo_{1-x} thin films for initial characterization. The substrate is placed in between a pure Co and pure Au sputtering target (Figure 47a). Because both targets are oriented at an angle with respect to the substrate, the deposition rate of each target is variable depending on the location of the substrate: the areas on the substrate closest to each target will be rich in that element. Thus, with a stationary substrate throughout the deposition, a compositional gradient is achieved across the substrate, as demonstrated in Figure 47b. Conversely, by rotating the substrate

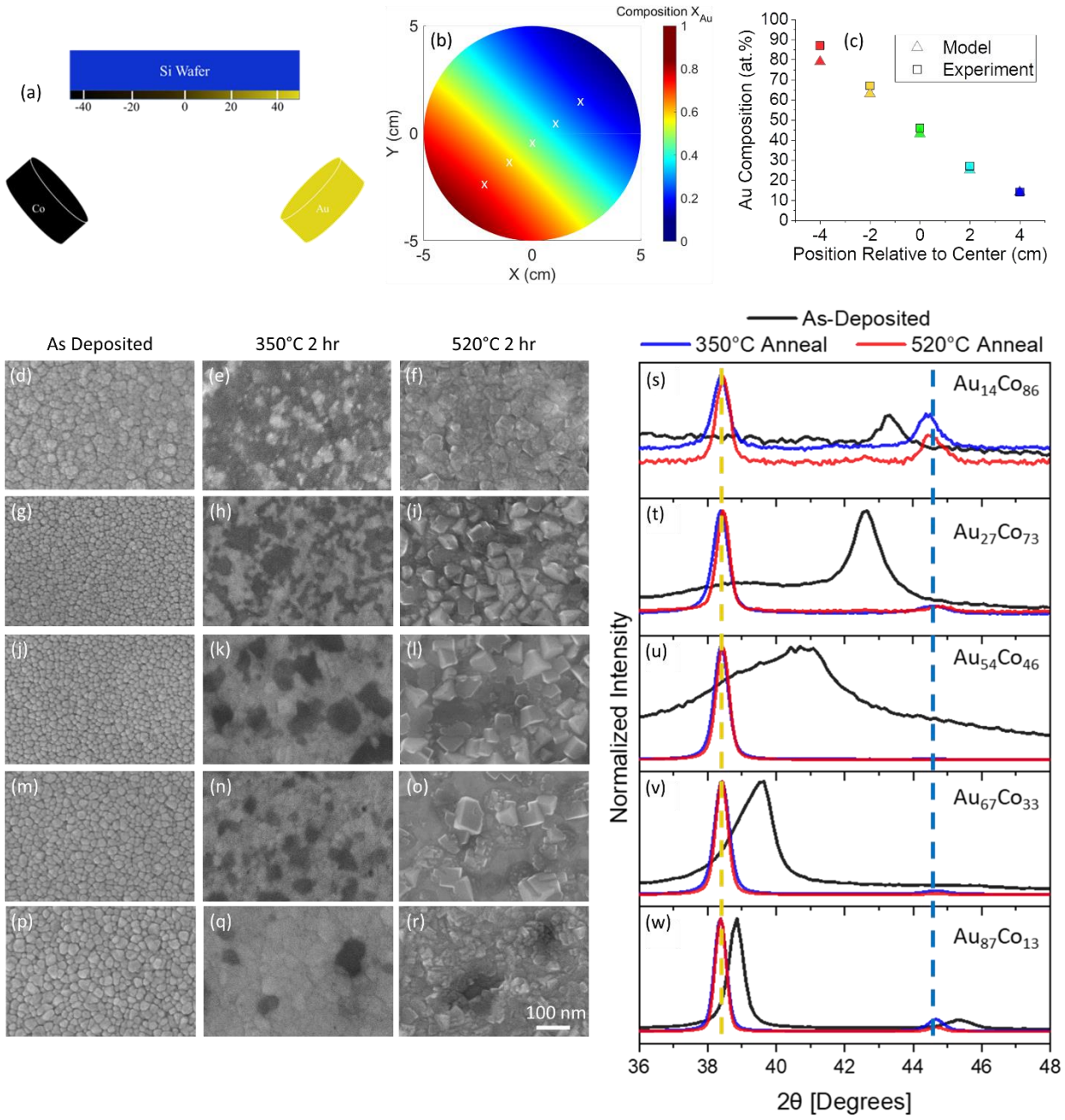

Figure 47: a) Representation of AuCo combinatorial sputtering, b) modelled compositional gradient across the AuCo thin film after combinatorial sputtering, c) comparison of model vs experiment, d-r) SEM images. of the thin films, s-w) X-ray diffraction at five compositions along the chemical gradient of as deposited (black) and annealed (blue at 350°C and red at 520°C) thin films.

during deposition, a continuous composition of the two elements is obtained across the entirety of the substrate. In this paper both methods are utilized. The combinatorial sputtering approach (stationary substrate) was used for the initial characterization of the material system. Then co-sputtering (rotating substrate) was utilized to synthesize thin films with three specific compositions for PLiD and further characterization.

To determine the crystal structure of the combinatorially sputtered AuCo thin film for various compositions, x-ray diffraction (XRD) was conducted at five equally spaced locations along the chemical gradient on both an as deposited and annealed ~400 nm thick sample. Annealing was performed in vacuum at two temperatures: one in the HCP+FCC region of the phase diagram (350°C for 2 hrs), and the other, in the FCC+FCC region (520°C for 2 hrs). The compositions, as determined via energy-dispersive x-ray spectroscopy (EDX), were $Au_{87}Co_{13}$, $Au_{67}Co_{33}$, $Au_{48}Co_{52}$, $Au_{27}Co_{73}$, and $Au_{14}Co_{86}$. Figure 47c-g demonstrates that the as deposited films form an Au_xCo_{1-x} FCC solid solution, contrary to the phase separated thermodynamic equilibrium state. This is apparent by the absence of peaks at angles associated with the FCC (111) orientation of pure Au (~38°) or pure Co (~44°), and instead the presence of peaks in between that shift in 2θ consistent with compositional changes. The most Au-rich and Co-rich positions, exhibit a single composition of the solid solution, indicated by a single (111) peak. The remaining three compositions demonstrate a primary peak with a shoulder, or a second peak in the case of the $Au_{27}Co_{73}$, suggesting that there is a wider distribution of solid solution compositions present. None of the compositions that were tested displayed any evidence of the Co HCP structure. The scanning electron microscope (SEM) images included in Figure 47 demonstrate the extremely fine grain structure (>10 nm) with no differentiation between the solid solution compositions for any of the compositions.

Annealing in the HCP+FCC and FCC+FCC temperature ranges resulted in nearly identical behaviors in XRD. The solid solution peaks disappear and are replaced by peaks at ~38° and ~44°. The first peak can easily be identified as the Au FCC (111), while the second peak has two potential contributions: the Co FCC (111) peak discussed above or the Au (200) that is also located at ~44°. In the most Au-rich samples, the Au (111) peak is much greater than the ~44° peak, whereas in the $Au_{14}Co_{86}$, the relative intensities are much closer. For this reason, it can be deduced that the increased Co content has enhanced the signal of the Co (111) peak enough to be discernable. Regardless of the presence of a Co (111) peak, the disappearance of the solid solution, and emergence of the Au (111) indicates phase separation has successfully been induced from annealing. Further, there remain no discernible HCP peaks regardless of annealing temperature.

The low temperature annealing produces clear z-contrast in the SEM images seen in Figure 47, where the higher Z element, Au, appears brighter. EDX mapping confirms this contrast and can be clearly seen in Figure 48. As would be expected, as the Co composition increases, the frequency of Co grains increases, though the size of the grains appears to be largest at the $Au_{48}Co_{52}$ composition. The distribution of Co islands within an Au matrix is maintained up until the highest Co concentration, where the behavior is inversed. Increasing the annealing temperature leads to formation of large crystals at the surface that obscure the differentiation between the two elements. Following initial characterization, thinner films were synthesized for magnetic and optical testing. Here, three compositions were selected for characterization. Due to the inability to characterize the HCP peak, annealing was focused on the FCC+FCC region of phase diagram, to avoid confusion. An annealing temperature of 450°C was chosen to be above the HCP region and at a lower temperature than the previously used 520°C in the hopes of reducing the large surface crystal formations. Figure 2 shows that very similar as deposited morphology is observed and following

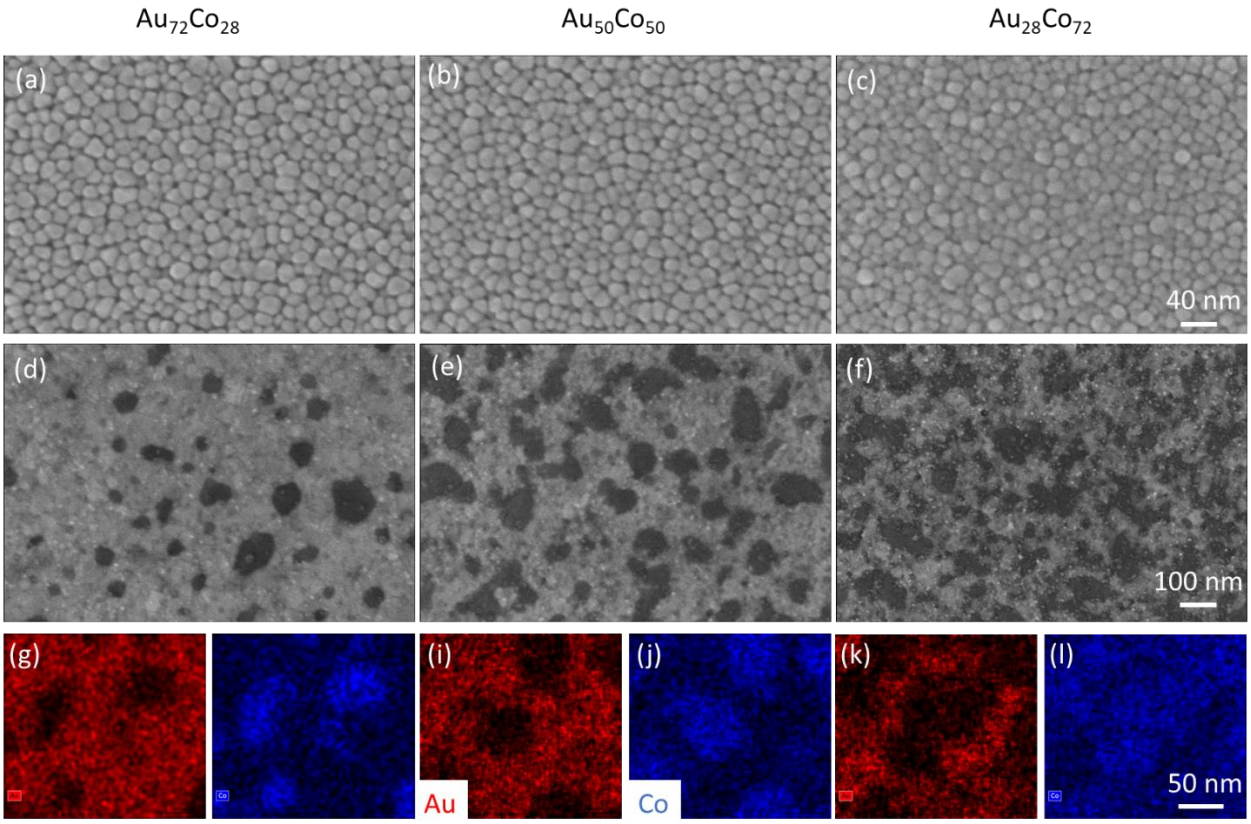

Figure 48: a-c) SEM images of the 60 nm thin films of the three compositions, d-f) SEM images *demonstrating the phase separation caused by annealing, g-l) EDX maps indicating the dark regions in d-f are Co while the light areas are Au.*

annealing large phase separation is achieve without the crystallization observed in Figure 47. Figure 48g-l provides validation for the phase contrast identification from Figure 47d-f.

Nanoparticles via Pulsed Laser induced Dewetting (PLiD)

Au_xCo_{1-x} spherical cap nanoparticles, as seen in Figure 49, were synthesized from 10 nm co-sputtered thin films via PLiD. While nanoparticles synthesized for magnetic testing allowed for processing on "bulk" 500 μm thick Si substrates (coated with 100 nm SiO_2), optical measurements necessitated electron and optically transparent substrates. Here, a 40 nm thick low stress SiN_x membrane (~150 μm x ~150 μm) supported by a 300 μm thick Si frame was used. Previous work[165] on 10 nm thick $Ag_{60}Ni_{40}$ thin films provides approximate heating conditions required to generate nanoparticles on both substrates, and indicates a liquid lifetime requirement of approximately 20 ns for dewetting. Despite identical metal deposition on the two substrates, the variation in substrate drastically alters the thermal behavior. Finite element thermal simulations shown in Figure 49j indicate that a fluence of ~140 mJ/cm^2 provides a sufficient liquid lifetime for the bulk substrates while only ~40mJ/cm^2 is necessary for the thin transparent substrates. Not only are energy input requirements different, the liquid lifetime and cooling times are significantly longer on the thin membrane compared to thick substrate (nanoseconds compared to milliseconds).

Figure 49 demonstrates that following PLiD, nanoparticles appear homogenous whereas annealing results in distinct contrast indicating phase separation: as was the case with the thin films, the dark areas correspond to Co. The three different compositions $Au_{66}Co_{34}$, $Au_{48}Co_{52}$, and $Au_{22}Co_{78}$ exhibit nearly identical behaviors following PLiD. Annealing for 20 mins, compared to 60 mins does not result in markedly different behaviors, though there does appear to be some additional conglomeration of phase separated areas into slightly large phase separated areas. Although there does not appear to be an equilibrium chemical morphology for any composition, the $Au_{66}Co_{34}$

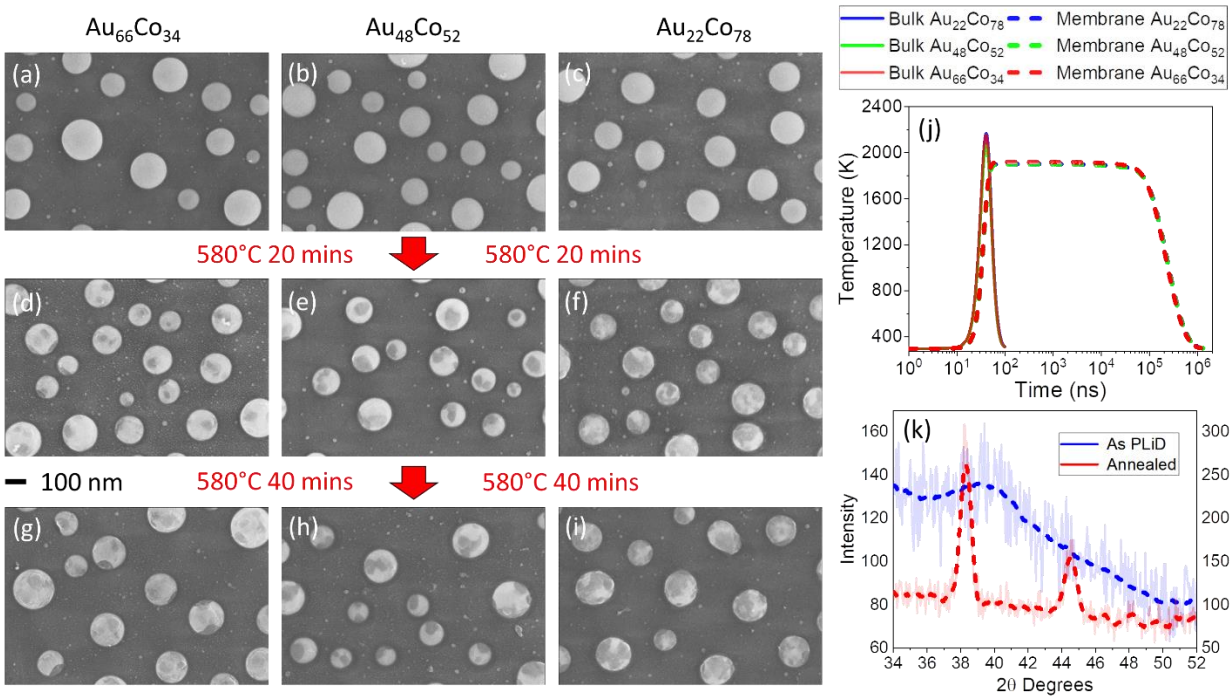

Figure 49: a-c) Particle diameter distribution following PLiD on three different composition thin films, d-i) shows the particle morphology following annealing, j) XRD measurements on the Au50Co50 as PLiD and annealed samples, k) thermal simulations for the three 10 nm thin films.

sample is predominantly small Co cores that transition to the surface, a similar behavior is observed in $Au_{48}Co_{52}$, albeit with larger Co regions, and the $Au_{22}Co_{78}$ is largely Co with Au areas seemingly randomly distributed in the nanoparticle. XRD measurements of a PLiD sample prior to annealing and after (Figure 49k), indicate that the as PLiD nanoparticles have a Au_xCo_{1-x} solid solution structure, and that annealing induces phase separation; similar to what was observed in the as deposited and annealed thin films. The combination of liquid miscibility, rapid cooling, and slow kinetics allow for the generation of non-equilibrium Au_xCo_{1-x} solid solution nanoparticles. It should be noted that XRD signal is significantly reduced in Figure 49 compared to Figure 47 due to reduced dimensions of the tested samples owning to the small laser spot (>1 cm^2) and thinner (10 nm vs 400 nm) deposited thin film.

Magnetic Properties

Thin Films

The magnetic properties of the Au_xCo_{1-x} thin films prior to and after annealing were characterized by vibrating sample magnetometry (VSM). These results are expressed as M vs. H plots at two different test temperatures (2 K and 400 K) in Figure 50a and b, respectively. At 2 K, all samples exhibit ferromagnetism, as would be expected from Co, which is identified via the characteristic coercivity (opening of the hysteresis loop). At 400 K, the coercivity is decreased; however, ferromagnetism is maintained for all samples other than the as deposited $Au_{72}Co_{28}$ sample. The absence of coercivity, and a peak in the zero field cool plot at ~210 K (Figure 50c) indicates that this film is exhibiting a superparamagnetic behavior above this blocking temperature. The magnetic anisotropy of pure Co in the HCP structure is exceptionally high, making the formation of superparamagnetism very challenging. Here, the combination of the FCC structure (lower magnetic anisotropy), grain size (~10 nm), and prevalence of Au within the solid solution make

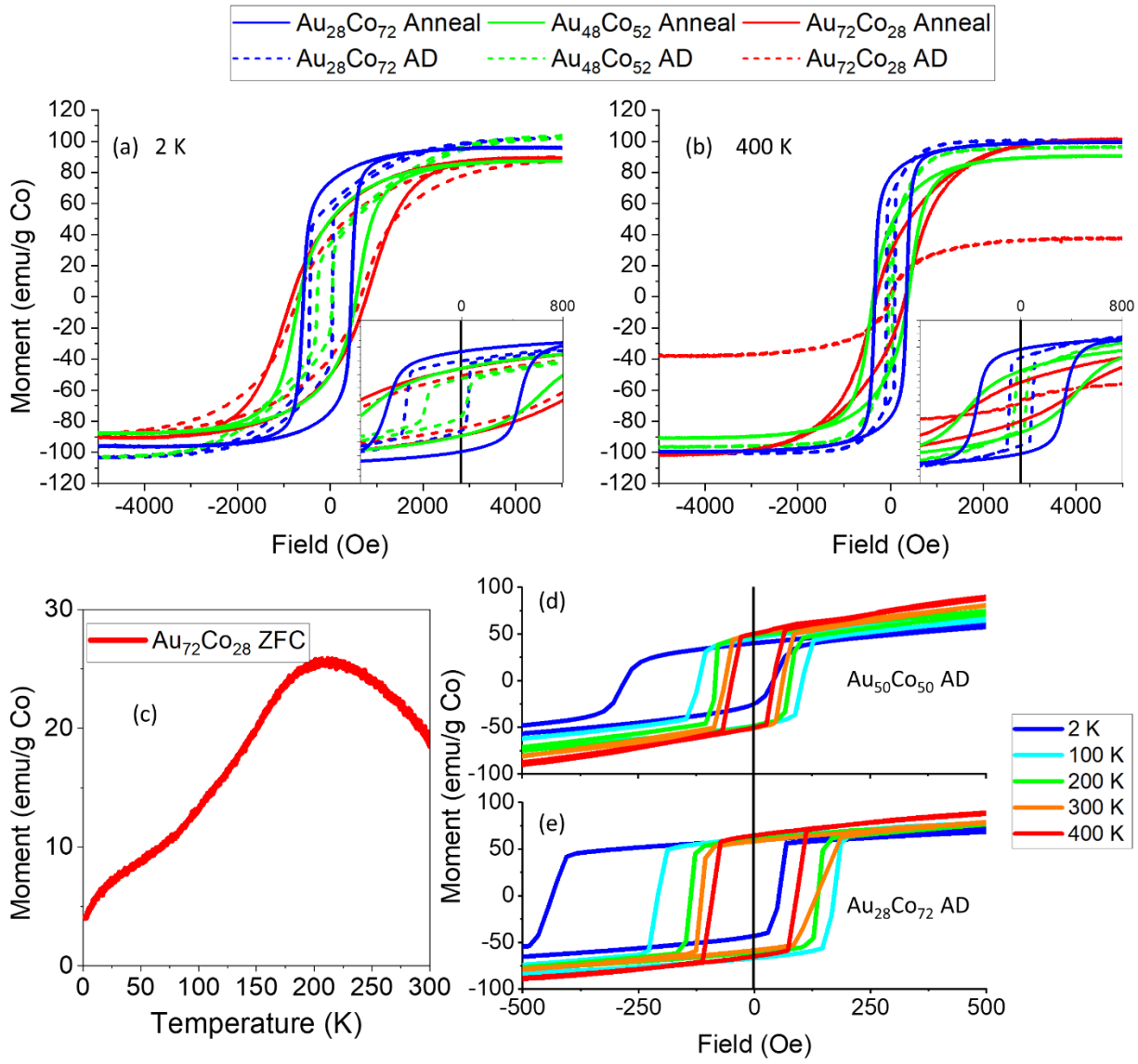

Figure 50: M vs H plots at 2 K (a) and 400 K (b) for the as deposted and phase seperated 2D Au72Co28, Au50Co50, and Au72Co28 thin films, c) ZFC plot for the as deposited Au-rch thin film, d and e) demonstrate the temperature dependance of the Au50Co50 and Au72Co28 samples.

this behavior possible. After annealing, large Co grains form which increases the magnetic anisotropy, thus increasing the blocking temperature to above 400 K and leading to ferromagnetism as seen in Figure 50b. The other as deposited films exhibit a similar nanogranular structure, but do not have this same superparamagnetic behavior. This is due to the reduction of Au in the solid solution, leading to greater magnetic anisotropy, and either an increase in the blocking temperature, or a transition to a multidomain state.

In Figure 50 all magnetic moment measurements have been normalized to the estimated Co mass of each sample. This normalization leads to similar saturation magnetizations for each sample, outside of the $Au_{72}Co_{28}$ as deposited film above its blocking temperature. This is indicating that there is very little contribution from Au on the saturation magnetization. There are however significant differences in the reversal behavior that can be linked to the nanostructure of the films. The Co grains within the $Au_{72}Co_{28}$ film are highly isolated and demonstrate a wide distribution in size. For this reason, the individual grains do not communicate, and the result is a wide distribution of reversal behaviors averaged together to make a gradually sloped reversal curve. The $Au_{50}Co_{50}$ sample still clearly has Co islands in an Au matrix; however, the size of these grains is more consistent than that the $Au_{72}Co_{28}$ samples, and there is a beginning to an interconnected structure, and thus the slope of the reversal curve is increased. Finally, the $Au_{28}Co_{72}$ thin film exhibits clear interconnection between the grains leading to a markedly different reversal behavior. Here nucleation begins much later than in the other films, and then at a critical field, there is rapid reversal of the magnetization.

There is an obvious shift in the hysteresis loops of the as deposited $Au_{28}Co_{72}$ and $Au_{50}Co_{50}$ samples towards the negative field. This behavior is due to exchange bias, which can be caused by an

interface between an antiferromagnetic and a ferromagnetic material. The interface delays the initiation of the ferromagnetic behavior as it requires more energy to overcome the polarization created at this interface, thus shifting the ferromagnetic behavior toward the negative field in the plot. The ferromagnetic component in the material is clearly Co; however, the antiferromagnetic contribution could be attributed to CoO, Co_3O_4 or the interactions between Au and Co. The exchange bias disappears with increasing test temperature as well as through annealing. Figure 50c and d show M vs. H plots for $Au_{50}Co_{50}$ and $Au_{28}Co_{72}$, respectively, at five different testing temperatures. The exchange bias is largely eliminated by increasing the test temperature from 2 K to 100 K. The Neel temperature of CoO is ~300 K, so it is unlikely that the exchange bias is due to CoO. Co_3O_4 on the other hand has a Neel temperature of approximately 30 K; however, the formation of Co_3O_4 is observed at elevated temperatures, which should not occur in the as deposited films. Further, reduction in exchange bias from annealing also contradicts the possibility of Co oxides, because annealing would be expected to increase oxide formation, and thus enhance exchange bias. Annealing does, however, reduce the solid solution Au_xCo_{1-x} and with that many of the Au and Co interactions. For these reasons it appears likely that the exchange bias is primarily due to Au and Co interactions.

Nanoparticles

The magnetic properties of the nanoparticles shown in Figure 51 were measured using VSM. The $Au_{22}Co_{78}$ and $Au_{48}Co_{52}$ PLiD nanoparticles exhibit an interesting behavior called a "wasp-waisted" hysteresis loop. The geometry of the nanoparticles allows for magnetic domains to generate a vortex around the circumference of the nanospheres. When the nanoparticles are in the saturated state, all moment are aligned. When the field is cycled in the opposite direction, reversal begins, and the vortex begins to form as the moment decreases from the saturation point, near zero

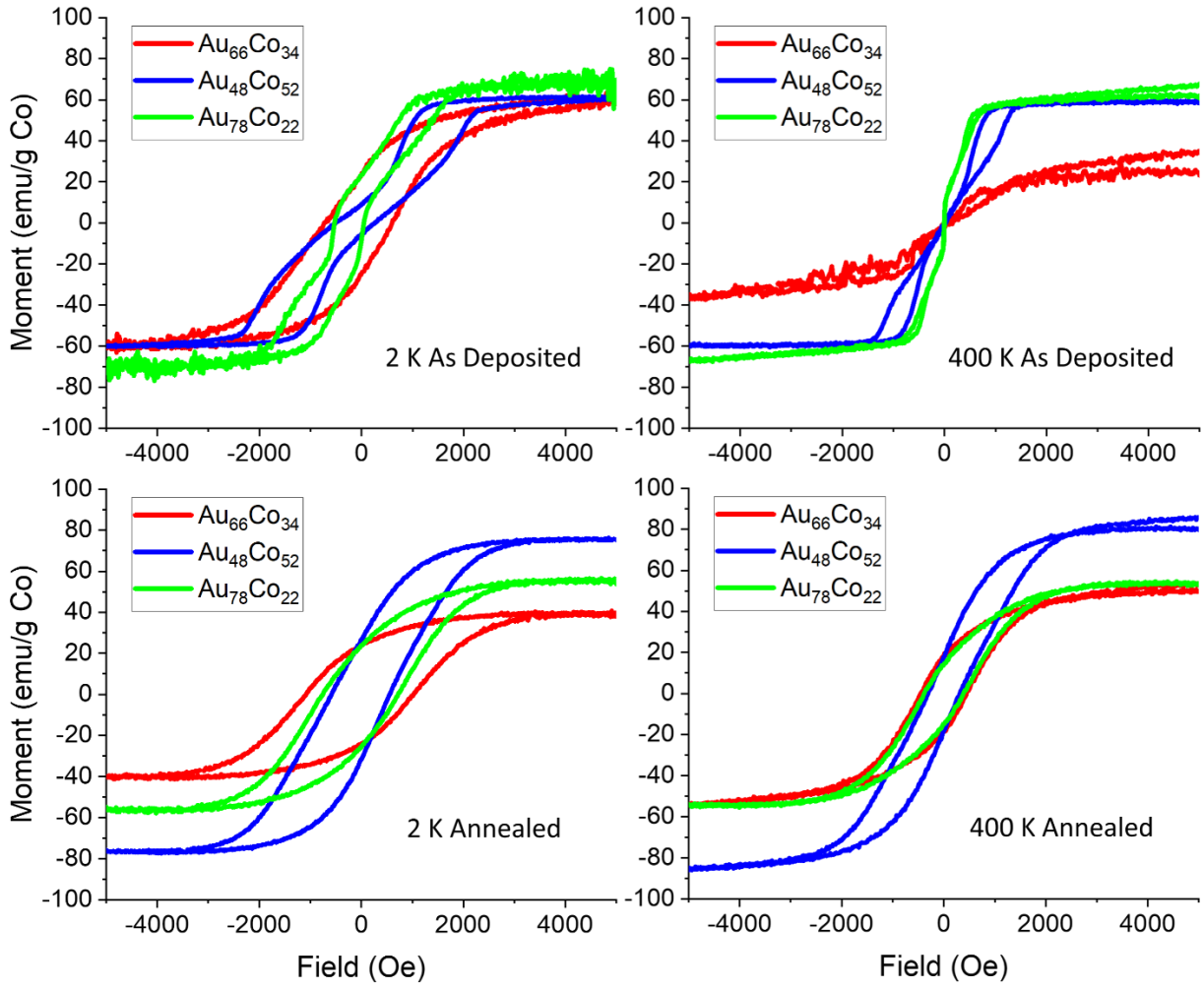

Figure 51:M vs. H plots of the nanoparticles at 2 K and 400 K as PLiD and following annealing

magnetization a full vortex is realized. This behavior is prevalent in all as laser treated nanoparticles at RT and disappears in the Au rich sample at 2 k. Additionally, this behavior disappears following the thermal anneal. The as laser treated nanoparticles are relatively homogenous throughout each individual nanoparticle, while the annealed samples have larege clusters of phase separated Au and Co. In the as laser treated nanoparticles domains can form around the circumference of the spheres, but after phase separation, the Au rich grains block this behavior.

The phase separation resulting from 20 minutes of annealing is sufficient to produce room temperature ferromagnetism in all samples, as seen in Figure 5. There is essentially no observable exchange bias at 300 K, and relatively minimal at 2 K, with the only noticeable trend being the asymmetry in the positive and negative lobes. There is a significant variation in the saturation magnetization in the most Co rich nanoparticles despite normalization to the Co mass, however the coercivity and retentivity remain nearly identical for all compositions.

Optical Properties

Ellipsometry

The optical properties of the as deposited and annealed $Au_{72}Co_{28}$, $Au_{50}Co_{50}$, and $Au_{28}Co_{72}$ thin films were measured via ellipsometry. These results, as well as reference data for Au[166] and Co[167], are included in Figure 52 as a function of photon energy. The characteristics of a strong plasmonic material, like Au, are a large $|\varepsilon_1|$ (Figure 52b), indicating the polarization induced by incident light at the surface of the material, and a small ε_2 (Figure 52c), which is correlated to the extinction coefficient, and thus indicates absorption within the material. A simple relationship $\left(-\frac{\varepsilon_1}{\varepsilon_2}\right)$, termed

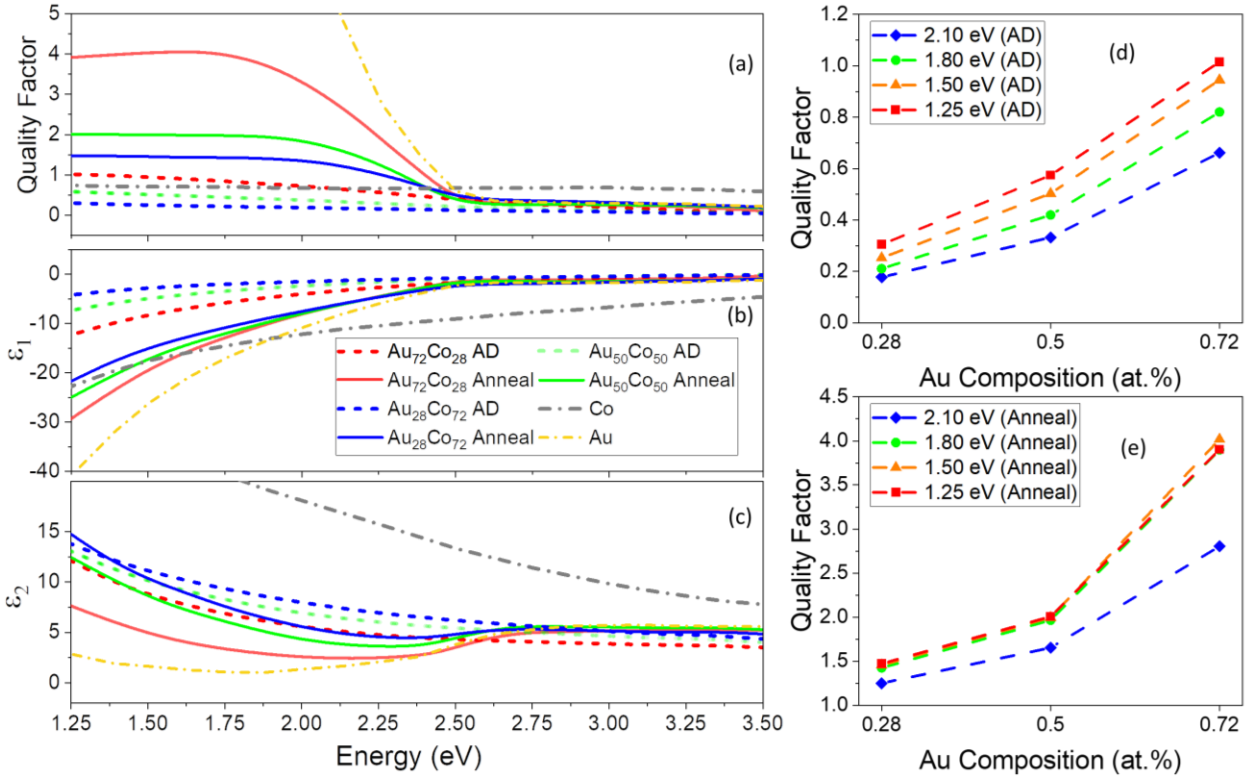

Figure 52: Ellipsometry results for the 60 nm Au72Co28, Au50Co50, and Au28Co72 films showing the quality factor (a), ε1 (b) and ε2 (c) as a function of photon energy (eV) for as-deposited and annealed samples. Also included is reference data for pure Au and Co. d and e) show the quality factor as a function of Au composition for the as deposited and annealed thin films at four different energies.

the localized surface plasmon resonance quality factor (Q_{LSPR}), can be used to express the viability of a material for plasmonic applications:this value is plotted in Figure 52a. Below the energy of the Au interband transition (~2.4 eV), Figure 52a demonstrates that the addition of Co, which possesses minimal plasmonic functionality, greatly reduces Q_{LSPR} compared to pure Au. This behavior is present in both the as deposited and annealed films, and scales with the composition of Co. There is, however, a clear difference in the behavior of the as deposited film and the annealed film. Whereas the as deposited film exhibits a behavior similar to pure Co, the phase separation induced through annealing, significantly enhances the quality factor of the Au_xCo_{1-x} thin films. Specifically, the $Au_{72}Co_{28}$ composition, suggests that small quantities of phase separated Co can be introduced into an Au matrix while maintaining strong, albeit damped from pure Au, optical properties in the visible and near infrared frequencies. Figure 52d and e exhibit Q_{LSPR} as a function of Au composition for the as deposited (d) and annealed films (e). The as deposited films show an incremental linear improvement in the Q_{LSPR}. Conversely, the annealed films show a steep increase from $Au_{50}Co_{50}$ to $Au_{72}Co_{28}$. Another difference in the as deposited and annealed films, is that the as deposited films show an incremental increase in Q_{LSPR} with decreasing photon energy. The annealed films, where Au is fully separated from the solid solution, on the other hand demonstrate a behavior very similar to Au, where Q_{LSPR} begins to decrease after a maximum value around 1.5 eV.

Nanoparticles

Transmission Spectroscopy

Optical transmission spectroscopy measurements were conducted on pure Au, $Au_{66}Co_{34}$, $Au_{48}Co_{52}$, and $Au_{22}Co_{78}$ nanoparticles prior to and after annealing, these results are plotted in Figure 53. Also, included in Figure 53 (e-h) are nanoparticle size distributions for each

composition. Whereas the particle distributions for the VSM samples were very consistent, here there is significant variation between the different compositions. The resonance energy of LSPR modes excited by the optical field are greatly influenced by the size of the nanoparticles, with reducing the size of nanoparticles producing a blue shift in the spectra. This trend continues until the lowest energy LSPR mode, the dipole, reaches a resonance energy at ~2.4 eV where interband transitions are reached.

Figure 53 a exhibits the optical properties of pure Au. The pure Au PLiD nanoparticles produce a sharp peak in absorption at ~2.1 eV. Annealing the Au nanoparticles results in a slight blue shift and a modest increase in intensity of the peak. Au nanoparticles smaller than ~50 nm possess a single resonance, termed the quasiplanar mode, that is nearly degenerate with the surface plasmon polariton energy[20], so it is reasonable that the predominance of nanoparticles in the 50-100 nm range (Figure 53a) results in a peak at 2.1 eV. This primary peak can thus be identified as the Au LSPR dipole mode. The other peak that is present at ~2.4 eV which likely be attributed to interband transitions.

In the as PLiD state where nanoparticles are homogenous Au_xCo_{1-x}, there is no clear LSPR absorption in the $Au_{48}Co_{52}$ and $Au_{22}Co_{78}$ samples, and only a weak and exceptionally broad peak in the $Au_{66}Co_{34}$ sample. The strength of the LSPR dipole modes are enhanced significantly through phase separation induced through annealing for 20 mins at 580°C, and then improved slightly beyond that with an additional 40 mins of annealing. Consistent with what was observed in Figure 52, and evidenced here by $Au_{66}Co_{34}$, the addition of small amounts of phase separated Co allows for a strong plasmonic response in Au_xCo_{1-x}. Beyond this point, the quality of the plasmon peak is significantly reduced with increasing Co. Both the $Au_{48}Co_{52}$, and $Au_{22}Co_{78}$ compositions possess only weak and very broad plasmon peaks even after annealing. It must be noted, however, that

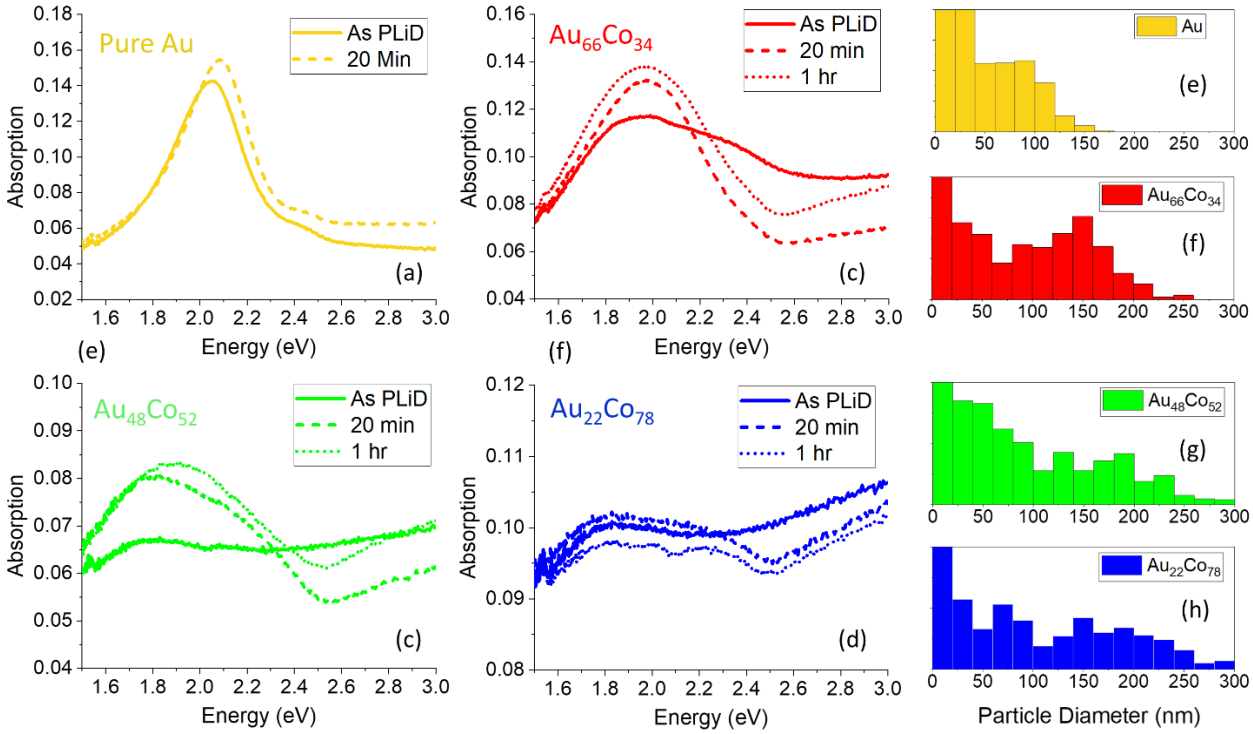

Figure 53: a, b, c, and d) optical transmission spectra of the four samples as PLiD and following annealing, e, f, and g, and h) particle diameter distribution of pure Au and Au64Co34, Au48Co52, and Au22Co78.

there is also a significant broadening from the variation in the nanoparticle size distributions at different compositions (Figure 53e-h). The $Au_{66}Co_{34}$ composition has the narrowest nanoparticle distribution with an average size of ~130 nm, again ignoring sizes below 50 nm. The increase in particle size compared to pure Au, leads to a red shift to 1.95 eV. The $Au_{48}Co_{52}$ sample has a wide particle distribution from about 240 nm down to 50 nm, this results in a very broad peak beginning at 1.75 eV. Finally, the $Au_{22}Co_{78}$ dipole mode is similarly broad with the presence of multiple peaks spanning a wide energy range due to the breath in breadth nanoparticle size distribution.

Electron Energy Loss Spectroscopy

While the results from Figure 53 illuminate the average behavior of a large collection of nanoparticles, electron energy loss spectroscopy (EELS) provides a tool to measure individual nanoparticles, and thus directly observe the influence of chemical morphology on optical properties. In Figure 54 three nanoparticles with different chemical morphologies, but very similar composition and size (~155 nm) are analyzed via EEL point spectra at selected points of interest and spectrum images of the overall nanoparticles. The point spectra shown in Figure 54 were fit to two Lorentzian functions corresponding to the LSPR dipole mode and the quasiplanar mode; energy positions of these fits were used to generate the energy filtering criteria in the spectrum images. The first nanoparticle (Figure 54a) was dewet via PLiD with no further heat treatment (directly comparable to the as PLiD plots in Figure 53). Here, there is a one predominant, exceptionally broad, peak (FWHM = 1.65 eV) at 1.64 eV which can be identified as the LSPR dipole mode. The spectrum image filtered to this energy, Figure 54, shows that this peak is uniformly distributed around the nanoparticle. The second, and much smaller, peak is associated with the quasiplanar mode and located at 2.72 eV.

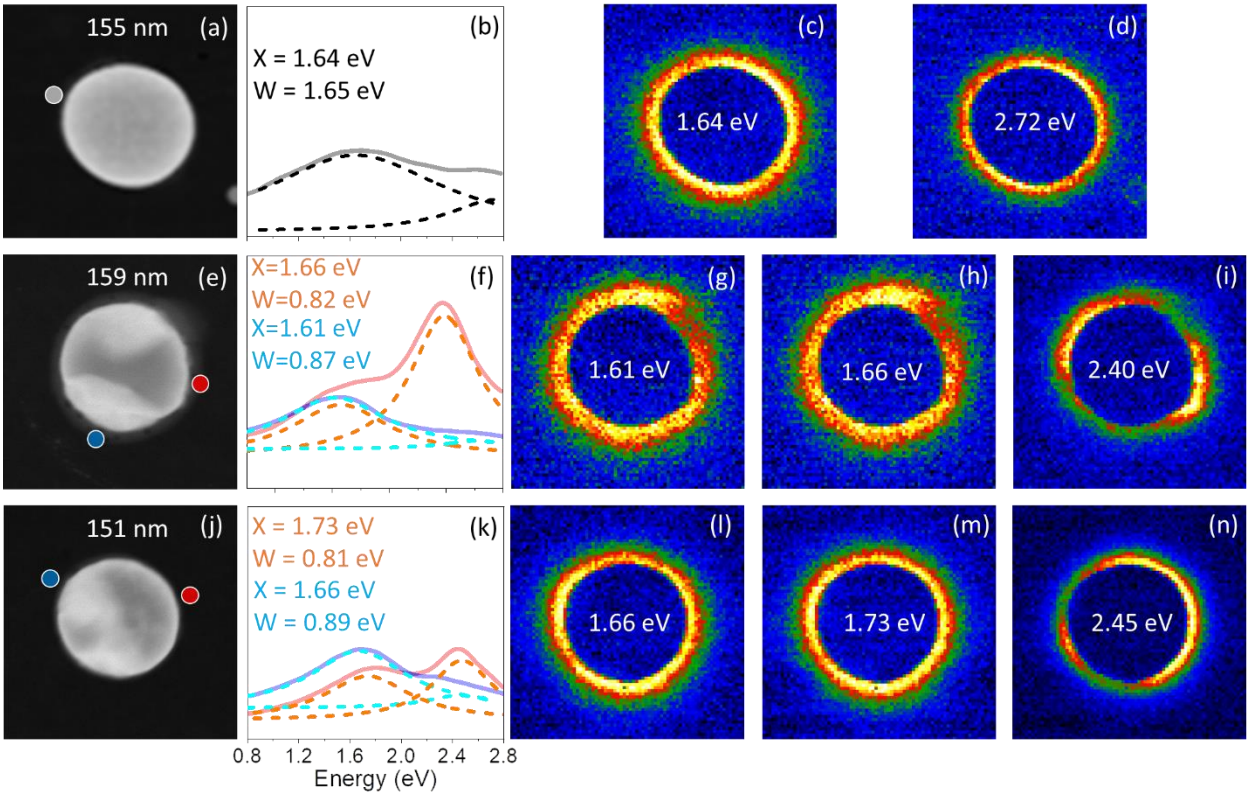

Figure 54: a, e, and j) show the HAADF STEM images of three AuxCo1-x nanoparticles, b, f, and k) show the point spectra at the positions indicated in a, e, and j, c-d, g-I, and l-n) spectrum images filtered to the energies indicated.

Nanoparticles in Figure 54e and Figure 54j were both laser treated, and then annealed at 450°C for 2 hrs, and are thus comparable to the 20 and 60 min anneal plots found in Figure 53. As is seen in Figure 49, there are a wide range of nanoparticle morphologies following annealing, and here two different morphologies have been selected. It must be noted that the contrast between the two phases is inverted in this figure, i.e. the darker contrast corresponds to Co, due to the transmission aspect of this measurement technique. The first annealed nanoparticle has two Co sides with an Au strip that reaches end to end. The other annealed nanoparticle found in Figure 54 is a near Janus particle with a slight Au rich area in the Co hemisphere. Both nanoparticles exhibit a similar behavior despite the variation in chemical morphology. A Co probe position results in a dominant peak (the LSPR dipole) and a significantly smaller higher energy peak. Probing an Au position results in a much larger higher energy peak (Au quasiplanar) in addition to the LSPR peak. An interesting, but subtle, variation in the probe positions, is a very small red shift when probing the Co side compared to the Au. Additionally, the intensity of the peak, as seen by the fitted point spectra and spectrum images is not greater on the Au side and is actually larger on the Co side. The shift in peak position when comparting the two annealed nanoparticles is likely due to the slight variation in size, although the chemical segregation behavior could also be contributing to this behavior. There are no obvious variations in the spectrum images at the Co and Au LSPR resonance energies (Figure 54g, h, l, and m). The highest energy spectrum images, associated with the quasiplanar mode, exhibit clear contrast that mirrors what is seen in the HAADF images for the annealed nanoparticles, due to pronounced phase separation. Conversely, this mode in as PLiD particle is uniform around the entire particle, consistent with the homogenous appearance. Finally, it must be noted that the resonance energies for the nanoparticles measured in EELS appear to be

red-shifted from the transmission measurements in Figure 7, this can be attributed to a slight variation in the substrate.

Conclusions

The chemical composition and morphology of Au_xCo_{1-x} thin films and nanoparticles can readily be controlled via a combination of co-sputtering, PLiD, and annealing, and demonstrate a large degree of tunability in magnetic and optical properties. The solid solution thin films can demonstrate superparagmetism with a sufficient Au content, while the demagnetizing behavior can be controlled by the grain structure and chemical composition. PLiD nanoparticles exhibit a wasp-waisted hysteresis behavior due to vortex generation, while after annealing large phase separated grains of Au and Co lead to a more traditional ferromagnetic behavior. The optical response of the Au_xCo_{1-x} nanostructures is also largely influenced by the chemical morphology. When the Au and Co are intermixed in the solid solution state, the optical properties of the thin films and nanoparticles are greatly reduced from that of pure Au. The phase separation of the Au and Co through annealing significantly improves the optical response in ellipsometry, optical transmission, and EELS. This improvement is enhanced with the reduction in Co composition despite EELS evidence that excitation of the Co portions of a nanoparticle provides a similar, if not augmented LSPR resonance. Excitation of the Co does lead to an LSPR mode that is slightly red shifted from the Au LSPR mode which could explain some of the broadening behavior.

Methods

Radio Frequency Magnetron Sputtering

Two pure (Au and Co) sputtering targets were sputtered simultaneously with the substrate rotating (no compositional gradient) and with the substrate stationary (chemical gradient from one target

to the other) depending on experimental requirements. A base pressure of less than 3E-7 Torre, sputtering pressure of 5E-3 Torre, and Ar flow of 25 sccm was used for all samples. For combinatorial (no rotation) samples a bias of 20 W for Au and 200 W for Co resulted in a center composition of $Au_{50}Co_{50}$. These conditions resulted in a deposition rate of 2 nm/min, measured via profilometry. The 10 nm co-sputter films were achieved with Au sputtering powers (W) of 11, 20, and 20, and a Co bias of 200, 200, and 70 for the $Au_{22}Co_{78}$, $Au_{48}Co_{52}$, and $Au_{66}Co_{34}$ compositions. Each film was measured as 10 $\pm$ 1 nm with a profilometer. A substrate of 500 μm Si with a coating of 100 nm SiO_2 was used for all samples other than those used for transmission spectroscopy. For transmission, thin 40 nm 150 x 150 μm SiN_x membranes supported by a 300 μm thick Si frame were used.

Annealing

Annealing was conducted in vacuum (<10 mTorre). Annealing times and temperatures varied by experiments as listed in the text.

Scanning Electron Microscopy and Energy dispersive X-ray spectroscopy

Energy dispersive x-ray spectroscopy (EDX) and scanning electron microscopy (SEM) were conducted on a Carl Zeiss MERLIN SEM. The initial ~400 nm combinatorially sputtered Au_xCo_{1-x} thin film (as deposited and annealed) was characterized at five points separated by 20 mm along the composition gradient. For EDX, an accelerating voltage of 20 kV. The second combinatorically sputtered thin film (~60 nm) and the co-sputtered films were characterized with the same parameters. In addition to large area spectra used to determine chemical composition, spatial EDX maps were also collected to observe the nanoscale chemical morphology. Particle size distributions in the PLiD samples and grain size in the thin films were determined with SEM images, and the built-in particle analysis plugin in ImageJ.

X-Ray Diffraction

X-Ray Diffraction patterns were measured using a Malvern Panalytical Empyrean diffractometer. A 2theta-omega scan with an omega offset of -4.5° was run with a Cu tube (0.154 nm) with an angle sweep from 30° to 110°. Measurements were taken approximately coincident to where the five EDX scans were performed across both the as-deposited and annealed sample. The $Au_{50}Co_{50}$ as PLiD and annealed samples were characterized with the same parameters.

Ellipsometry

A JA Woollam M-2000U ellipsometer was used to measure ε_1 and ε_2 as a function of wavelength. A spot size of approximately 1 cm x 1 mm. The approximate thickness of each sample was 60 nm, which was sufficient to avoid substrate effects. The raw data was fit using an effective medium approximation (EMA) model in which the composition of each component was estimated using the EDS data. The two metal components were then fit using a spline model.

Vibrating Sample Magnetometry

A vibrating sample magnetometer (VSM) on a PPMS DynaCool was used to obtain the magnetic properties of AuCo. The measurement time per point was 2 s. The magnetic hysteresis loop of the sample was conducted from -5000 Oe to 5000 Oe at temperatures in the range of 2 K to 400 K for the thin film samples, and at 2 K and 300 K for the nanoparticle samples. The sample size was ~4 mm vs 4 mm, and the mass normalization was conducted by measuring each sample, subtracting the substrate and then using composition from EDX and thickness from profilometry to determine the Co mass.

Pulsed Laser Induced Dewetting (PLiD)

Photothermal heating was conducted using a 248 nm KrF excimer laser. Experiments were conducted in a pulsed mode using a $1/e^2$ Gaussian pulse width of 18 ns and a top hat spatial

distribution. The PLiD samples on thick Si (VSM) were shot with five laser pulses with a fluence of 140 mJ/cm^2. A single pulse with a fluence of 40 mJ/cm^2 was used for the samples supported by the SiN_x membrane (transmission).

Thermal Finite Element Modeling

In order to approximate the photothermal heating of the Au_xCo_{1-x} films, a thermal finite element model (FEM) was utilized. Here, a heat source was applied at the Au_xCo_{1-x} surface (z = 0 nm), in the same manner as[168,169]. The governing equation for the heat flow is listed below:

$$\rho C_p \frac{dT}{dt} = \nabla \cdot (k\nabla T) + Q(x,y,z)$$

$$Q(x,y,z) = \frac{2\alpha}{\pi w^2} P(1-R)G(t)exp(-\alpha z)$$

The terms α and R indicate the absorption coefficient and the reflectivity, respectively, which were determined from the ellipsometry measurements for different compositions. The value w is the full-width of the laser beam at 1/e^2 of the maximum fluence. The laser fluence is demonstrated as P. G(t) represents the temporal Gaussian of the KrF laser. The edges of the suspended membrane were assigned a boundary condition of room temperature to approximate the thick Si frame. The samples heated on thick Si did not require a boundary condition. The material properties were assumed to be constant, and thermal effects of phase transitions were ignored.

Transmission Spectroscopy

Optical transmission spectroscopy was conducted on the as deposited and annealed PLiD samples. A 1 mm aperture was for all measurements, and photon energies from 1.5 eV to 3 eV are included.

Electron Energy Loss Spectroscopy

A Nion aberration-corrected high energy resolution monochromated EELS-STEM (HERMES) operated at an accelerating voltage of 60 kV was used to obtain the spectra and spectrum images.

The convergence and collection semiangles used for the spectrum acquisition were 30 and 15 mrad, respectively. The energy resolution (full width at half-maximum of the zero-loss peak) was approximately 20 meV. The EEL spectra presented in were normalized to the zero-loss peak.

CHAPTER IV
ELECTRIC AND MAGNETIC FIELD COUPLING IN PLASMONIC META-ATOMS VISUALIZED VIA STIMULATED ELECTRON GAIN SPECTROSCOPY

Electric and magnetic field coupling in plasmonic meta-atoms visualized via stimulated electron energy gain spectroscopy

David A. Garfinkel[1], Vasudevan Iyer[2], Robyn Collette[1], Grace Pakeltis[1], Benjamin Lawrie[2], Philip D. Rack[1,2]

1. Department of Materials Science and Engineering, University of Tennessee, Knoxville, Tennessee 37996, United States

2. Center for Nanophase Materials Sciences, Oak Ridge National Laboratory, Oak Ridge, Tennessee 37831, United States

Authors Contribution

The author led all sample fabrication via electron beam lithography, in house transmission electron microscope sample synthesis, and sputtering. All electron energy loss and electron energy gain spectroscopy done on the Zeiss Libra 200 was conducted by the author. The author was also responsible for all writing, data processing, analysis, and generation of figures, including all peak fitting. Collaborator Grace Pakeltis performed the electron energy loss spectroscopy that is included in Figure 56. All computational theory figures were provided via the David Masiello group at the University of Washington.

Introduction

The quest for high frequency magnetic materials has led to miniaturization of plasmonic meta-atom architectures. While standard split ring resonator (SRR) geometries are useful meta-atoms for extension to infrared frequencies[95,170], lithographic constraints make optical frequencies challenging[171–173]. Thus, coupled ring-like arrangements of nanospheres[174–176], nanodisks[177,178] and nanorods[179–181], referred to as oligomers, have made it possible to extend magnetic modes to higher frequencies. Oligomers with *n* number of nanoparticles or nanorods hybridize into various localized surface plasmon resonance (LSPR) modes, where the number of modes increases with *n.* The configuration with all individual longitudinal dipoles orientated head to tail is the lowest

energy mode and the resultant circulating current induced by the hybridized dipoles creates a magnetic field normal to the closed loop. At higher energies, the individual dipoles arrange into different configurations, including those with a net electric dipole. The energy splitting between these modes is dependent on the individual mer length, spacing and n[100].

Several groups have studied the optical and magnetic resonances of nanoparticle ring structures [see[176] for review]. Alu et al[182] showed theoretically that rings of silver nanoparticles exhibit negative permeability and permittivity at optical frequencies where n, nanoparticle size and spacing, as well as the surrounding medium index of refraction all affect the resonance frequency. Experimentally, gold nanoshell particles were self-assembled and the electric and magnetic dipole of an n=3 nanoparticle cluster was revealed with p-polarization and s-polarization scattering measurements, respectively[183]. An atomic force microscope manipulation method was also used to direct the assembly of an n=4 ring of gold nanoparticles, and oblique angle scattering measurements with mixed s- and p-polarization induced both an electric and magnetic dipole[184]. Furthermore, slight geometric asymmetries were shown to enhance the magnetic dipole and lead to a Fano dip in the scattering spectra. More recently, Moritz and Simovsky[185] showed that nanoparticle "dimers" that effectively prolate the sphere geometry enhanced the negative permittivity and permeability of n=4 oligomers. Finally, the electric and magnetic dipoles of equilateral trimers of gold nanords were also studied, and s-polarized excitation clearly revealed both the electric and magnetic modes[180]. Again, slight geometric asymmetries in the structures enhances the magnetic dipole and can induce a Fano interference between the bright electric mode and the dark magnetic mode.

Electron energy loss spectroscopy (EELS) is a powerful tool as a high-resolution near-field probe, and has been used extensively to investigate various plasmonic phenomena [see[186] and[187] for recent

reviews]. The EELS spectrum image of the hybridized in phase (bonding) and out of phase (antibonding) modes have different signatures, so the combined spectrum and spectrum imaging can be used to unequivocally distinguish these modes. Specifically, the bonding vertices are more localized to the rod ends, whereas the antibonding modes exhibit a bright gap. Relevant to nanomagenetic plasmonic meta-atoms, von Cube et al. have studied individual[95,188] and coupled[96,189] split ring resonators. They realized infrared (1.25 eV) electric/magnetic dipole mode in gold SRRs with edge lengths down to 120 nm. The dispersion of gold surface plasmons and nanoscale synthesis limitations make it challenging to extend gold SRRS to optical frequencies. EELS of silver nanorod equilateral triangles were recently studied and the electric and magnetic dipole modes were determined to hybridize with ~0.25 eV splitting[179].

To extend the capability of EELS, we have recently integrated an optical delivery system to a scanning transmission electron microscope equipped with a monochromated electron source and EELS detector. The laser delivery system is capable of photothermally heating the sample for *in situ* and so-called rapid *ex situ* imaging[121], and also photo-exciting the sample to allow for photoinduced near-field imaging/spectroscopy of materials in a conventional microscope. For instance, we have demonstrated continuous wave (cw) stimulated EEL (sEEL) and stimulated EE gain (sEEG) signatures in silver nanostructures[190], and have characterized the longitudinal m=1,2,3 LSPR modes of gold nanorods[7] as well as coupled dimers[8]. While ultrafast time-resolved photo induced near-field electron microscopy has been developed[191–194] and has elucidated interesting plasmonic[195,196] and biological processes[197], the cw excitation of materials in a conventional microscope is useful for revealing many excited state phenomena. In traditional EELS, all excitations of plasmonic modes are excited via spontaneous near field interactions with the electron beam. Each individual event results in a loss of energy from the electron, and thus the

characteristic peaks occur on the loss side of the zero loss peak. With simultaneous photoexcitation, plasmonic modes can be driven via photoexcitation, and thus incident electrons can either gain or lose energy during near field interactions. This leads to both a stimulated electron energy gain (sEEG) and stimulated electron energy loss (sEEL) peak at the energy of the optical source.

Here we use sEEGS and to map the near field of the in-phase magnetic dipole mode and the out-of-phase electric dipole mode of a simple plasmonic trimer structure. The lowest energy mode consists of the three longitudinal dipoles arranged in a head-to-tail configuration, leading to a circulating current Figure 55b. In the remainder of the text, we will refer to this lowest energy mode as the magnetic mode due to the induced magnetic field Figure 55c. In the coupled trimer the other observable mode, which will be termed as the electric mode, is composed of two rods coupling out-of-phase at a vertex, and the remaining rod exhibiting weak coupling Figure 55c. To directly image the electric and magnetic modes of the trimer meta-atom, we vary the rod length to tune the magnetic and electric modes to the laser energy (1.58 eV). The trimer structure designed to align the magnetic mode with the laser energy will be referred to as the magnetic structure, while trimer tuned to the electric mode, will be referred to as the electric structure. Thus, for the first time, we have imaged the near-field of a photoinduced magnetic and electric dipole in a plasmonic meta-atom using sEEG.

Results

Figure 55a schematically illustrates our experimental setup for sEEGS. Note that the electron beam (dotted line in Figure 55a) and laser are fixed at a 90° angle relative to one another, so the sample must be tilted to focus both beams to the same field of view. Figure 55f and i show two extreme tilt angles (θ) to demonstrate the influence of tilt angle on coupling between the trimers

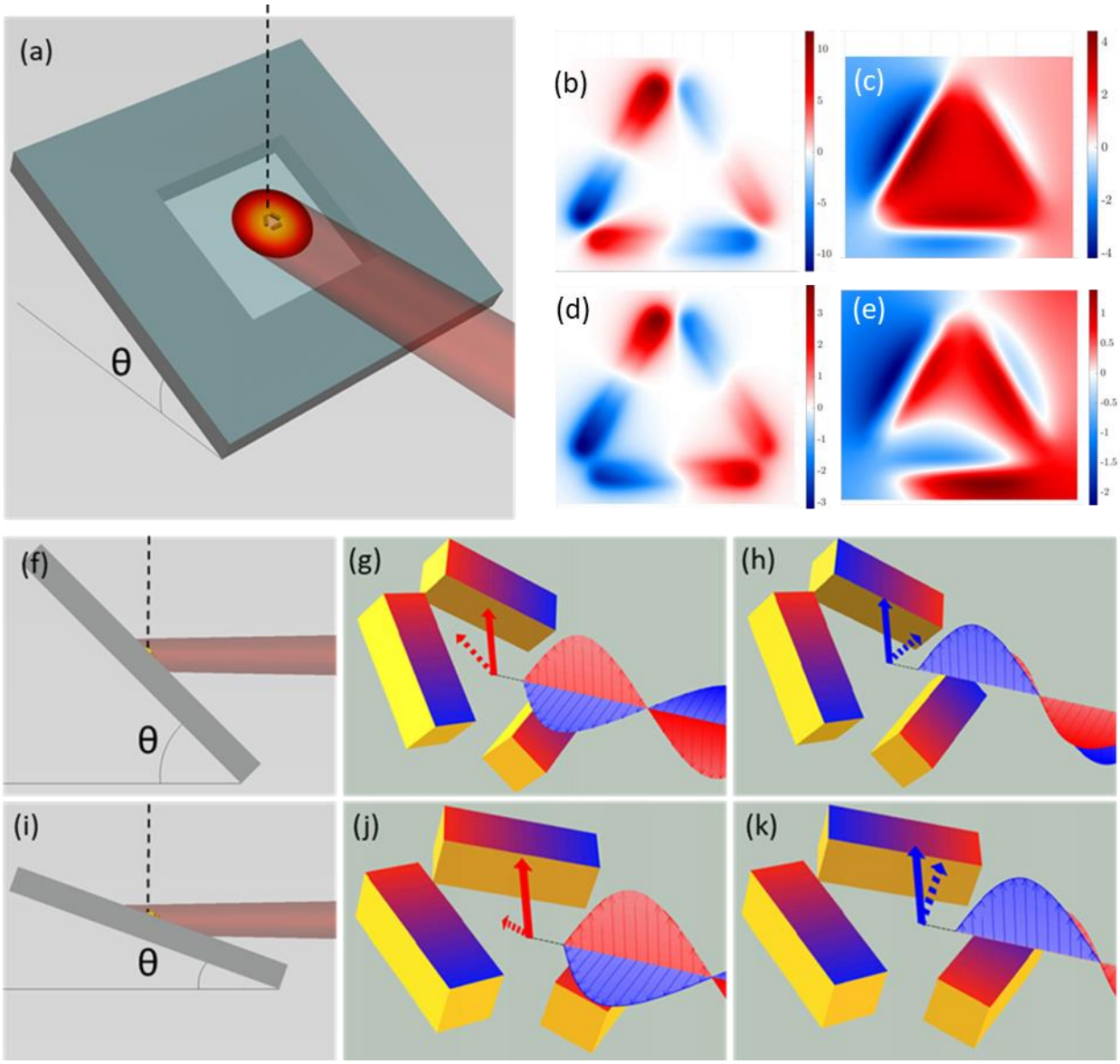

Figure 55: Schematic of the sEEGS experimental setup (a). (b-e) Simulations demonstrating the electric (b and d) and magnetic (c and e) corresponding to the magnetic (b and c) and electric (d and e) trimer modes. Theta indicates the sample tilt from normal to the electron beam (shown as dotted line, f-k) show the influence of sample tilt on the optical coupling of the electric (g and j) and magnetic (h and k) modes. Red arrows are used to show the electric field for the electric mode, while blue is used for the magnetic component to the magnetic structure. Dotted arrows indicate the projection of the electric and magnetic components onto the plane that it is operative.

and the laser. With this experimental setup, θ is typically constrained to a range of about ~20°-35° due to interference from the silicon membrane frame at large angles and difficulty aligning the laser at lower angles. Figure 55h and j illustrate that coupling between the electric mode and the laser are maximized (the magnitude of the projected component, illustrated as a red dotted line) when θ increases. For the magnetic mode (h and k), its magnetic dipole is oriented normal to the structure, and because of that, increasing the tilt angle reduces the coupling strength of the magnetic component of the optical field (shown by the dotted blue line). Thus, by modifying the tilt angle the relative coupling strength of each mode should move in opposite directions.

Prior to performing excited state spectroscopy on the trimers, a separate instrument was used to obtain higher resolution (18 meV FWHM) EELS data on a sample trimer structure. Figure 56 demonstrates the hybridization of the three rods into two distinct modes through point spectra (a) and spectrum images (b-e). As illustrated by the high angle annular dark field (HAADF) inset, the point spectra were taken at two positions, in between the two rods at the vertex (gap), and at the end of one of the rods (tip). At the tip position, both the magnetic (1.58 eV) and the electric (1.85 eV) modes are excited; conversely, in the gap the magnetic mode is greatly reduced. The spectrum images of the full structures (b and c), as well as the magnified top vertex (d and e) clearly reinforce the observations from the point spectra. Whereas the electric mode has a high intensity at the gap, the magnetic mode has a defining nodal line in the gap center where excitation is zero as a single electron cannot simultaneously excite out-of-phase dipoles in the two adjacent rods.

Trimers with rod lengths of ~175 nm were synthesized to efficiently tune the electric dipole mode to our 1.58 eV laser. Figure 57a shows a bright field TEM image of the selected electric structure. The associated EELS spectrum images without laser irradiance at the magnetic mode (1.35 eV) and electric mode (1.62 eV) are included in Figure 57b and c, respectively. Figure 57d and e are

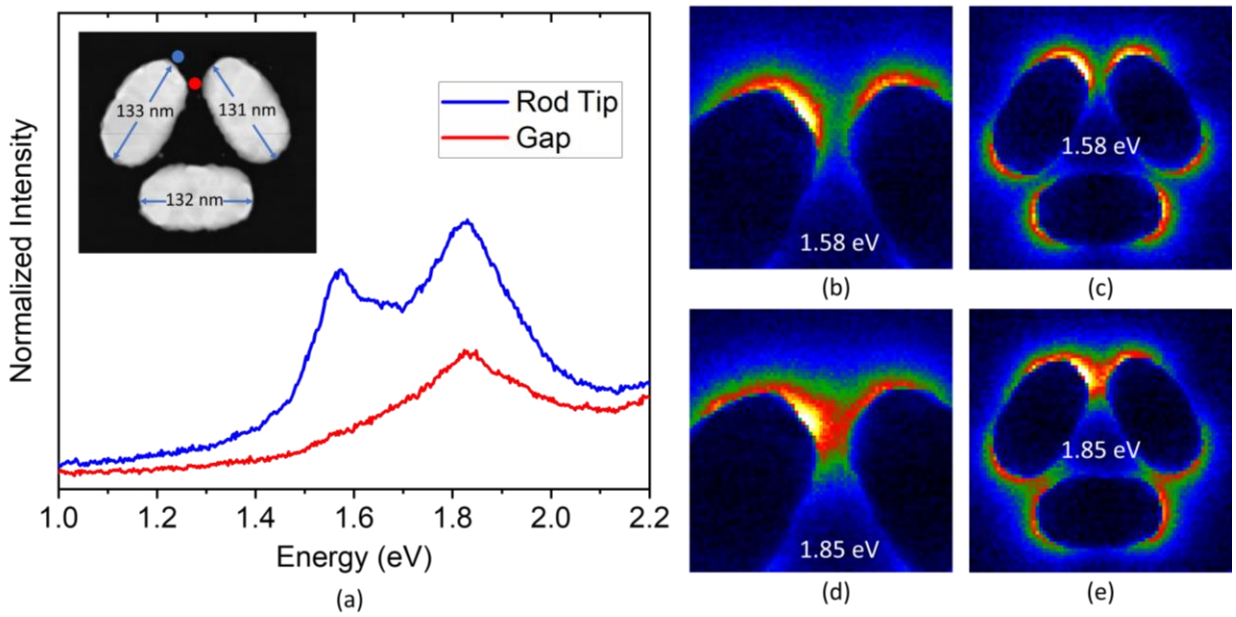

Figure 56: a) high resolution point spectra at an edge and gap location. b-c) spectrum images of the whole trimer with the magnetic mode at 1.58 eV (b) and electric mode at 1.85 (c). d-e) spectrum images of the top vertex showing the magnetic and electric modes at energies of 1.58 and 1.85 eV, respectively.

higher resolution images of the top vertex at the same two energies; the selected area relative to the complete structure is illustrated in Figure 57a. The overall trends observed in Figure 56, namely the variation in the signatures between the two modes, are consistent with what is observed in Figure 57a-e. The primary deviation being greater asymmetry in the magnetic mode of the trimer characterized in Figure 57. Here, the left rod in the top vertex (seen in both b and d) has a greater intensity in the magnetic mode than the remainder of the structure. Conversely, the excitation of the electric mode appears to be slightly higher near the right rod, though this result is subtle.

In the sEEGS experimental setup, the top vertex is the farthest point from the laser, which typically leads to maximized sEEGS signal. For this reason, higher resolution sEEGS experiments were measured at the top vertex of the trimers. Specifically, spectrum images of the vertex (Figure 57f and g), and point spectra at a gap and tip aloof position (Figure 57h and i) were collected at tilt angles of 20° and 32° with a laser irradiance of 1.3E5 W/cm^2. Spectrum images filtered at -1.58 eV with the structure tilted at 20^o (Figure 57f) and 32^o (Figure 57g) demonstrate the tilt sensitivity of sEEGS. At 20^o the intensity from the sEEG peak is low and not discernible above the noise level, and thus no clear behavior can be surmised. When the sample tilt is increased to 32^o, the electric field component of the optical field increases, and the sEEGS signature increases. Peak intensities are observed near the rod tips, with a maximum near the right rod which is consistent with the elevated EELS intensity at the same rod tip without laser irradiance (Figure 57e). Figure 3 h and i show EELS spectra taken at zero tilt (no laser), as well as at 20^o and 32^o tilt with the laser on. An aloof position in the gap is shown in Figure 57h, while an aloof position at the rod tip is shown in Figure 57i. The sEEG (dotted), magnetic (short dash), and electric (long dash) peak positions are indicated. The increased collection time associated with point spectra compared to spectrum images results in a peak at -1.58 eV for both tilt conditions and both aloof positions,

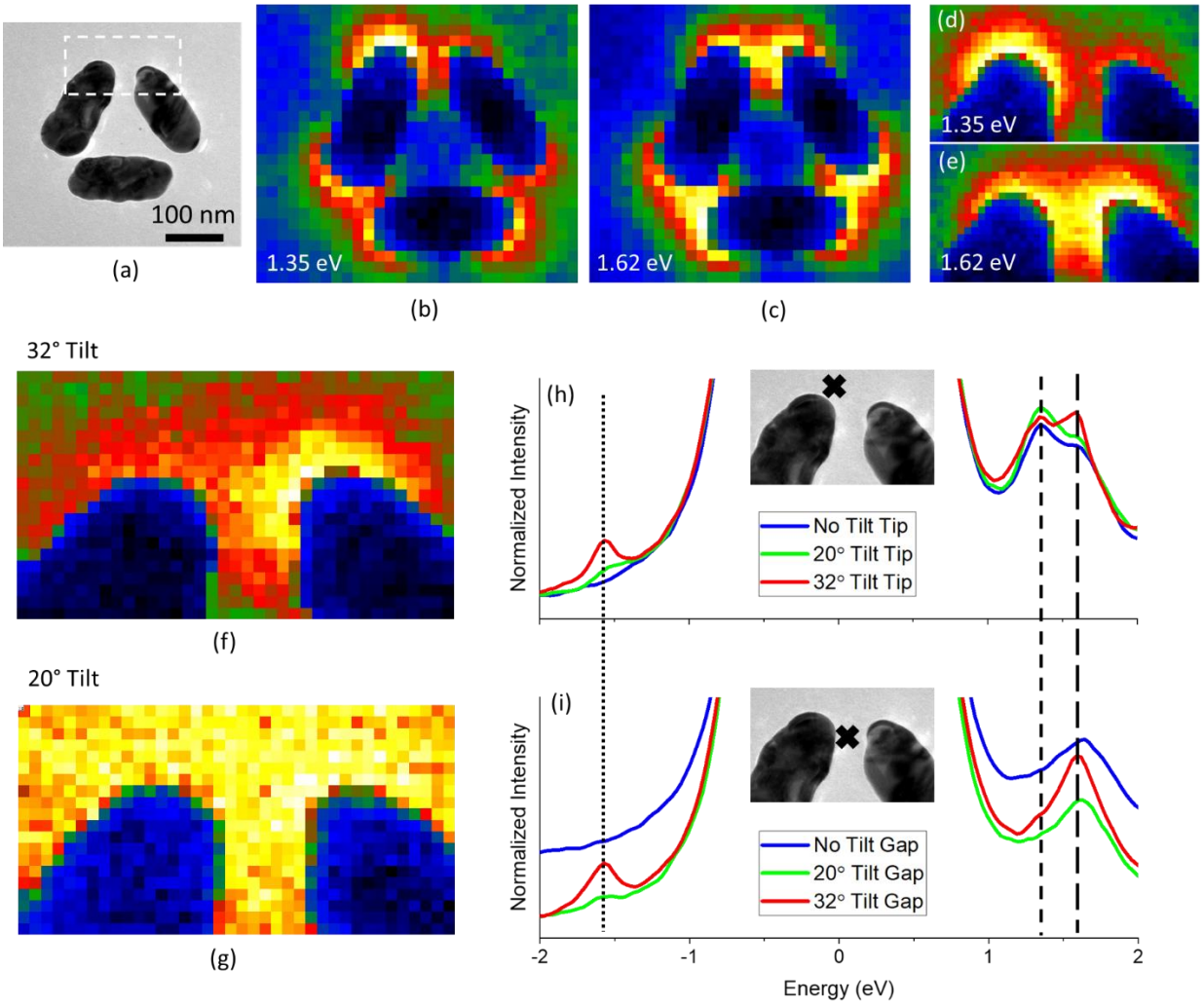

Figure 57: a) TEM bright field image of a trimer that hybridizes with the electric dipole resonant near the laser energy. The measured rod lengths are ~175 nm. b-c) spectrum images of the magnetic (1.33 eV) and electric (1.64) dipole modes. d-e) high resolution spectrum image of the top vertex from b and c. f-g) sEEGs spectrum images of the vertex in d and e at -1.58 eV with laser on at 20 and 32° tilt. h-i) point spectra of the trimer at no tilt with no laser irradiance, and laser on with 20° tilt and 32° tilt taken at the rod tip (h) and the gap (i).

indicating coupling to the laser. The gain behavior is strikingly similar in the two aloof positions: there is a clear increase, of similar magnitude in sEEG intensity with increasing the tilt angle. The loss behavior, however, is quite different, and consistent with what is observed in Figure 56a: the ratio of the electric mode to magnetic mode is much greater in the gap than at the tip. The lack of sensitivity in the sEEGS peak to the magnetic mode suggests that there is minimal contribution from the detuned magnetic mode (ΔE = 0.23 eV from laser energy) in the electric structure.

The magnetic mode was tuned to the laser energy via patterning trimers with slightly reduced rod lengths of ~140 nm. Similar to Figure 57, Figure 58 shows a bright field TEM image (a) and associated spectrum images of the complete trimer (b and c) and the top vertex (d and e) at the magnetic mode (1.64 eV) and electric mode (1.89 eV) energy with no laser irradiance. The behavior of this trimer is very similar to that of the electric structure; however, the energy splitting between the two modes is reduced (0.2 eV compared to 0.27 eV), and the magnetic structure exhibits a more symmetric spectrum image at the top vertex, where the two modes are nearly identical at the left and right rods.

Similar sEEGS measurements as taken for the electric structure from Figure 57f-j are presented in Figure 58 for the magnetic structure: the sample was tilted to 20^{o} and 32^{o} with a laser irradiance of 1.3E5 W/cm^{2}. Optical field interactions in the magnetic structure are decidedly different from the electric structure. At both tilt conditions, the sEEGS spectrum images, Figure 58f and g, show obvious indications of coupling. The signature is more localized to the left rod, though the peak is elevated at the right rod as well. At 20^{o} the intensity is more localized to the left rod than at 32^{o}, where the gap and surrounding area exhibit an increase in intensity. Contrary to what was observed in the electric structure, the two spectra from the aloof positions are different; namely the magnetic mode does not exhibit a significant tilt dependence. Further, there is a significant difference in

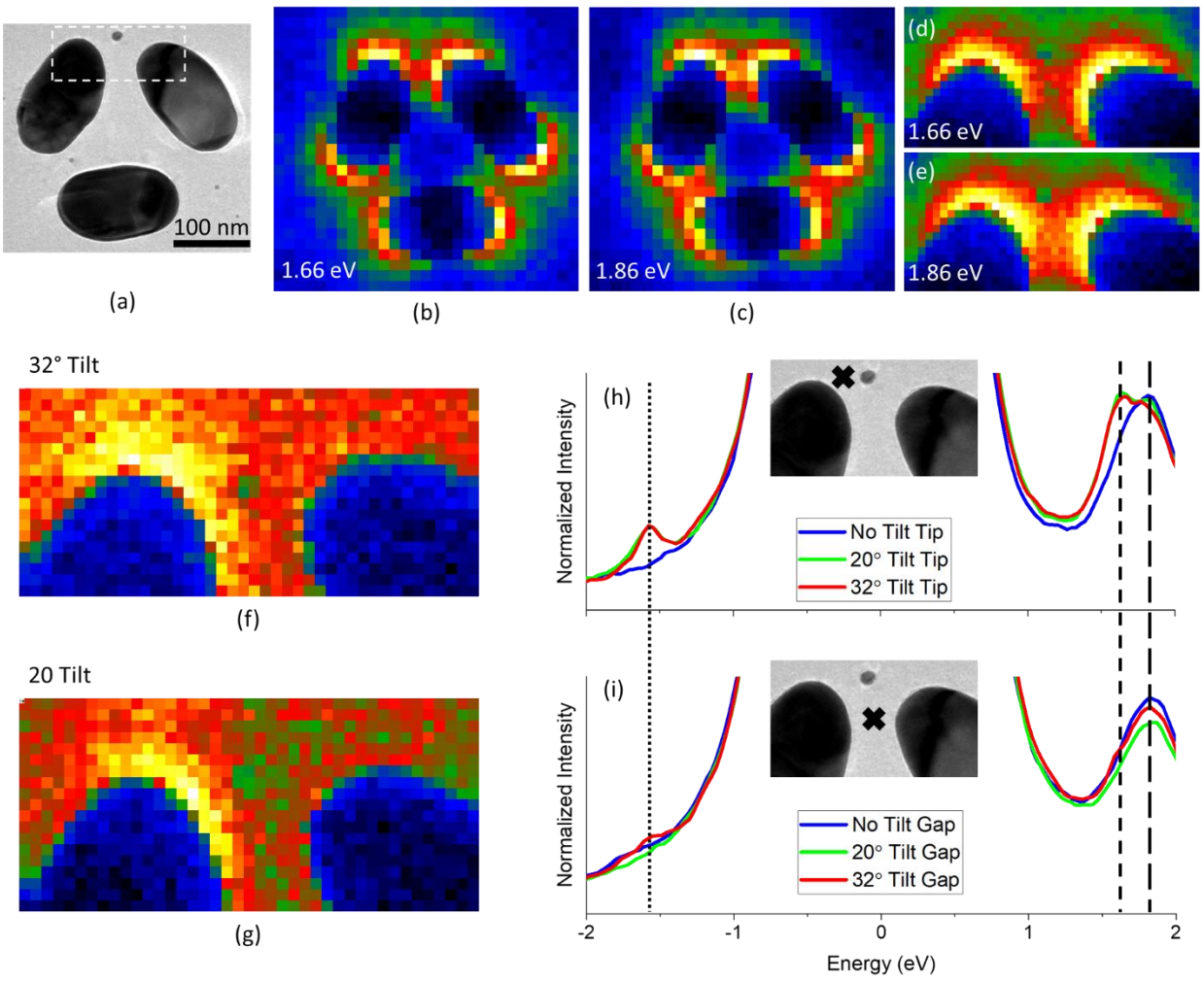

Figure 58: a) TEM bright field image of a trimer that hybridizes with the magnetic dipole resonant near the laser energy. The measured rod lengths are ~140 nm. b-c) spectrum images of the magnetic (1.66 eV) and electric (1.86) dipole modes. d-e) high resolution spectrum image of the top vertex from b and c. f-g) sEEGs spectrum images of the vertex in d and e at -1.58 eV with laser on at 20 and 32° tilt. h-i) point spectra of the trimer at no tilt with no laser irradiance, and laser on with 20° tilt and 32° tilt taken at the rod tip (h) and the gap (i).

magnitude of the sEEGS peak at the tip compared to the gap. As expected from the in-phase coupling of the magnetic mode, the sEEG intensity at the tip is much greater than that of the gap position. Similarly, when comparing the loss behavior, the magnetic mode is much stronger compared to the electric mode at the tip, thus in this structure, where the laser tuned to the magnetic mode, the sEEGS intensity scales with the magnetic mode spontaneous EELS intensity.

To improve interpretation of the results from the point spectra exhibited in Figure 57h-f and Figure 58h-f, the raw data were fit to deconvolve the spectra and better elucidate isolated peaks. It should be noted that the sEELS peak was subtracted from the data prior to fitting the spontaneous magnetic and electric loss peaks. Further information on the data fitting can be found in SI. Additionally, complimentary data from intermediate tilt angles (25° and 30°) are included. Figure 59a-d show the fitted Lorentzian functions associated with the magnetic and electric mode as well as sEEGS peaks for the tip and gap position for both the magnetic (Figure 59a-b) and electric (Figure 59c-d) trimer structures. Bright field TEM images with the aloof positions from Figure 57 and Figure 58 are included as insets to indicate the structure and probe positions. Though there is some variation, the magnetic and electric peak intensities remain relatively consistent regardless of tilt for each individual structure, with the 30° tilt measurement on the electric structure at the tip position being the most significant outlier (electric peak is larger than at other tilts). Focusing on the sEEGS peak, in the electric structure (c and d) there is a clear trend of increasing sEEGS intensity with increasing tilt angle for both aloof positions. This is consistent with what was observed in Figure 57 and agrees with enhanced coupling of the electric field component of the optical field to the electric trimer structure. In the magnetic structure, and consistent with the in-phase mode, the sEEGS intensity is much stronger at the tip compared to the gap, and neither mode demonstrates the same degree of tilt dependance (consistent with Figure 58). The tip position

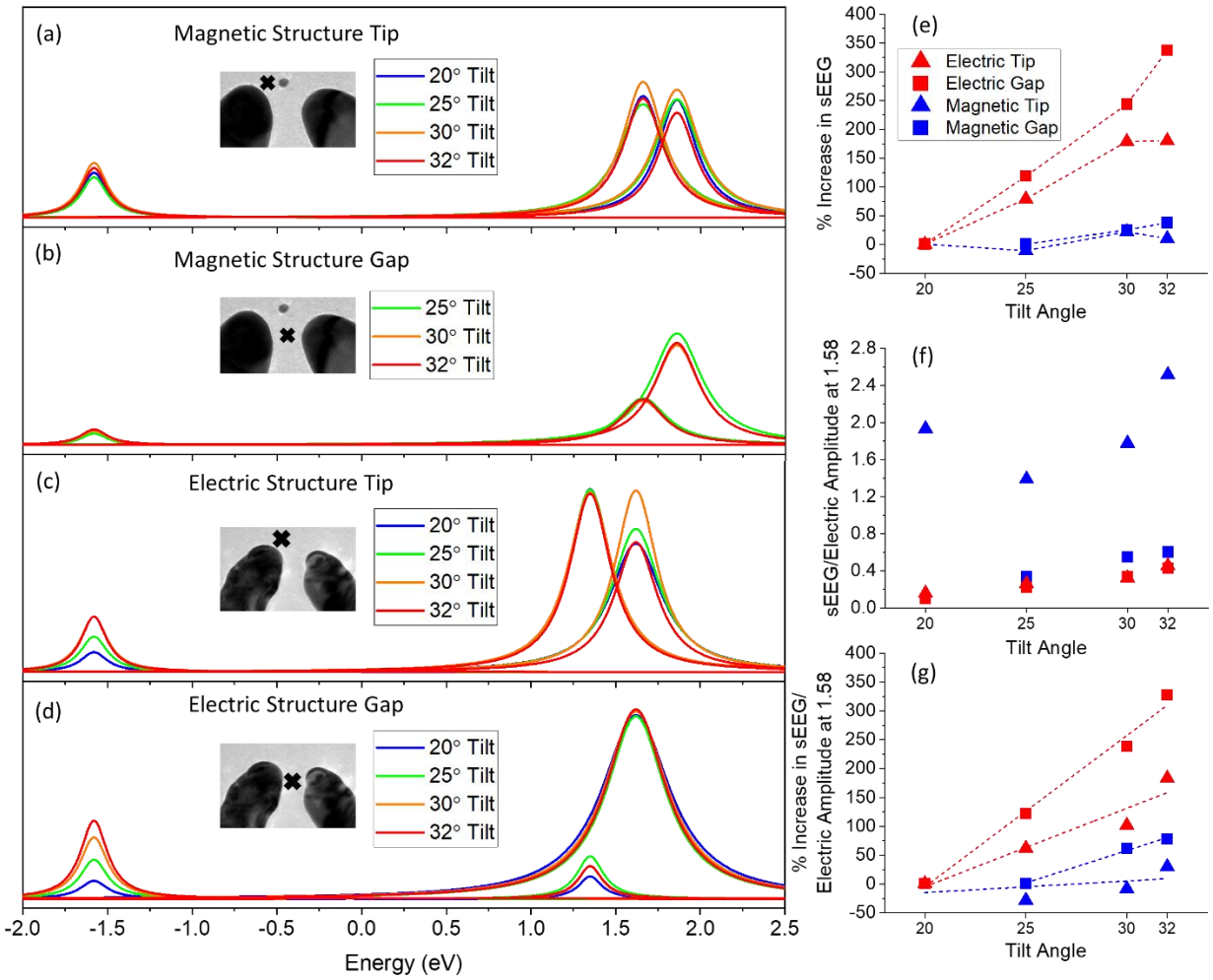

Figure 59: a-d) fitted magnetic and electric loss peaks as well as sEEGS peak for the magnetic structure at the tip (a), magnetic structure in the gap (b), electric structure at the tip (c), and electric structure in the gap (d). e) plot of percentage increase in sEEGS intensity as a function of tilt angle (normalized to the lowest tilt measurement), f) sEEGS peak normalized to the value of the electric peak at the laser energy (1.58eV) as a function of tilt, and g) percentage increase in sEEGS normalized the electric peak as was done in (f).

specifically fluctuates only modestly up and down with tilt. It should be noted that the gap position for the 20° magnetic structure did not produce a sEEGS peak sufficient for data fitting, so it is omitted.

The percentage increase in the sEEGS peak intensity (normalized to the lowest tilt measured) as a function of tilt is included in Figure 59e. Both probe positions for the electric structure show very strong tilt dependence, with the gap position possessing a slightly larger rate of change. The tilt dependence is much weaker in the magnetic structure. To compare the relationship between the sEEGS peak and the electric mode, Figure 59f exhibits the tilt dependence of the sEEGS peak normalized to the intensity of the fitted electric mode at 1.58 eV. The coupling efficiency (magnitude of y axis) of the two probe positions in the electric structure is similar and both increase with increasing tilt. The gap position of the magnetic mode also increases with tilt, and is slightly higher on the plot, indicating that when simply considering coupling to the tail of the electric mode, the coupling efficiency must be slightly greater than in the electric structure to account for the sEEGS intensity. Finally, the tip position again does not possess the same clear tilt behavior. Further, the necessary coupling efficiency to the electric mode is roughly an order of magnitude greater than what is observed in the electric structures. Figure 59g is very similar to Figure 59f; however, the y axis now shows the percentage increase in sEEGS, normalized to the electric mode peak, as a function of tilt. This allows for a closer examination of the behaviors in the electric structure and the gap of the magnetic mode. Interestingly a linear fit (included in the figure) fits very well with both aloof positions on the electric structure and the gap position of the magnetic structure.

Discussion

Due to the full head-to-tail dipole configuration in the magnetic mode, there is no net electric dipole, thus negligible coupling to the electric component of the optical field is expected. However, Figure 58f-h and Figure 59a-b clearly show a sEEG peak at the laser energy in the magnetic structure. There are three likely explanations for the presence of this peak: 1) the sEEG peak is coupling to the tail of the higher energy electric mode, 2) the magnetic component of the optical field is driving the magnetic plasmon mode, and 3) phase retardation effects due to the sample tilt allow for coupling between the optical electric field and the magnetic mode.

From the magnetic structure sEEGS results, it can be concluded that the tail of the electric mode is coupling to the laser, though its contributions appear to be minor. This is most clear by the behavior of the sEEGS peak at the gap, where the magnetic mode spontaneous EELS intensity is significantly reduced, compared to the tip. Unlike the tip position, the gap of the magnetic structure behaves similarly to the electric structure: the sEEGS peak increases linearly with increasing tilt. Because the incident light is unpolarized with the wave vector directed at the sample, the electric field component of the incoming photons can be oriented parallel to the tilt axis (horizontal), perpendicular to it (vertical), or a combination of the two. The magnitude of the electric field scales by $\sin^2(\square)$ for photons that are polarized perpendicular to the tilt axis (i.e. a maximum when the substrate is perpendicular to the photon beam and parallel to the electron beam). This is schematically illustrated in Figure 1, where the vector of the net electric dipole projected onto the substrate (dashed red line) is larger at larger tilt. Thus, the observed increase in the sEEGS peak with tilt, suggests coupling from the electric component of the optical field to the electric dipole mode. With that, it is evident that the sEEGS peak in the gap of the magnetic structure can, at least in part, be attributed to coupling from the electric tail of electric mode.

The tip position of the magnetic structure, on the other hand, does not have the same tilt behavior. The sEEGS intensity at the tip possesses no clear trend with tilt, but rather is just has small deviations from the average value. Not only does the tilt behavior deviate from the behavior expected with purely electric excitation, the magnitude of the sEEGS peak at the tip is similar to that observed in the electric structure, despite being detuned from the electric mode. As seen in Figure 59f and g, attributing the magnetic structure sEEGs to coupling to the tail of the electric mode results in a coupling efficiency that is an order of magnitude larger than what is observed in the electric structure. Further, the gap position in the magnetic mode, and the tip position of the electric structure, require more efficient coupling to the electric mode compared to the gap position of the electric mode to account for sEEGS intensity. The magnetic mode intensity at the tip position is much higher at 1.58 eV in these two structures compared to the gap position of the electric mode. Thus, while there is at least some coupling to the electric mode in both structures, there remain obvious discrepancies in the behavior of the two structures and two aloof positions that strongly suggest additional mechanism(s) are involved in the sEEG excitation. As described above, two other coupling mechanisms are possible: namely, exciting the magnetic mode with the magnetic component of the optical field and exciting the magnetic mode via phase retardation effects. Both explanations suggest that the optically dark magnetic mode is being photoexcited and viewed in the near field with sEEGS.

Due to the geometry of our system, a component of the magnetic field of the incident light can be oriented such that it is perpendicular to the plane of the trimer, and consequently can excite the magnetic mode. Figure 55f-k) illustrates that the magnetic field coupling has the opposite tilt-dependence relative to the electric field; namely, decreasing the tilt angle increases the projection of the perpendicular magnetic field, and thus the intensity in the optically driven near field. This

same geometry also creates phase retardation effects. In order to separate the two effects, optical excitation simulations were conducted for two different configurations between the trimer structure and the optical field. The results of these simulations are included in Figure 60, where a) demonstrates a condition in which the magnetic mode can be excited through the threading of magnetic component of the optical field. The spectra all demonstrate a clear peak at 1.85 eV corresponding the electric mode due to the electric field of the laser being oriented along the plane of the trimer for all conditions. The 90° configuration corresponds to an orientation where the magnetic component of the optical field is parallel to the trimer. Here there is no excitation of the magnetic mode, and one single peak is observed. Decreasing the angle corresponds to improved coordination between the magnetic field associated with the magnetic mode of the trimer and the magnetic field of the optical source. The result is the excitation of the magnetic mode which can be seen by the peak at 1.58 eV, this peak increases in intensity with decreasing angle. Thus, the simulations in Figure 60a clearly demonstrate the ability to optically excite the magnetic mode by varying the angle of the optical magnetic field with respect to the trimer.

The second set of simulations (Figure 60b) maintains a parallel orientation between the optical magnetic field and the trimer structure, thus any observable intensity at 1.58 eV would indicate excitation of the magnetic mode through the electric field of the optical source via retardation effects. Regardless of the angle, there is no excitation of the magnetic mode in this configuration. This result indicates that phase retardation effects are not contributing the excitation of the magnetic mode, and thus that the sEEGS signal can be attributed entirely to two contributions: direct excitation of the magnetic mode (as shown in Figure 60a) and minor coupling to the tail of the electric mode.

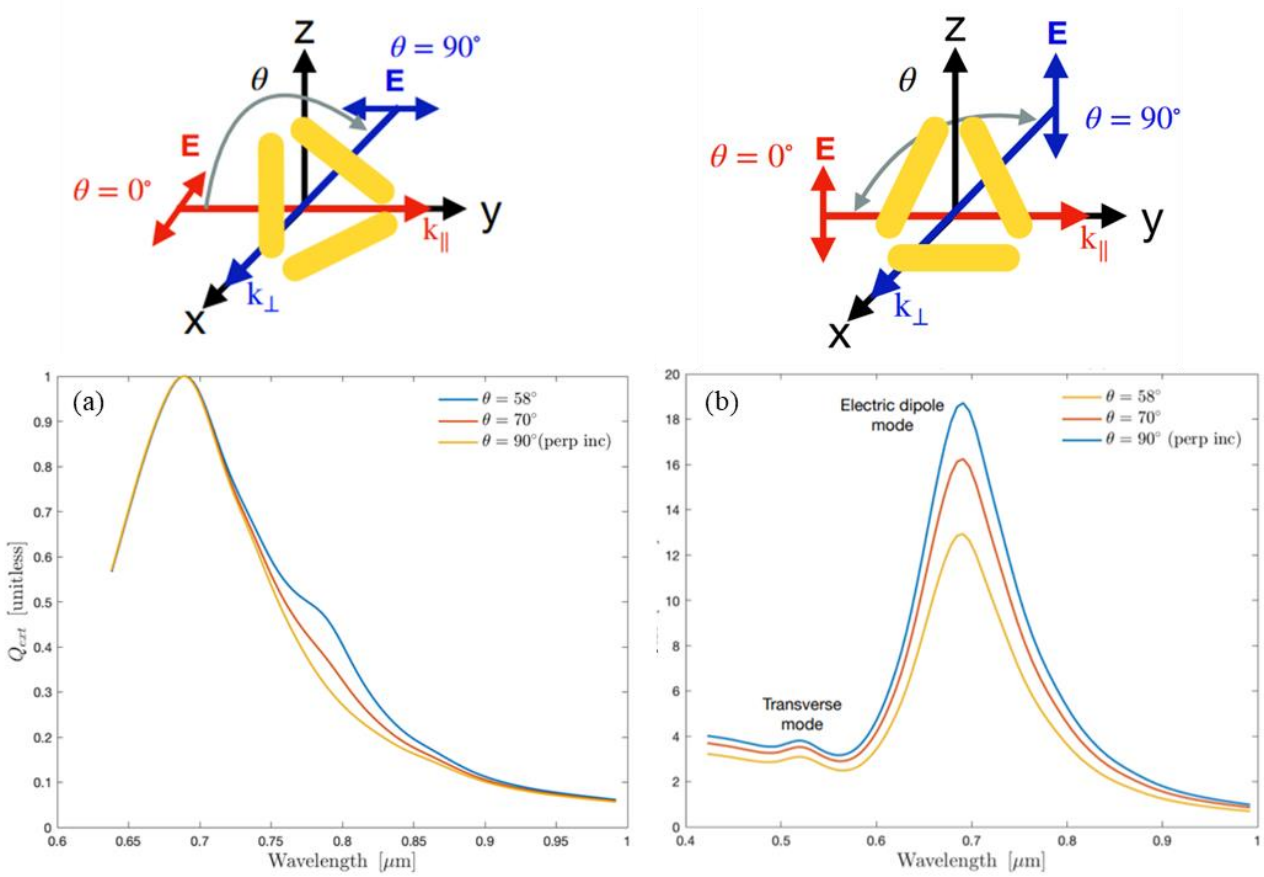

Figure 60: Optical simulations indicating two different tilt axes, a) shows the increase in coupling to the magnetic mode as magnetic field of the optical excitation goes from parallel to the plane of the structure (90°) towards perpendicular with decreasing angle, and b) to observe any potential retardation coupling to the magnetic mode, where the magnetic field remain parallel to the structure for all angles, but the electric field moves towards out of phase.

Conclusions

Au nanorods were patterned in a trimer configuration with sufficiently small gaps to induce the hybridization of the individual rods into a collective lower energy in phase magnetic dipole mode, and an out of phase electric dipole mode. Two trimer structures, termed the magnetic structure and electric structure, were synthesized with different rod lengths to tune one with the magnetic mode energy (1.66 eV vs. 1.58 eV) near our laser and the other with the electric mode near our laser (1.62 eV vs. 1.58 eV). By tilting the trimers (the laser is fixed at 90° relative to the electron beam), optical excitation in the form of a sEEGS peak was observed in both the magnetic structure and the electric structure. A strong positive linear relationship between the sEEGS peak and tilt was observed in the electric structure, whereas the sEEGS intensity in the magnetic structure is relatively constant. By probing the two structures at a gap and tip position, the relative sEEG intensities of the electric and magnetic mode can be modulated due to the position sensitivity of the spontaneous EELS for the in-phase and out-of-phase modes. It was determined that sEEGS intensity increases with increasing tilt angle when the laser energy overlaps strongly with the electric mode. This result is consistent with an increase in the electric field component of the optical field with increasing tilt. Deviations from a simple increase in sEEGS with increasing tilt are consistent with contributions from the magnetic mode. Optical simulations demonstrated excitation of the magnetic mode via the magnetic component of the optical field in a tilted condition, while also demonstrating that retardation effects associated with the electric component of the optical field cannot excite the magnetic mode. Thus, we show that sEEGS is capable of probing the near field of electrically and magnetically driven plasmonic meta-atoms.

Methods

Fabrication

The Au trimer structures were fabricated through a multistep lithography process. Using electron beam lithography, arrays of trimers with different rod lengths and gap sizes were patterned on a 300 μm Si wafer with 30 nm low stress SiN_x coating both sides. Metal deposition of the approximately 40 nm thick Au was done via direct current sputtering; lift off was completed through sonicated baths of alternating acetone and microdeposit remover 1165. In order to obtain electron transparent membranes beneath these metalized areas, the Si was removed with etching in a KOH bath. S1818 photoresist was used to create a mask in which the desired areas for the membranes could be etched using a SiN_x dry etch process. The wafer was then placed in a fixture that protects the metalized side via an air cavity, while the back side with the areas of exposed Si was left open to the environment. This fixture was submerged in a KOH bath at 85°C until the Si was completely removed from the desired areas. Finally, individual TEM samples each with four ~100 x 100 μm 30 nm SiN_x membranes supporting the Au trimer structures were cleaved.

High Resolution EELS

A Nion aberration-corrected high energy resolution monochromated EELS-STEM (HERMES) operated at an accelerating voltage of 60 kV was used to obtain individual point spectra and spectrum images. The convergence and collection semiangles used for the spectrum acquisition were 30 and 15 mrad, respectively. The energy resolution (full width at half-maximum of the zero-loss peak) was approximately 20 meV. A zero-loss peak normalization was used on the EEL spectra included in Figure 56.

Stimulated Electron Energy Loss and Gain Spectroscopy

A Zeiss Libra outfitted with a 785 nm solid state laser oriented normal to the electron beam was used for EELS and sEELS/sEEGS measurements. An acceleration voltage of 200 kV, collection semiangle of 100 mrad and convergence semiangle of 0 mrad were used. A dispersion of 30 meV per channel was obtained via a 0.5 μm monochromator slit is used for spectrum acquisition. Excited state imaging was conducted with an irradiance of 1.3E5 W/cm^2 in the 5 μm Gassian laser spot.

Peak Fitting

Fitting of the EELS and sEELS/sEEGS data was completed in a method similar to prvious sEEGS experiments[7,8]. First, a Gaussian was fit to the zero-loss peak. This peak was then subtracted from the data. Next, the SiN_x background was removed by a combination of four Lorentzian peaks. The sEEGS peak was then fit by first removing the tail left by the zero-loss peak, and then via a single Lorentzian while inputting a position of -1.58 eV (the laser energy) and the previously determined full width half max from the zero-loss peak. For the loss peaks, the tail from the zero-loss was removed. The peak positions for the electric and magnetic modes were then determined by fitting the flat no laser EELS spectra. For excited state spectra, after removing the zero-loss peak tail, the sEELS peak was removed by subtracting the sEEGS peak mirrored to the 1.58 eV. Finally, using the peak positions obtained from the flat, no laser irradiance spectra, the two modes were fit to two Lorentzian, with an additional Lorentzian fitting the Au peak at ~2.4 eV.

REFERENCES

(1) Wu, Y.; Fowlkes, J. D.; Roberts, N. A.; Diez, J. A.; Kondic, L.; González, A. G.; Rack, P. D. Competing Liquid Phase Instabilities during Pulsed Laser Induced Self-Assembly of Copper Rings into Ordered Nanoparticle Arrays on SiO2. *Langmuir* **2011**, *27* (21), 13314–13323. https://doi.org/10.1021/la203165v.

(2) D. Fowlkes, J.; Kondic, L.; A. Diez, J.; G. González, A.; Wu, Y.; A. Roberts, N.; E. McCold, C.; D. Rack, P. Parallel Assembly of Particles and Wires on Substrates by Dictating Instability Evolution in Liquid Metal Films. *Nanoscale* **2012**, *4* (23), 7376–7382. https://doi.org/10.1039/C2NR31637D.

(3) Fowlkes, J. D.; Roberts, N. A.; Wu, Y.; Diez, J. A.; González, A. G.; Hartnett, C.; Mahady, K.; Afkhami, S.; Kondic, L.; Rack, P. D. Hierarchical Nanoparticle Ensembles Synthesized by Liquid Phase Directed Self-Assembly. *Nano Lett.* **2014**, *14* (2), 774–782. https://doi.org/10.1021/nl404128d.

(4) Maier, S. A. Electromagnetics of Metals. In *Plasmonics: Fundamentals and Applications*; Springer, New York, NY, 2007; pp 5–19. https://doi.org/10.1007/0-387-37825-1_1.

(5) Santhanam, V. Scalable Synthesis of Noble Metal Nanoparticles. In *Nanoscale and Microscale Phenomena*; Springer Tracts in Mechanical Engineering; Springer, New Delhi, 2015; pp 59–81. https://doi.org/10.1007/978-81-322-2289-7_4.

(6) Egorova, E. M.; Kubatiev, A. A.; Schvets, V. I. Biochemical Synthesis of Metal Nanoparticles. In *Biological Effects of Metal Nanoparticles*; Springer, Cham, 2016; pp 79–107. https://doi.org/10.1007/978-3-319-30906-4_2.

(7) Collette, R.; Garfinkel, D. A.; Hu, Z.; Masiello, D. J.; Rack, P. D. Near Field Excited State Imaging via Stimulated Electron Energy Gain Spectroscopy of Localized Surface Plasmon Resonances in Plasmonic Nanorod Antennas. *Scientific Reports* **2020**, *10* (1), 12537. https://doi.org/10.1038/s41598-020-69066-z.

(8) Collette, R.; Garfinkel, D. A.; Rack, P. D. Nearfield Excited State Imaging of Bonding and Antibonding Plasmon Modes in Nanorod Dimers via Stimulated Electron Energy Gain Spectroscopy. *J. Chem. Phys.* **2020**, *153* (4), 044711. https://doi.org/10.1063/5.0012260.

(9) AdNaNoTek Magnetron Sputtering Deposition https://www.adnano-tek.com/magnetron-sputtering-deposition-msd.html (accessed 2021 -08 -31).

(10) Gennes, P.-G. de; Brochard-Wyart, F.; Quéré, D. Capillarity: Deformable Interfaces. In *Capillarity and Wetting Phenomena*; Springer, New York, NY, 2004; pp 1–31. https://doi.org/10.1007/978-0-387-21656-0_1.

(11) Ruckenstein, E.; Jain, R. K. Spontaneous Rupture of Thin Liquid Films. *J. Chem. Soc., Faraday Trans. 2* **1974**, *70* (0), 132–147. https://doi.org/10.1039/F29747000132.

(12) Guastalla, J. Recent Work on Surface Activity, Wetting and Dewetting. *Journal of Colloid Science* **1956**, *11* (4), 623–636. https://doi.org/10.1016/0095-8522(56)90178-7.

(13) Padday, J. F. Cohesive Properties of Thin Films of Liquids Adhering to a Solid Surface. *Spec. Discuss. Faraday Soc.* **1970**, *1* (0), 64–74. https://doi.org/10.1039/SD9700100064.

(14) Bischof, J.; Scherer, D.; Herminghaus, S.; Leiderer, P. Dewetting Modes of Thin Metallic Films: Nucleation of Holes and Spinodal Dewetting. *Phys. Rev. Lett.* **1996**, *77* (8), 1536–1539. https://doi.org/10.1103/PhysRevLett.77.1536.

(15) Thompson, C. V. Solid-State Dewetting of Thin Films. *Annual Review of Materials Research* **2012**, *42* (1), 399–434. https://doi.org/10.1146/annurev-matsci-070511-155048.
(16) Jiran, E.; Thompson, C. V. Capillary Instabilities in Thin, Continuous Films. *Thin Solid Films* **1992**, *208* (1), 23–28. https://doi.org/10.1016/0040-6090(92)90941-4.
(17) Diez, J. A.; González, A. G.; Kondic, L. On the Breakup of Fluid Rivulets. *Physics of Fluids* **2009**, *21* (8), 082105. https://doi.org/10.1063/1.3211248.
(18) Diez, J. A.; Kondic, L. On the Breakup of Fluid Films of Finite and Infinite Extent. *Physics of Fluids* **2007**, *19* (7), 072107. https://doi.org/10.1063/1.2749515.
(19) Amendola, V.; Pilot, R.; Frasconi, M.; Maragò, O. M.; Iatì, M. A. Surface Plasmon Resonance in Gold Nanoparticles: A Review. *J. Phys.: Condens. Matter* **2017**, *29* (20), 203002. https://doi.org/10.1088/1361-648X/aa60f3.
(20) Wu, Y.; Li, G.; Cherqui, C.; Bigelow, N. W.; Thakkar, N.; Masiello, D. J.; Camden, J. P.; Rack, P. D. Electron Energy Loss Spectroscopy Study of the Full Plasmonic Spectrum of Self-Assembled Au–Ag Alloy Nanoparticles: Unraveling Size, Composition, and Substrate Effects. *ACS Photonics* **2016**, *3* (1), 130–138. https://doi.org/10.1021/acsphotonics.5b00548.
(21) Davis, T. J.; Gómez, D. E.; Roberts, A. Plasmonic Circuits for Manipulating Optical Information. *Nanophotonics* **2017**, *6* (3), 543–559. https://doi.org/10.1515/nanoph-2016-0131.
(22) Quillin, S. C.; Cherqui, C.; Montoni, N. P.; Li, G.; Camden, J. P.; Masiello, D. J. Imaging Plasmon Hybridization in Metal Nanoparticle Aggregates with Electron Energy-Loss Spectroscopy. *J. Phys. Chem. C* **2016**, *120* (37), 20852–20859. https://doi.org/10.1021/acs.jpcc.6b02170.
(23) Magnetic-Materials-Background-4-Classification-of-Magnetic-Materials.Pdf.
(24) magnetic nano particles in bio medical applications https://www.slideshare.net/hassan7777777/magnetic-nano-particles-in-bio-medical-applications (accessed 2021 -08 -31).
(25) Ruffino, F.; Carria, E.; Kimiagar, S.; Crupi, I.; Grimaldi, M. G. Rayleigh-Instability-Driven Dewetting of Thin Au and Ag Films on Indium–Tin-Oxide Surface under Nanosecond Laser Irradiations. *Micro & Nano Letters* **2013**, *8* (3), 127–130. https://doi.org/10.1049/mnl.2012.0870.
(26) Ratautas, K.; Gedvilas, M.; Račiukaitis, G.; Grigonis, A. Nanoparticle Formation after Nanosecond-Laser Irradiation of Thin Gold Films. *Journal of Applied Physics* **2012**, *112* (1), 013108. https://doi.org/10.1063/1.4731253.
(27) Ruffino, F.; Pugliara, A.; Carria, E.; Romano, L.; Bongiorno, C.; Fisicaro, G.; La Magna, A.; Spinella, C.; Grimaldi, M. G. Towards a Laser Fluence Dependent Nanostructuring of Thin Au Films on Si by Nanosecond Laser Irradiation. *Applied Surface Science* **2012**, *258* (23), 9128–9137. https://doi.org/10.1016/j.apsusc.2011.12.087.
(28) Yadavali, S.; Khenner, M.; Kalyanaraman, R. Pulsed Laser Dewetting of Au Films: Experiments and Modeling of Nanoscale Behavior. *Journal of Materials Research* **2013**, *28* (13), 1715–1723. https://doi.org/10.1557/jmr.2013.90.
(29) Oh, Y.; Lee, M. Single-Pulse Transformation of Ag Thin Film into Nanoparticles via Laser-Induced Dewetting. *Applied Surface Science* **2017**, *399*, 555–564. https://doi.org/10.1016/j.apsusc.2016.12.027.

(30) Nikov, Ru. G.; Nedyalkov, N. N.; Atanasov, P. A.; Hirsch, D.; Rauschenbach, B.; Grochowska, K.; Sliwinski, G. Characterization of Ag Nanostructures Fabricated by Laser-Induced Dewetting of Thin Films. *Applied Surface Science* **2016**, *374*, 36–41. https://doi.org/10.1016/j.apsusc.2015.09.004.
(31) El-Sayed, H. A.; Horwood, C. A.; Owusu-Ansah, E.; Shi, Y. J.; Birss, V. I. Gold Nanoparticle Array Formation on Dimpled Ta Templates Using Pulsed Laser-Induced Thin Film Dewetting. *Physical Chemistry Chemical Physics* **2015**, *17* (16), 11062–11069. https://doi.org/10.1039/c5cp00924c.
(32) Mckeown, J. T.; Roberts, N. A.; Fowlkes, J. D.; Campbell, G. H.; Browning, N. D.; Rack, P. D. Ultrafast Laser Dewetting of Thin Metal Films. *Presented at: Frontiers of Electron Microscopy in Materials Science, Rohnert Park, CA, United States* **2011**.
(33) Rack, P. D.; Guan, Y.; Fowlkes, J. D.; Melechko, A. V.; Simpson, M. L. Pulsed Laser Dewetting of Patterned Thin Metal Films: A Means of Directed Assembly. *Appl. Phys. Lett.* **2008**, *92* (22), 223108. https://doi.org/10.1063/1.2939436.
(34) Maekawa, Y.; Shibuta, Y. Dewetting Dynamics of Nickel Thin Film on Alpha-Quartz Substrate: A Molecular Dynamics Study. *Chemical Physics Letters* **2016**, *658*, 30–36. https://doi.org/10.1016/j.cplett.2016.06.016.
(35) Kondic, L.; Diez, J. A.; Rack, P. D.; Guan, Y.; Fowlkes, J. D. Nanoparticle Assembly via the Dewetting of Patterned Thin Metal Lines: Understanding the Instability Mechanisms. *Phys. Rev. E* **2009**, *79* (2), 026302. https://doi.org/10.1103/PhysRevE.79.026302.
(36) González, A. G.; Diez, J. A.; Wu, Y.; Fowlkes, J. D.; Rack, P. D.; Kondic, L. Instability of Liquid Cu Films on a SiO2 Substrate. *Langmuir* **2013**, *29* (30), 9378–9387. https://doi.org/10.1021/la4009784.
(37) Kunwar, S.; Pandey, P.; Sui, M.; Zhang, Q.; Li, M.-Y.; Lee, J. Nanoscale Morphology and Optical Property Evolution of Pt Nanostructures on GaN (0 0 0 1) by the Systematic Control of Annealing Temperature and Duration with Various Pt Thickness. *Mater. Res. Express* **2017**, *4* (6), 065019. https://doi.org/10.1088/2053-1591/aa72be.
(38) Owusu-Ansah, E.; Horwood, C. A.; El-Sayed, H. A.; Birss, V. I.; Shi, Y. J. A Method for the Formation of Pt Metal Nanoparticle Arrays Using Nanosecond Pulsed Laser Dewetting. *Appl. Phys. Lett.* **2015**, *106* (20), 203103. https://doi.org/10.1063/1.4921528.
(39) Okamoto, H. Supplemental Literature Review of Binary Phase Diagrams: Ag-Ni, Al-Cu, Al-Sc, C-Cr, Cr-Ir, Cu-Sc, Eu-Pb, H-V, Hf-Sn, Lu-Pb, Sb-Yb, and Sn-Y. *J. Phase Equilib. Diffus.* **2013**, *34* (6), 493–505. https://doi.org/10.1007/s11669-013-0256-8.
(40) Yang, K.; Kryutyanskiy, V.; Kolmychek, I.; Murzina, T. V.; Lukaszew, R. A. Experimental Correlation between Nonlinear Optical and Magnetotransport Properties Observed in Au-Co Thin Films. *Journal of Nanomaterials* **2016**, *2016*, e4786545. https://doi.org/10.1155/2016/4786545.
(41) Herminghaus, S.; Jacobs, K.; Mecke, K.; Bischof, J.; Fery, A.; Ibn-Elhaj, M.; Schlagowski, S. Spinodal Dewetting in Liquid Crystal and Liquid Metal Films. *Science* **1998**, *282* (5390), 916–919. https://doi.org/10.1126/science.282.5390.916.
(42) Nguyen, T. D.; Fuentes-Cabrera, M.; Fowlkes, J. D.; Rack, P. D. Coexistence of Spinodal Instability and Thermal Nucleation in Thin-Film Rupture: Insights from Molecular Levels. *Phys. Rev. E* **2014**, *89* (3), 032403. https://doi.org/10.1103/PhysRevE.89.032403.

(43) Thiele, U.; Velarde, M. G.; Neuffer, K. Dewetting: Film Rupture by Nucleation in the Spinodal Regime. *Physical Review Letters* **2001**, *87* (1). https://doi.org/10.1103/PhysRevLett.87.016104.
(44) Oh, Y.; Lee, J.; Lee, M. Fabrication of Ag-Au Bimetallic Nanoparticles by Laser-Induced Dewetting of Bilayer Films. *Applied Surface Science* **2018**, *434*, 1293–1299. https://doi.org/10.1016/j.apsusc.2017.11.245.
(45) Qiu, G.; Ng, S. P.; Wu, C.-M. L. Bimetallic Au-Ag Alloy Nanoislands for Highly Sensitive Localized Surface Plasmon Resonance Biosensing. *Sensors and Actuators B: Chemical* **2018**, *265*, 459–467. https://doi.org/10.1016/j.snb.2018.03.066.
(46) Goswami, A.; Aravindan, S.; Rao, P. V. Fabrication of Substrate Supported Bimetallic Nanoparticles and Their Optical Characterization through Reflection Spectra. *Superlattices and Microstructures* **2016**, *91*, 252–258. https://doi.org/10.1016/j.spmi.2016.01.016.
(47) Sachan, R.; Malasi, A.; Yadavali, S.; Griffey, B.; Dunlap, J.; Duscher, G.; Kalyanaraman, R. Laser-Induced Self-Assembled Nanostructures on Electron-Transparent Substrates. *Particle & Particle Systems Characterization* **2015**, *32* (4), 476–482. https://doi.org/10.1002/ppsc.201400183.
(48) Sachan, R.; Yadavali, S.; Shirato, N.; Krishna, H.; Ramos, V.; Duscher, G.; Pennycook, S. J.; Gangopadhyay, A. K.; Garcia, H.; R Kalyanaraman. Self-Organized Bimetallic Ag–Co Nanoparticles with Tunable Localized Surface Plasmons Showing High Environmental Stability and Sensitivity. *Nanotechnology* **2012**, *23* (27), 275604. https://doi.org/10.1088/0957-4484/23/27/275604.
(49) Sachan, R.; Malasi, A.; Ge, J.; Yadavali, S.; Krishna, H.; Gangopadhyay, A.; Garcia, H.; Duscher, G.; Kalyanaraman, R. Ferroplasmons: Intense Localized Surface Plasmons in Metal-Ferromagnetic Nanoparticles. *ACS Nano* **2014**, *8* (10), 9790–9798. https://doi.org/10.1021/nn5031719.
(50) Garcia, H.; Sachan, R.; Kalyanaraman, R. Optical Plasmon Properties of Co-Ag Nanocomposites Within the Mean-Field Approximation. *Plasmonics* **2012**, *7* (1), 137–141. https://doi.org/10.1007/s11468-011-9286-4.
(51) Pandey, P.; Kunwar, S.; Sui, M.; Bastola, S.; Lee, J. Compositional Effect on the Fabrication of AgxPd1−x Alloy Nanoparticles on C-Plane Sapphire at Distinctive Stages of the Solid-State-Dewetting of Bimetallic Thin Films. *RSC Adv.* **2017**, *7* (87), 55471–55481. https://doi.org/10.1039/C7RA11058H.
(52) Pandey, P.; Kunwar, S.; Sui, M.; Bastola, S.; Lee, J. Role of Annealing Temperature, Time, and Composition on the Fabrication of Aux Pd1 #8722;x Nanostructures on c-Plane Sapphire by the Solid-State Dewetting of Bimetallic Thin Films. *IEEE Transactions on Nanotechnology* **2018**, *17* (2), 325–331. https://doi.org/10.1109/TNANO.2018.2801943.
(53) McKeown, J. T.; Wu, Y.; Fowlkes, J. D.; Rack, P. D.; Campbell, G. H. Simultaneous In-Situ Synthesis and Characterization of Co@Cu Core-Shell Nanoparticle Arrays. *Advanced Materials* **2015**, *27* (6), 1060–1065. https://doi.org/10.1002/adma.201404374.
(54) Wu, Y.; Fowlkes, J. D.; Rack, P. D. The Optical Properties of Cu-Ni Nanoparticles Produced via Pulsed Laser Dewetting of Ultrathin Films: The Effect of Nanoparticle Size and Composition on the Plasmon Response. *Journal of Materials Research* **2011**, *26* (2), 277–287. https://doi.org/10.1557/jmr.2010.9.

(55) Fowlkes, J. D.; Wu, Y.; Rack, P. D. Directed Assembly of Bimetallic Nanoparticles by Pulsed-Laser-Induced Dewetting: A Unique Time and Length Scale Regime. *ACS Appl. Mater. Interfaces* **2010**, *2* (7), 2153–2161. https://doi.org/10.1021/am100417x.
(56) Oh, Y.-J.; Kim, J.-H.; V. Thompson, C.; A. Ross, C. Templated Assembly of Co–Pt Nanoparticles via Thermal and Laser-Induced Dewetting of Bilayer Metal Films. *Nanoscale* **2013**, *5* (1), 401–407. https://doi.org/10.1039/C2NR32932H.
(57) Seo, O.; Oh, S. A.; Lee, J. Y.; Ha, S. S.; Kim, J. M.; Choi, J. W.; Kim, J.-W.; Kang, H. C.; Noh, D. Y. Controlling the Alloy Composition of PtNi Nanocrystals Using Solid-State Dewetting of Bilayer Films. *Journal of Alloys and Compounds* **2016**, *667*, 141–145. https://doi.org/10.1016/j.jallcom.2016.01.111.
(58) Censabella, M.; Ruffino, F.; Zimbone, M.; Bruno, E.; Grimaldi, M. G. Self-Organization Based Fabrication of Bimetallic PtPd Nanoparticles on Transparent Conductive Oxide Substrates. *physica status solidi (a)* **2018**, *215* (3), 1700524. https://doi.org/10.1002/pssa.201700524.
(59) Oh, Y.-J.; Ross, C. A.; Jung, Y. S.; Wang, Y.; Thompson, C. V. Cobalt Nanoparticle Arrays Made by Templated Solid-State Dewetting. *Small* **2009**, *5* (7), 860–865. https://doi.org/10.1002/smll.200801433.
(60) Giermann, A. L.; Thompson, C. V. Solid-State Dewetting for Ordered Arrays of Crystallographically Oriented Metal Particles. *Appl. Phys. Lett.* **2005**, *86* (12), 121903. https://doi.org/10.1063/1.1885180.
(61) Hartnett, C. A.; Mahady, K.; Fowlkes, J. D.; Afkhami, S.; Kondic, L.; Rack, P. D. Instability of Nano- and Microscale Liquid Metal Filaments: Transition from Single Droplet Collapse to Multidroplet Breakup. *Langmuir* **2015**, *31* (50), 13609–13617. https://doi.org/10.1021/acs.langmuir.5b03598.
(62) Meshot, E. R.; Zhao, Z.; Lu, W.; Hart, A. J. Self-Ordering of Small-Diameter Metal Nanoparticles by Dewetting on Hexagonal Mesh Templates. *Nanoscale* **2014**, *6* (17), 10106–10112. https://doi.org/10.1039/C4NR01501K.
(63) Yang, S.; Xu, F.; Ostendorp, S.; Wilde, G.; Zhao, H.; Lei, Y. Template-Confined Dewetting Process to Surface Nanopatterns: Fabrication, Structural Tunability, and Structure-Related Properties. *Advanced Functional Materials* **2011**, *21* (13), 2446–2455. https://doi.org/10.1002/adfm.201002387.
(64) Sundar, A.; Decker, C. J.; Hughes, R. A.; Neretina, S. The Templated Assembly of Highly Faceted Three-Dimensional Gold Microstructures into Periodic Arrays. *Materials Letters* **2012**, *76*, 155–158. https://doi.org/10.1016/j.matlet.2012.02.091.
(65) Altomare, M.; Nguyen, N. T.; Schmuki, P. Templated Dewetting: Designing Entirely Self-Organized Platforms for Photocatalysis. *Chem. Sci.* **2016**, *7* (12), 6865–6886. https://doi.org/10.1039/C6SC02555B.
(66) Habenicht, A.; Olapinski, M.; Burmeister, F.; Leiderer, P.; Boneberg, J. Jumping Nanodroplets. *Science* **2005**, *309* (5743), 2043–2045. https://doi.org/10.1126/science.1116505.
(67) Guan, Y. F.; Pearce, R. C.; Melechko, A. V.; Hensley, D. K.; Simpson, M. L.; Rack, P. D. Pulsed Laser Dewetting of Nickel Catalyst for Carbon Nanofiber Growth. *Nanotechnology* **2008**, *19* (23), 235604. https://doi.org/10.1088/0957-4484/19/23/235604.

(68) Oh, H.; Lee, J.; Lee, M. Transformation of Silver Nanowires into Nanoparticles by Rayleigh Instability: Comparison between Laser Irradiation and Heat Treatment. *Applied Surface Science* **2018**, *427*, 65–73. https://doi.org/10.1016/j.apsusc.2017.08.102.
(69) Wu, Y.; Fowlkes, J. D.; Rack, P. D.; Diez, J. A.; Kondic, L. On the Breakup of Patterned Nanoscale Copper Rings into Droplets via Pulsed-Laser-Induced Dewetting: Competing Liquid-Phase Instability and Transport Mechanisms. *Langmuir* **2010**, *26* (14), 11972–11979. https://doi.org/10.1021/la1013818.
(70) Roberts, N. A.; Fowlkes, J. D.; Mahady, K.; Afkhami, S.; Kondic, L.; Rack, P. D. Directed Assembly of One- and Two-Dimensional Nanoparticle Arrays from Pulsed Laser Induced Dewetting of Square Waveforms. *ACS Appl. Mater. Interfaces* **2013**, *5* (10), 4450–4456. https://doi.org/10.1021/am400925h.
(71) Mahady, K.; Afkhami, S.; Kondic, L. On the Influence of Initial Geometry on the Evolution of Fluid Filaments. *Physics of Fluids* **2015**, *27* (9), 092104. https://doi.org/10.1063/1.4931086.
(72) Fowlkes, J. D.; Kondic, L.; Wu, Y.; Rack, P. D.; Diez, J. A. Self- versus Directed-Assembly of Nanoparticles via Pulsed Laser Induced Dewetting of Patterned Metal Films. *Nano Letters* **2011**, *11* (6), 2478–2485. https://doi.org/10.1021/nl200921c.
(73) Wu, Y.; Dong, N.; Fu, S.; Fowlkes, J. D.; Kondic, L.; Vincenti, M. A.; de Ceglia, D.; Rack, P. D. Directed Liquid Phase Assembly of Highly Ordered Metallic Nanoparticle Arrays. *ACS Appl. Mater. Interfaces* **2014**, *6* (8), 5835–5843. https://doi.org/10.1021/am500695h.
(74) Petryayeva, E.; Krull, U. J. Localized Surface Plasmon Resonance: Nanostructures, Bioassays and Biosensing—A Review. *Analytica chimica acta* **2011**, *706* (1), 8–24. https://doi.org/10.1016/j.aca.2011.08.020.
(75) Chen, Y.; Ming, H. Review of Surface Plasmon Resonance and Localized Surface Plasmon Resonance Sensor. **光子**传感器：英文版 **2012**, *2* (1), 37–49. https://doi.org/10.1007/s13320-011-0051-2.
(76) Kracker, M.; Worsch, C.; Bocker, C.; Rüssel, C. Optical Properties of Dewetted Thin Silver/Gold Multilayer Films on Glass Substrates. *Thin Solid Films* **2013**, *539*, 47–54. https://doi.org/10.1016/j.tsf.2013.04.153.
(77) Tesler, A. B.; Maoz, B. M.; Feldman, Y.; Vaskevich, A.; Rubinstein, I. Solid-State Thermal Dewetting of Just-Percolated Gold Films Evaporated on Glass: Development of the Morphology and Optical Properties. *Journal of physical chemistry. C* **2013**, *117* (21), 11337–11346. https://doi.org/10.1021/jp400895z.
(78) Lee, K.-S.; El-Sayed, M. A. Dependence of the Enhanced Optical Scattering Efficiency Relative to That of Absorption for Gold Metal Nanorods on Aspect Ratio, Size, End-Cap Shape, and Medium Refractive Index. *J Phys Chem B* **2005**, *109* (43), 20331–20338. https://doi.org/10.1021/jp054385p.
(79) Loo, C.; Lin, A.; Hirsch, L.; Lee, M.-H.; Barton, J.; Halas, N.; West, J.; Drezek, R. Nanoshell-Enabled Photonics-Based Imaging and Therapy of Cancer. *Technol Cancer Res Treat* **2004**, *3* (1), 33–40. https://doi.org/10.1177/153303460400300104.
(80) Skrabalak, S. E.; Chen, J.; Sun, Y.; Lu, X.; Au, L.; Cobley, C. M.; Xia, Y. Gold Nanocages: Synthesis, Properties, and Applications. *Acc Chem Res* **2008**, *41* (12), 1587–1595. https://doi.org/10.1021/ar800018v.
(81) Barbillon, G.; Bijeon, J.-L.; Plain, J.; de la Chapelle, M. L.; Adam, P.-M.; Royer, P. Electron Beam Lithography Designed Chemical Nanosensors Based on Localized

Surface Plasmon Resonance. *Surface Science* **2007**, *601*, 5057–5061. https://doi.org/10.1016/j.susc.2007.09.005.
(82) Cinel, N. A.; Bütün, S.; Özbay, E. Electron Beam Lithography Designed Silver Nano-Disks Used as Label Free Nano-Biosensors Based on Localized Surface Plasmon Resonance. *Opt. Express, OE* **2012**, *20* (3), 2587–2597. https://doi.org/10.1364/OE.20.002587.
(83) Singh, J.; Soni, R. K. Tunable Optical Properties of Au Nanoparticles Encapsulated TiO2 Spheres and Their Improved Sunlight Mediated Photocatalytic Activity. *Colloids and Surfaces A: Physicochemical and Engineering Aspects* **2021**, *612*, 126011. https://doi.org/10.1016/j.colsurfa.2020.126011.
(84) Balamurugan, B.; Maruyama, T. Evidence of an Enhanced Interband Absorption in Au Nanoparticles:Size-Dependent Electronic Structure and Optical Properties. *Applied physics letters* **2005**, *87* (14), 143105-143105–3. https://doi.org/10.1063/1.2077834.
(85) Smitha, S. L.; Gopchandran, K. G.; Smijesh, N.; Philip, R. Size-Dependent Optical Properties of Au Nanorods. *Progress in Natural Science: Materials International* **2013**, *23* (1), 36–43. https://doi.org/10.1016/j.pnsc.2013.01.005.
(86) García de Abajo, F. J. Optical Excitations in Electron Microscopy. *Rev. Mod. Phys.* **2010**, *82* (1), 209–275. https://doi.org/10.1103/RevModPhys.82.209.
(87) Cherqui, C.; Thakkar, N.; Li, G.; Camden, J. P.; Masiello, D. J. Characterizing Localized Surface Plasmons Using Electron Energy-Loss Spectroscopy. *Annual Review of Physical Chemistry* **2016**, *67* (1), 331–357. https://doi.org/10.1146/annurev-physchem-040214-121612.
(88) Kociak, M.; Stéphan, O. Mapping Plasmons at the Nanometer Scale in an Electron Microscope. *Chem. Soc. Rev.* **2014**, *43* (11), 3865–3883. https://doi.org/10.1039/C3CS60478K.
(89) Rossouw, D.; Couillard, M.; Vickery, J.; Kumacheva, E.; Botton, G. A. Multipolar Plasmonic Resonances in Silver Nanowire Antennas Imaged with a Subnanometer Electron Probe. *Nano Lett.* **2011**, *11* (4), 1499–1504. https://doi.org/10.1021/nl200634w.
(90) Wu, Y.; Hu, Z.; Kong, X.-T.; Idrobo, J. C.; Nixon, A. G.; Rack, P. D.; Masiello, D. J.; Camden, J. P. Infrared Plasmonics: STEM-EELS Characterization of Fabry-P\'erot Resonance Damping in Gold Nanowires. *Phys. Rev. B* **2020**, *101* (8), 085409. https://doi.org/10.1103/PhysRevB.101.085409.
(91) Keast, V. J.; Walhout, C. J.; Pedersen, T.; Shahcheraghi, N.; Cortie, M. B.; Mitchell, D. R. G. Higher Order Plasmonic Modes Excited in Ag Triangular Nanoplates by an Electron Beam. *Plasmonics* **2016**, *11* (4), 1081–1086. https://doi.org/10.1007/s11468-015-0145-6.
(92) Park, S.; Ahn, Y. Substrate Effects on Terahertz Metamaterial Resonances for Various Metal Thicknesses. *Journal of the Korean Physical Society* **2015**, *65*, 1843–1847. https://doi.org/10.3938/jkps.65.1843.
(93) Shen, Q.; Hou, B.; Chen, Z.; Wang, Z.-L. Effect of Gap Width on Enhanced Magnetic Optical Fields in Metallic Split Ring Resonators. *AIP Advances* **2012**, *2*. https://doi.org/10.1063/1.4770319.
(94) Miyamaru, F.; Kubota, S.; Nakanishi, T.; Kawashima, S.; Sato, N.; Kitano, M.; Takeda, M. W. Transmission Properties of Double-Gap Asymmetric Split Ring Resonators in Terahertz Region. *Appl. Phys. Lett.* **2012**, *101* (5), 051112. https://doi.org/10.1063/1.4739945.

(95) Cube, F. von; Irsen, S.; Niegemann, J.; Matyssek, C.; Hergert, W.; Busch, K.; Linden, S. Spatio-Spectral Characterization of Photonic Meta-Atoms with Electron Energy-Loss Spectroscopy [Invited]. *Opt. Mater. Express, OME* **2011**, *1* (5), 1009–1018. https://doi.org/10.1364/OME.1.001009.
(96) Von Cube, F.; Irsen, S.; Diehl, R.; Niegemann, J.; Busch, K.; Linden, S. From Isolated Metaatoms to Photonic Metamaterials: Evolution of the Plasmonic near-Field. *Nano letters* **2013**, *13* (2), 703–708. https://doi.org/10.1021/nl3043757.
(97) Kadkhodazadeh, S.; Christensen, T.; Beleggia, M.; Mortensen, N. A.; Wagner, J. B. The Substrate Effect in Electron Energy-Loss Spectroscopy of Localized Surface Plasmons in Gold and Silver Nanoparticles. *ACS Photonics* **2017**, *4* (2), 251–261. https://doi.org/10.1021/acsphotonics.6b00489.
(98) Liu, D.; Fang, L.; Zhou, F.; Li, H.; Zhang, T.; Li, C.; Cai, W.; Deng, Z.; Li, L.; Li, Y. Ultrasensitive and Stable Au Dimer-Based Colorimetric Sensors Using the Dynamically Tunable Gap-Dependent Plasmonic Coupling Optical Properties. *Advanced Functional Materials* **2018**, *28* (18), 1707392. https://doi.org/10.1002/adfm.201707392.
(99) Kadkhodazadeh, S.; de Lasson, J. R.; Beleggia, M.; Kneipp, H.; Wagner, J. B.; Kneipp, K. Scaling of the Surface Plasmon Resonance in Gold and Silver Dimers Probed by EELS. *J. Phys. Chem. C* **2014**, *118* (10), 5478–5485. https://doi.org/10.1021/jp500288s.
(100) Pakeltis, G.; Rotunno, E.; Khorassani, S.; Garfinkel, D. A.; Collette, R.; West, C. A.; Retterer, S. T.; Idrobo, J. C.; Masiello, D. J.; Masiello, D. J.; Rack, P. D.; Rack, P. D. High Spatial and Energy Resolution Electron Energy Loss Spectroscopy of the Magnetic and Electric Excitations in Plasmonic Nanorod Oligomers. *Opt. Express, OE* **2021**, *29* (3), 4661–4671. https://doi.org/10.1364/OE.416046.
(101) Hughes, R. A.; Menumerov, E.; Neretina, S. When Lithography Meets Self-Assembly: A Review of Recent Advances in the Directed Assembly of Complex Metal Nanostructures on Planar and Textured Surfaces. *Nanotechnology* **2017**, *28* (28), 282002. https://doi.org/10.1088/1361-6528/aa77ce.
(102) Controllable femtosecond laser-induced dewetting for plasmonic applications - Makarov - 2016 - Laser & Photonics Reviews - Wiley Online Library https://onlinelibrary.wiley.com/doi/abs/10.1002/lpor.201500119 (accessed 2021 -08 -25).
(103) Ruffino, F.; Grimaldi, M. G. Nanostructuration of Thin Metal Films by Pulsed Laser Irradiations: A Review. *Nanomaterials (Basel)* **2019**, *9* (8), 1133. https://doi.org/10.3390/nano9081133.
(104) Kondic, L.; González, A.; Diez, J.; Fowlkes, J.; Rack, P. Liquid-State Dewetting of Pulsed-Laser-Heated Nanoscale Metal Films and Other Geometries. *Annual Review of Fluid Mechanics* **2020**, *52*. https://doi.org/10.1146/annurev-fluid-010719-060340.
(105) Yadavali, S.; Krishna, H.; Kalyanaraman, R. Morphology Transitions in Bilayer Spinodal Dewetting Systems. *Phys. Rev. B* **2012**, *85* (23), 235446. https://doi.org/10.1103/PhysRevB.85.235446.
(106) Khenner, M.; Yadavali, S.; Kalyanaraman, R. Formation of Organized Nanostructures from Unstable Bilayers of Thin Metallic Liquids. *Physics of Fluids* **2011**, *23*, 122105-122105–122114. https://doi.org/10.1063/1.3665618.
(107) Garfinkel, D. A.; Pakeltis, G.; Tang, N.; Ivanov, I. N.; Fowlkes, J. D.; Gilbert, D. A.; Rack, P. D. Optical and Magnetic Properties of Ag–Ni Bimetallic Nanoparticles Assembled via Pulsed Laser-Induced Dewetting. *ACS Omega* **2020**, *5* (30), 19285–19292. https://doi.org/10.1021/acsomega.0c02894.

(108) Mao, S.; Kuldinow, D.; Haataja, M. P.; Košmrlj, A. Phase Behavior and Morphology of Multicomponent Liquid Mixtures. *Soft Matter* **2019**, *15* (6), 1297–1311. https://doi.org/10.1039/C8SM02045K.
(109) Schnedlitz, M.; Fernandez-Perea, R.; Knez, D.; Lasserus, M.; Schiffmann, A.; Hofer, F.; Hauser, A. W.; de Lara-Castells, M. P.; Ernst, W. E. Effects of the Core Location on the Structural Stability of Ni–Au Core–Shell Nanoparticles. *J Phys Chem C Nanomater Interfaces* **2019**, *123* (32), 20037–20043. https://doi.org/10.1021/acs.jpcc.9b05765.
(110) Sachan, R.; Yadavali, S.; Shirato, N.; Krishna, H.; Ramos, V.; Duscher, G.; Pennycook, S. J.; Gangopadhyay, A. K.; Garcia, H.; R Kalyanaraman. Self-Organized Bimetallic Ag–Co Nanoparticles with Tunable Localized Surface Plasmons Showing High Environmental Stability and Sensitivity. *Nanotechnology* **2012**, *23* (27), 275604. https://doi.org/10.1088/0957-4484/23/27/275604.
(111) Free Energy of a Nonuniform System. I. Interfacial Free Energy: The Journal of Chemical Physics: Vol 28, No 2 https://aip.scitation.org/doi/10.1063/1.1744102 (accessed 2021 -08 -25).
(112) Fischer, H. P.; Maass, P.; Dieterich, W. Novel Surface Modes in Spinodal Decomposition. *Phys. Rev. Lett.* **1997**, *79* (5), 893–896. https://doi.org/10.1103/PhysRevLett.79.893.
(113) Diverging time and length scales of spinodal decomposition modes in thin films | EPL https://epljournal.edpsciences.org/articles/epl/abs/1998/07/42109/42109.html (accessed 2021 -08 -25).
(114) Hohenberg, P. C.; Halperin, B. I. Theory of Dynamic Critical Phenomena. *Rev. Mod. Phys.* **1977**, *49* (3), 435–479. https://doi.org/10.1103/RevModPhys.49.435.
(115) Anderson, D. M.; McFadden, G. B.; Wheeler, A. A. Diffuse-Interface Methods in Fluid Mechanics. *Annual Review of Fluid Mechanics* **1998**, *30* (1), 139–165. https://doi.org/10.1146/annurev.fluid.30.1.139.
(116) Thiele, U.; Madruga, S.; Frastia, L. Decomposition Driven Interface Evolution for Layers of Binary Mixtures. I. Model Derivation and Stratified Base States. *Physics of Fluids* **2007**, *19* (12), 122106. https://doi.org/10.1063/1.2824404.
(117) Madruga, S.; Thiele, U. Decomposition Driven Interface Evolution for Layers of Binary Mixtures. II. Influence of Convective Transport on Linear Stability. *Physics of Fluids* **2009**, *21* (6), 062104. https://doi.org/10.1063/1.3132789.
(118) Bribesh, F. A. M.; Fraštia, Ľ.; Thiele, U. Decomposition Driven Interface Evolution for Layers of Binary Mixtures. III. Two-Dimensional Steady Films with Flat and Modulated Surfaces. *Physics of Fluids* **2012**, *24* (6), 062109. https://doi.org/10.1063/1.4727888.
(119) Naraigh, L. O.; Thiffeault, J.-L. Nonlinear Dynamics of Phase Separation in Thin Films. *Nonlinearity* **2010**, *23* (7), 1559–1583. https://doi.org/10.1088/0951-7715/23/7/003.
(120) Thiele, U.; Todorova, D. V.; Lopez, H. Gradient Dynamics Description for Films of Mixtures and Suspensions: Dewetting Triggered by Coupled Film Height and Concentration Fluctuations. *Phys. Rev. Lett.* **2013**, *111* (11), 117801. https://doi.org/10.1103/PhysRevLett.111.117801.
(121) Wu, Y.; Liu, C.; Moore, T. M.; Magel, G. A.; Garfinkel, D. A.; Camden, J. P.; Stanford, M. G.; Duscher, G.; Rack, P. D. Exploring Photothermal Pathways via in Situ Laser Heating in the Transmission Electron Microscope: Recrystallization, Grain Growth, Phase Separation, and Dewetting in Ag0.5Ni0.5 Thin Films. *Microscopy and Microanalysis* **2018**, *24* (6), 647–656. https://doi.org/10.1017/S1431927618015465.

(122) McKeown, J. T.; Roberts, N. A.; Fowlkes, J. D.; Wu, Y.; LaGrange, T.; Reed, B. W.; Campbell, G. H.; Rack, P. D. Real-Time Observation of Nanosecond Liquid-Phase Assembly of Nickel Nanoparticles via Pulsed-Laser Heating. *Langmuir* **2012**, *28* (49), 17168–17175. https://doi.org/10.1021/la303657e.
(123) McKeown, J. T.; Wu, Y.; Fowlkes, J. D.; Rack, P. D.; Campbell, G. H. Simultaneous In-Situ Synthesis and Characterization of Co@Cu Core-Shell Nanoparticle Arrays. *Advanced Materials 27* (6), 1060–1065. https://doi.org/10.1002/adma.201404374.
(124) Reiter, G. Dewetting of Thin Polymer Films. *Phys. Rev. Lett.* **1992**, *68* (1), 75–78. https://doi.org/10.1103/PhysRevLett.68.75.
(125) Seemann, R.; Herminghaus, S.; Jacobs, K. Dewetting Patterns and Molecular Forces: A Reconciliation. *Phys Rev Lett* **2001**, *86* (24), 5534–5537. https://doi.org/10.1103/PhysRevLett.86.5534.
(126) Seemann, R.; Herminghaus, S.; Neto, C.; Schlagowski, S.; Podzimek, D.; Konrad, R.; Mantz, H.; Jacobs, K. Dynamics and Structure Formation in Thin Polymer Melt Films. *J. Phys.: Condens. Matter* **2005**, *17* (9), S267–S290. https://doi.org/10.1088/0953-8984/17/9/001.
(127) Nguyen, T. T.; Mammeri, F.; Ammar, S. Iron Oxide and Gold Based Magneto-Plasmonic Nanostructures for Medical Applications: A Review. *Nanomaterials* **2018**, *8* (3), 149. https://doi.org/10.3390/nano8030149.
(128) Tomitaka, A.; Arami, H.; Raymond, A.; Yndart, A.; Kaushik, A.; Jayant, R. D.; Takemura, Y.; Cai, Y.; Toborek, M.; Nair, M. Development of Magneto-Plasmonic Nanoparticles for Multimodal Image-Guided Therapy to the Brain. *Nanoscale* **2017**, *9* (2), 764–773. https://doi.org/10.1039/C6NR07520G.
(129) Kretschmer, F.; Mühlig, S.; Hoeppener, S.; Winter, A.; Hager, M. D.; Rockstuhl, C.; Pertsch, T.; Schubert, U. S. Survey of Plasmonic Nanoparticles: From Synthesis to Application. *Particle & Particle Systems Characterization* **2014**, *31* (7), 721–744. https://doi.org/10.1002/ppsc.201300309.
(130) Maksymov, I. S. Magneto-Plasmonic Nanoantennas: Basics and Applications. *Reviews in Physics* **2016**, *1*, 36–51. https://doi.org/10.1016/j.revip.2016.03.002.
(131) Urries, I.; Muñoz, C.; Gomez, L.; Marquina, C.; Sebastian, V.; Arruebo, M.; Santamaria, J. Magneto-Plasmonic Nanoparticles as Theranostic Platforms for Magnetic Resonance Imaging, Drug Delivery and NIR Hyperthermia Applications. *Nanoscale* **2014**, *6* (15), 9230–9240. https://doi.org/10.1039/C4NR01588F.
(132) Ovejero, J. G.; Yoon, S. J.; Li, J.; Mayoral, A.; Gao, X.; O'Donnell, M.; García, M. A.; Herrasti, P.; Hernando, A. Synthesis of Hybrid Magneto-Plasmonic Nanoparticles with Potential Use in Photoacoustic Detection of Circulating Tumor Cells. *Microchim Acta* **2018**, *185* (2), 130. https://doi.org/10.1007/s00604-017-2637-x.
(133) Wu, C.-H.; Cook, J.; Emelianov, S.; Sokolov, K. Multimodal Magneto-Plasmonic Nanoclusters for Biomedical Applications. *Advanced Functional Materials* **2014**, *24* (43), 6862–6871. https://doi.org/10.1002/adfm.201401806.
(134) Chen, M.; Kim, Y. N.; Lee, H. M.; Li, C.; Cho, S. O. Multifunctional Magnetic Silver Nanoshells with Sandwichlike Nanostructures. *The Journal of Physical Chemistry C* **2008**, *112* (24), 8870–8874. https://doi.org/10.1021/jp800649b.
(135) Hamidi, S. M.; Oskuei, M. A. Magneto-Plasmonic Effect in Cobalt Thin Film Incorporating Core–Shell Ag@Au Nanoparticles. *Journal of Superconductivity and Novel Magnetism* **2014**, *27* (6), 1469–1472. https://doi.org/10.1007/s10948-013-2449-0.

(136) Oh, Y.; Lee, J.; Lee, M. Fabrication of Ag-Au Bimetallic Nanoparticles by Laser-Induced Dewetting of Bilayer Films. *Applied Surface Science* **2018**, *434*, 1293–1299. https://doi.org/10.1016/j.apsusc.2017.11.245.
(137) Wu, Y.; Fowlkes, J. D.; Rack, P. D. The Optical Properties of Cu-Ni Nanoparticles Produced via Pulsed Laser Dewetting of Ultrathin Films: The Effect of Nanoparticle Size and Composition on the Plasmon Response. *Journal of Materials Research* **2011**, *26* (2), 277–287. https://doi.org/10.1557/jmr.2010.9.
(138) Allaire, R. H.; Dhakane, A.; Emery, R.; Ganesh, P.; Rack, P. D.; Kondic, L.; Cummings, L.; Fuentes-Cabrera, M. Surface, Interface, and Temperature Effects on the Phase Separation and Nanoparticle Self Assembly of Bi-Metallic Ni0.5Ag0.5: A Molecular Dynamics Study. *Nanomaterials* **2019**, *9* (7), 1040. https://doi.org/10.3390/nano9071040.
(139) Mueller, C. M.; Murthy, R. R.; Bourgeois, M. R.; Schatz, G. C. Thermodynamic Determination of Bimetallic Particle Geometry: Suitability of Poorly Miscible Alloys for Surface-Enhanced Raman. *J. Phys. Chem. C* **2020**, *124* (5), 3287–3296. https://doi.org/10.1021/acs.jpcc.9b10889.
(140) Favazza, C.; Kalyanaraman, R.; Sureshkumar, R. Robust Nanopatterning by Laser-Induced Dewetting of Metal Nanofilms. *Nanotechnology* **2006**, *17* (16), 4229. https://doi.org/10.1088/0957-4484/17/16/038.
(141) Krishna, H.; Sachan, R.; Strader, J.; Favazza, C.; Khenner, M.; Kalyanaraman, R. Thickness-Dependent Spontaneous Dewetting Morphology of Ultrathin Ag Films. *Nanotechnology* **2010**, *21* (15), 155601. https://doi.org/10.1088/0957-4484/21/15/155601.
(142) Jeong, U.; Teng, X.; Wang, Y.; Yang, H.; Xia, Y. Superparamagnetic Colloids: Controlled Synthesis and Niche Applications. *Advanced Materials* **2007**, *19* (1), 33–60. https://doi.org/10.1002/adma.200600674.
(143) Krishnan, K. M. Biomedical Nanomagnetics: A Spin Through Possibilities in Imaging, Diagnostics, and Therapy. *IEEE Transactions on Magnetics* **2010**, *46* (7), 2523–2558. https://doi.org/10.1109/TMAG.2010.2046907.
(144) Correlating the optical property evolution in the Au-Ni binary thin films: From metastable solid solution to phase separated alloy - ScienceDirect https://www.sciencedirect.com/science/article/abs/pii/S0925838819314951 (accessed 2021 -08 -16).
(145) Boldman, W. L.; Garfinkel, D. A.; Collette, R.; Jorgenson, C. S.; Pradhan, D. K.; Gilbert, D. A.; Rack, P. D. Exploring the Composition, Phase Separation and Structure of AgFe Alloys for Magneto-Optical Applications. *Materials Science and Engineering: B* **2021**, *266*, 115044. https://doi.org/10.1016/j.mseb.2021.115044.
(146) Fowlkes, J. D.; Kondic, L.; Diez, J.; Wu, Y.; Rack, P. D. Self-Assembly versus Directed Assembly of Nanoparticles via Pulsed Laser Induced Dewetting of Patterned Metal Films. *Nano Lett.* **2011**, *11* (6), 2478–2485. https://doi.org/10.1021/nl200921c.
(147) Espinosa, A.; Bugnet, M.; Radtke, G.; Neveu, S.; Botton, G. A.; Wilhelm, C.; Abou-Hassan, A. Can Magneto-Plasmonic Nanohybrids Efficiently Combine Photothermia with Magnetic Hyperthermia? *Nanoscale* **2015**, *7* (45), 18872–18877. https://doi.org/10.1039/c5nr06168g.
(148) Tomitaka, A.; Arami, H.; Huang, Z.; Raymond, A.; Rodriguez, E.; Cai, Y.; Febo, M.; Takemura, Y.; Nair, M. Hybrid Magneto-Plasmonic Liposomes for Multimodal Image-

Guided and Brain-Targeted HIV Treatment. *Nanoscale* **2017**, *10* (1), 184–194. https://doi.org/10.1039/c7nr07255d.
(149) Huang, L.; Ao, L.; Hu, D.; Wei, W.; Sheng, Z.; su, wu. Magneto-Plasmonic Nanocapsules for Multimodal-Imaging and Magnetically Guided Combination Cancer Therapy. *Chemistry of Materials* **2016**, *28*. https://doi.org/10.1021/acs.chemmater.6b02413.
(150) Magneto-Plasmonic Au-Fe Alloy Nanoparticles Designed for Multimodal SERS-MRI-CT Imaging - Amendola - 2014 - Small - Wiley Online Library https://onlinelibrary.wiley.com/doi/abs/10.1002/smll.201303372 (accessed 2021 -08 -16).
(151) Magneto-Plasmonic Janus Vesicles for Magnetic Field-Enhanced Photoacoustic and Magnetic Resonance Imaging of Tumors - Liu - 2016 - Angewandte Chemie International Edition - Wiley Online Library https://onlinelibrary.wiley.com/doi/abs/10.1002/anie.201608338 (accessed 2021 -08 -16).
(152) Ogut, E.; Menguc, M. P.; Sendur, K. Integrating Magnetic Heads With Plasmonic Nanostructures in Multilayer Configurations. *IEEE Transactions on Magnetics* **2013**, *49* (7), 3687–3690. https://doi.org/10.1109/TMAG.2013.2247982.
(153) Li, Z.; Jin, J.; Yang, F.; Song, N.; Yin, Y. Coupling Magnetic and Plasmonic Anisotropy in Hybrid Nanorods for Mechanochromic Responses. *Nat Commun* **2020**, *11* (1), 2883. https://doi.org/10.1038/s41467-020-16678-8.
(154) Selective Lactam Formation from Amino Alcohols Using Polymer-Incarcerated Gold and Gold/Cobalt Nanoparticles as Catalysts under Aerobic Oxidative Conditions - Soulé - 2012 - Asian Journal of Organic Chemistry - Wiley Online Library https://onlinelibrary.wiley.com/doi/abs/10.1002/ajoc.201200093 (accessed 2021 -08 -16).
(155) Peiris, E.; Sarina, S.; Waclawik, E. R.; Ayoko, G. A.; Han, P.; Jia, J.; Zhu, H.-Y. Plasmonic Switching of the Reaction Pathway: Visible-Light Irradiation Varies the Reactant Concentration at the Solid–Solution Interface of a Gold–Cobalt Catalyst. *Angewandte Chemie International Edition* **2019**, *58* (35), 12032–12036. https://doi.org/10.1002/anie.201904452.
(156) Marbella, L.; Andolina, C.; Smith, A.; Hartmann, M.; Dewar, A.; Johnston, K.; Daly, O.; Millstone, J. Gold-Cobalt Nanoparticle Alloys Exhibiting Tunable Compositions, Near-Infrared Emission, and High T2 Relaxivity. *Advanced Functional Materials* **2014**, *24*. https://doi.org/10.1002/adfm.201400988.
(157) Bahmanrokh, G.; Hashim, M.; Soltani, N.; Ismail, I.; Vaziri, P.; Navaseri, M.; Erfani, M.; Kanagesan, S. High Coercivity Sized Controlled Cobalt–Gold Core–Shell Nano-Crystals Prepared by Reverse Microemulsion. *Materials Research Bulletin* **2013**, *48* (10). https://doi.org/10.1016/J.MATERRESBULL.2013.06.021.
(158) Cheng, G.; Hight Walker, A. Synthesis and Characterization of Cobalt/Gold Bimetallic Nanoparticles. *Journal of Magnetism and Magnetic Materials* **2007**, *311*, 31–35. https://doi.org/10.1016/j.jmmm.2006.11.164.
(159) Peleg, N.; Shtrikman, S.; Gorodetsky, G.; Felner, I. Magnetic Study of Particle Distribution in Granular AuCo. **1999**. https://doi.org/10.1016/S0304-8853(98)00337-0.
(160) Nabika, H.; Mizuhata, M.; Kajinami, A.; Deki, S.; Akamatsu, K. Preparation and Characterization of Au/Co Nano-Alloys. *Journal of Electroanalytical Chemistry* **2003**, *559*, 99–102. https://doi.org/10.1016/S0022-0728(03)00054-8.

(161) Henger, U.; Korn, D. Electrical Resistivity of Thin Films of AuCo Solid Solutions. **1981**. https://doi.org/10.1088/0305-4608/11/12/010.
(162) Maurizio, C.; Michieli, N.; Kalinic, B.; Mattarello, V.; Bello, V.; Wilhelm, F.; Ollefs, K.; Mattei, G. Local Structure and X-Ray Magnetic Circular Dichroism of Au in Au-Co Nanoalloys. *Applied Surface Science* **2018**, *433*, 596–601. https://doi.org/10.1016/j.apsusc.2017.10.067.
(163) Chinni, F.; Spizzo, F.; Montoncello, F.; Mattarello, V.; Maurizio, C.; Mattei, G.; Del Bianco, L. Magnetic Hysteresis in Nanocomposite Films Consisting of a Ferromagnetic AuCo Alloy and Ultrafine Co Particles. *Materials (Basel)* **2017**, *10* (7), 717. https://doi.org/10.3390/ma10070717.
(164) Optical and Magnetic Properties of Ag–Ni Bimetallic Nanoparticles Assembled via Pulsed Laser-Induced Dewetting | ACS Omega https://pubs.acs.org/doi/10.1021/acsomega.0c02894 (accessed 2021 -08 -16).
(165) Diez, J. A.; González, A. G.; Garfinkel, D. A.; Rack, P. D.; McKeown, J. T.; Kondic, L. Simultaneous Decomposition and Dewetting of Nanoscale Alloys: A Comparison of Experiment and Theory. *Langmuir* **2021**, *37* (8), 2575–2585. https://doi.org/10.1021/acs.langmuir.0c02964.
(166) Johnson, P. B.; Christy, R. W. Optical Constants of the Noble Metals. *Phys. Rev. B* **1972**, *6* (12), 4370–4379. https://doi.org/10.1103/PhysRevB.6.4370.
(167) Johnson, P. B.; Christy, R. W. Optical Constants of Transition Metals: Ti, V, Cr, Mn, Fe, Co, Ni, and Pd. *Phys. Rev. B* **1974**, *9* (12), 5056–5070. https://doi.org/10.1103/PhysRevB.9.5056.
(168) Zhang, C.; Dyck, O.; Garfinkel, D. A.; Stanford, M. G.; Belianinov, A. A.; Fowlkes, J. D.; Jesse, S.; Rack, P. D. Pulsed Laser-Assisted Helium Ion Nanomachining of Monolayer Graphene-Direct-Write Kirigami Patterns. *Nanomaterials (Basel)* **2019**, *9* (10), E1394. https://doi.org/10.3390/nano9101394.
(169) Wu, Y.; Liu, C.; Moore, T. M.; Magel, G. A.; Garfinkel, D. A.; Camden, J. P.; Stanford, M. G.; Duscher, G.; Rack, P. D. Exploring Photothermal Pathways via in Situ Laser Heating in the Transmission Electron Microscope: Recrystallization, Grain Growth, Phase Separation, and Dewetting in Ag0.5Ni0.5 Thin Films. *Microscopy and Microanalysis* **2018**, *24* (6), 647–656. https://doi.org/10.1017/S1431927618015465.
(170) Zhou, J.; Koschny, Th.; Kafesaki, M.; Economou, E. N.; Pendry, J. B.; Soukoulis, C. M. Saturation of the Magnetic Response of Split-Ring Resonators at Optical Frequencies. *Phys. Rev. Lett.* **2005**, *95* (22), 223902. https://doi.org/10.1103/PhysRevLett.95.223902.
(171) Tobing, L. Y. M.; Tjahjana, L.; Zhang, D. H.; Zhang, Q.; Xiong, Q. Sub-100-Nm Sized Silver Split Ring Resonator Metamaterials with Fundamental Magnetic Resonance in the Middle Visible Spectrum. *Advanced Optical Materials* **2014**, *2* (3), 280–285. https://doi.org/10.1002/adom.201300456.
(172) Enkrich, C.; Wegener, M.; Linden, S.; Burger, S.; Zschiedrich, L.; Schmidt, F.; Zhou, J. F.; Koschny, Th.; Soukoulis, C. M. Magnetic Metamaterials at Telecommunication and Visible Frequencies. *Phys. Rev. Lett.* **2005**, *95* (20), 203901. https://doi.org/10.1103/PhysRevLett.95.203901.
(173) Tomioka, T.; Kubo, S.; Nakagawa, M.; Hoga, M.; Tanaka, T. Split-Ring Resonators Interacting with a Magnetic Field at Visible Frequencies. *Appl. Phys. Lett.* **2013**, *103* (7), 071104. https://doi.org/10.1063/1.4818666.

(174) Brandl, D. W.; Mirin, N. A.; Nordlander, P. Plasmon Modes of Nanosphere Trimers and Quadrumers. *J. Phys. Chem. B* **2006**, *110* (25), 12302–12310. https://doi.org/10.1021/jp0613485.
(175) Zohar, N.; Chuntonov, L.; Haran, G. The Simplest Plasmonic Molecules: Metal Nanoparticle Dimers and Trimers. *Journal of Photochemistry and Photobiology C: Photochemistry Reviews* **2014**, *21*, 26–39. https://doi.org/10.1016/j.jphotochemrev.2014.10.002.
(176) Monticone, F.; Al, A. The Quest for Optical Magnetism: From Split-Ring Resonators to Plasmonic Nanoparticles and Nanoclusters. *Journal of Materials Chemistry C* **2014**, *2* (43), 9059–9072. https://doi.org/10.1039/c4tc01406e.
(177) Hentschel, M.; Dorfmüller, J.; Giessen, H.; Jäger, S.; Kern, A. M.; Braun, K.; Zhang, D.; Meixner, A. J. Plasmonic Oligomers in Cylindrical Vector Light Beams. *Beilstein J. Nanotechnol.* **2013**, *4* (1), 57–65. https://doi.org/10.3762/bjnano.4.6.
(178) Selection Rules for Structured Light in Nanooligomers and Other Nanosystems | ACS Photonics https://pubs.acs.org/doi/10.1021/acsphotonics.0c00359 (accessed 2021 -01 -12).
(179) Cherqui, C.; Wu, Y.; Li, G.; Quillin, S. C.; Busche, J. A.; Thakkar, N.; West, C. A.; Montoni, N. P.; Rack, P. D.; Camden, J. P.; Masiello, D. J. STEM/EELS Imaging of Magnetic Hybridization in Symmetric and Symmetry-Broken Plasmon Oligomer Dimers and All-Magnetic Fano Interference. *Nano Lett.* **2016**, *16* (10), 6668–6676. https://doi.org/10.1021/acs.nanolett.6b03504.
(180) Greybush, N. J.; Pacheco-Peña, V.; Engheta, N.; Murray, C. B.; Kagan, C. R. Plasmonic Optical and Chiroptical Response of Self-Assembled Au Nanorod Equilateral Trimers. *ACS nano* **2019**, *13* (2), 1617–1624. https://doi.org/10.1021/acsnano.8b07619.
(181) Li, Z.-J.; Wu, Z.-S.; Li, H.-Y. Analysis of Electromagnetic Scattering by Uniaxial Anisotropic Bispheres. *J. Opt. Soc. Am. A, JOSAA* **2011**, *28* (2), 118–125. https://doi.org/10.1364/JOSAA.28.000118.
(182) Alù, A.; Salandrino, A.; Engheta, N. Negative Effective Permeability and Left-Handed Materials at Optical Frequencies. *Opt. Express, OE* **2006**, *14* (4), 1557–1567. https://doi.org/10.1364/OE.14.001557.
(183) Fan, J. A.; Wu, C.; Bao, K.; Bao, J.; Bardhan, R.; Halas, N. J.; Manoharan, V. N.; Nordlander, P.; Shvets, G.; Capasso, F. Self-Assembled Plasmonic Nanoparticle Clusters. *Science* **2010**, *328* (5982), 1135–1138. https://doi.org/10.1126/science.1187949.
(184) Farbod Shafiei; Francesco Monticone; Khai Q. Le; Xing-Xiang Liu; Thomas Hartsfield; Andrea Alù; Xiaoqin Li. A Subwavelength Plasmonic Metamolecule Exhibiting Magnetic-Based Optical Fano Resonance. *Nature Nanotechnology* **2013**, *8* (2), 95–99. https://doi.org/10.1038/nnano.2012.249.
(185) Morits, D. K.; Simovski, C. R. Negative Effective Permeability at Optical Frequencies Produced by Rings of Plasmonic Dimers. *Phys. Rev. B* **2010**, *81* (20), 205112. https://doi.org/10.1103/PhysRevB.81.205112.
(186) Probing Nanoparticle Plasmons with Electron Energy Loss Spectroscopy | Chemical Reviews https://pubs.acs.org/doi/abs/10.1021/acs.chemrev.7b00354 (accessed 2021 -02 -03).
(187) Coenen, T.; Haegel, N. M. Cathodoluminescence for the 21st Century: Learning More from Light. *Applied Physics Reviews* **2017**, *4* (3), 031103. https://doi.org/10.1063/1.4985767.

(188) Boudarham, G.; Feth, N.; Myroshnychenko, V.; Linden, S.; De Abajo, J. G.; Wegener, M.; Kociak, M. Spectral Imaging of Individual Split-Ring Resonators. *Physical review letters* **2010**, *105* (25), 255501. https://doi.org/10.1103/PhysRevLett.105.255501.
(189) Liang, Q.; Wen, Y.; Mu, X.; Reindl, T.; Yu, W.; Talebi, N.; Van Aken, P. A. Investigating Hybridization Schemes of Coupled Split-Ring Resonators by Electron Impacts. *Optics express* **2015**, *23* (16), 20721–20731. https://doi.org/10.1364/OE.23.020721.
(190) Liu, C.; Wu, Y.; Hu, Z.; Busche, J. A.; Beutler, E. K.; Montoni, N. P.; Moore, T. M.; Magel, G. A.; Camden, J. P.; Masiello, D. J.; Duscher, G.; Rack, P. D. Continuous Wave Resonant Photon Stimulated Electron Energy-Gain and Electron Energy-Loss Spectroscopy of Individual Plasmonic Nanoparticles. *ACS Photonics* **2019**, *6* (10), 2499–2508. https://doi.org/10.1021/acsphotonics.9b00830.
(191) Zewail, A. H. Four-Dimensional Electron Microscopy. *Science* **2010**, *328* (5975), 187–193. https://doi.org/10.1126/science.1166135.
(192) Howie, A. New Instrumentation and Cutting Edge Research. *Ultramicroscopy* **2017**, *180*, 52–58. https://doi.org/10.1016/j.ultramic.2016.11.006.
(193) Shorokhov, D.; Zewail, A. H. Perspective: 4D Ultrafast Electron Microscopy—Evolutions and Revolutions. *J. Chem. Phys.* **2016**, *144* (8), 080901. https://doi.org/10.1063/1.4941375.
(194) Barwick, B.; Zewail, A. H. Photonics and Plasmonics in 4D Ultrafast Electron Microscopy. *ACS Photonics* **2015**, *2* (10), 1391–1402. https://doi.org/10.1021/acsphotonics.5b00427.
(195) Yurtsever, A.; Baskin, J. S.; Zewail, A. H. Entangled Nanoparticles: Discovery by Visualization in 4D Electron Microscopy. *Nano Lett.* **2012**, *12* (9), 5027–5032. https://doi.org/10.1021/nl302824f.
(196) Barwick, B.; Flannigan, D. J.; Zewail, A. H. Photon-Induced near-Field Electron Microscopy. *NATURE, Nature,, Nature.* **2009**, *462* (7275), 902–906. https://doi.org/10.1038/nature08662.
(197) Lu, Y.; Yoo, B.-K.; Ng, A. H. C.; Kim, J.; Yeom, S.; Tang, J.; Lin, M. M.; Zewail, A. H.; Heath, J. R. 4D Electron Microscopy of T Cell Activation. *PNAS* **2019**, *116* (44), 22014–22019. https://doi.org/10.1073/pnas.1914078116.

VITA

David Garfinkel was born in Visalia, California to parents Michael Garfinkel and Elizabeth Garfinkel. David was raised in Eugene, OR, and went to Oregon State University for his undergraduate degree. He was awarded a B.S. in mechanical engineering in 2014, and a M.S. in materials science and engineering in 2016, also from Oregon State University. He was advised by Dr. Julie Tucker, and his thesis is titled "Role of Alloying on Thermal Stability of Duplex Stainless Steels". At the University of Tennessee, David was advised by Dr. Philip Rack. His research was focused on pulsed laser induced dewetting of multi-component metal systems, and their optical and magnetic properties, as well as nanofabrication and characterization of plasmonic structures.